



School of Architecture, Civil and Environmental Engineering ENAC

Resilient Steel Structures Laboratory RESSLab

Finite element investigation of the Slotted-Hidden-Gap (SHG) connection for square HSS bracing members under cyclic loading

Master's thesis

Author :

Joëlle LUU

Supervisors :

Prof. Dimitrios LIGNOS, EPFL
Prof. Colin ROGERS, McGill University

July 8, 2023

Acknowledgments

I would like to express my appreciation to Professor Dimitrios Lignos from the Ecole Polytechnique Fédérale de Lausanne for supervising this thesis. His guidance and expertise in the field of steel structures have been greatly valued. I also thank him for his enthusiasm in pursuing the master's project abroad and for providing me with the opportunity to pursue it in Montreal.

I would also like to thank Professor Colin Rogers for suggesting this fascinating topic and for his warm welcome at McGill University. His dedication, availability, and valuable pieces of advice have been more than appreciated. I am truly grateful for his kindness and wisdom.

My thanks also go to Mohamed Afifi for sharing his work with me, and to Diego Heredia Rosa for assisting me during challenging times with Abaqus.

To my friends, Ghita, who always believed in me more than I did and who has always been an incredible support. Last but certainly not least, I would like to express my profound gratitude to Gwen, who has been the sunshine of my adventure in Montreal, making me feel at home. Thank you for the wonderful memories we created together, which will forever hold a special place in my heart.

Abstract

The Slotted-Hidden-Gap (SHG) connection is an improved version of the conventional welded tube-to-gusset connection between hollow braces and framing elements used in Concentrically Braced Frames (CBFs), offering an enhanced performance without the need for additional reinforcement. Previous studies have demonstrated the efficiency of this feature in circular and square Hollow Structural Section (HSS) braces under monotonic tensile loading conditions, leading to the development of a design methodology based on the CSA S16-19 to construct the connection. However, limited research has been dedicated to investigating the compressive behavior of the brace and its connections. In order to obtain a more comprehensive understanding of the seismic behavior of the SHG connection, a numerical parametric study is conducted to examine the inelastic response of the connection under reversed cyclic loading conditions. Various parameters are considered, including the square HSS tube's size, the weld's length and size, the brace's slenderness, and the degree of confinement of the gusset plate that plays a crucial role in the development of a plastic hinge. Designed based on the previously developed methodology, the simulated braces demonstrated their ability to withstand compression cycles without fracturing at the connection, making it capacity design protected. The findings indicate that all confinement degrees of the gusset plate in the numerically tested models, from a constrained gusset plate to a linear clearance, led to a fracture away from the connection at mid-length of the brace. Notably, the use of a constrained gusset plate that redirected the moment towards the HSS tube's end resulted in an average additional 2.85% of plastic strains at the brace's slots compared to an elliptical or linear offset in the gusset plate. This effect was observed in stockier braces, yet no fracturing occurred.

Keywords : Concentrically Braced Frames (CBFs), Hollow Structural Sections (HSS), steel braces, welded connections, numerical simulations, FE models, constructability, seismic design

Contents

1	Introduction	11
1.1	Objectives and methodology	12
2	Literature review	13
2.1	Concentrically Braced Frames (CBFs)	13
2.1.1	Inelastic response of the brace subjected to seismic action	15
2.1.2	Effect of global and local slenderness	17
2.2	Hollow Structural Sections (HSS)	17
2.2.1	Material properties	18
2.3	Slotted-Hidden-Gap (SHG) connection	19
2.3.1	Background	20
2.3.2	Design and detailing methodology	22
2.4	Compressive behaviour of gusset plates	23
3	Calibration of FE model against test result	26
3.1	Laboratory-tested full-brace	26
3.2	Finite Element Model (FEM)	30
3.2.1	Detailed description of the FE model	30
3.3	SHG connection subjected to cyclic loading	35
4	Study of the hinge zone of the gusset plate	37
4.1	Brace and connection configurations	37
4.2	Assumptions	39
4.3	Results and discussion	42
4.4	Summary	55
5	Feasibility study of the SHG connection construction	56
5.1	Constructability of the SHG connection on-site	57
5.2	Conceptual solution ideas	58
5.2.1	Solution 1 - Reduction of the overlap length ratio	58
5.2.2	Solution 2 - Modification of the gusset plate's notch geometry	59
5.2.3	Solution 3 - Increase of the hidden gap's length	60
5.3	Alternative connections to build on-site	64

5.4	Summary	66
6	Conclusion and recommendations	67
7	Appendix	72
7.1	Design sheets for the parametric study	72
7.2	Chemical composition of the steel grades	76
7.3	Hysteretic curves with a constrained and elliptical hinge zone	77
7.4	Von Mises stress distributions	78

List of Figures

1	Conventional connection (Figure courtesy of Afifi (2021))	11
2	SHG connection (Figure courtesy of Afifi (2021))	12
3	CBFs configurations - a) single diagonal bracing, b) V-bracing, c) inverted V-bracing, d) X-diagonal bracing, e) split X-bracing	13
4	Braces cross-sections - a) L-shape angle, b) U-shape angle, c) RHS d) CHS, e) I-shape cross-section	14
5	Schematic P-u hysteretic relationship of a brace subjected to cyclic axial loading . . .	15
6	a) b) conventional connection (CC), c) CC with reinforcing plates, d) CC with return welds, e) f) SHG connection (Figure courtesy of Afifi (2021))	19
7	Dimensions of the SHG connection	21
8	Clearance rules	24
9	Whitmore's section	25
10	Full scale brace Specimen 12 tested by Moreau (2014) (Figures courtesy of Moreau (2014))	26
11	True stress-strain relationships for gusset plates, HSS tube and welds	28
12	Schematic drawing of the inverted V-bracing frame with SHG connections	28
13	Tensile-dominated loading protocol	29
14	Visual representation of the FE model	30
15	Longitudinal and transverse residual stress distributions of the HSS	31
16	Results from the buckling analysis (first eigenmode)	32
17	Photograph of the bottom grip of Specimen 12 by Moreau (2014)	32
18	Boundary conditions of the FE model	33
19	Global and local mesh of the HSS brace and its SHG connections	34
20	Force-displacement calibration of the FEM against the Specimen 12 with $\frac{KL}{r} = 57$ and $\frac{B}{t} = 15.6$	35
21	Comparison of the time histories of Specimen 12 and FEM	36
22	Degrees of confinement of the gusset plate for HSS 254 254 13	39
23	Loading protocol (IDR vs. cycles)	40
24	Loading protocol (IDR vs. time)	40
25	Force-displacement hysteretic response of the braces with a linear clearance zone in the gusset plate	42
26	Force-displacement hysteretic curves for HSS 127 127 6.4 with a constrained, elliptical and linear hinge zone	43

27	Lateral displacement distribution U_x for HSS 127 127 6.4 with different gusset plate configurations	44
28	Moment Vs. Rotation at the SHG connection near the HSS brace's slot	46
29	Critical location on the HSS at the connection	47
30	PEEQ distributions of 1AC, 2AC and 3AC models (constrained hinge zone with weld configuration A, respectively for HSS 127 127 6.4, HSS 254 254 13 and HSS 305 305 16) at the buckling resistance and T_{max}	48
31	PEEQ vs. Drift measured on the HSS at the end of the welds with a linear clearance in the gusset plate	49
32	PEEQ vs. Drift measured on the HSS at the end of the welds with a constrained and elliptical offset in the gusset plate	50
33	PEEQ vs. Drift measured on the HSS corner at the end of the welds for 1AC model (constrained hinge zone)	51
34	Von Mises stress distributions for 1AL1, 1BE, 1AC models at their respective buckling resistance	52
35	Von Mises stress distributions for 2AL1, 2BE, 2AC models at their respective buckling resistance	53
36	Von Mises stress distributions for 3AL1, 3BE, 3AC models at their respective buckling resistance	53
37	Von Mises stress distributions of the 1AL1 model (constrained hinge zone) at the buckling resistance and T_{max}	54
38	Von Mises stress distribution for constrained and elliptical configuration for HSS 305 305 16 at the buckling load	54
39	Paddle-to-gusset plates connections : a) 2-plates b) 4-angles c) Splice plate d) T-stub (Figure courtesy of Afifi (2021))	56
40	Implementation of the 3BL1 model ($L_{wg}/L_w = 15\%$)	57
41	Implementation of the 3AL1 model ($L_{wg}/L_w = 5\%$)	58
42	Solution 2 - Modification of the geometry of the gusset plate's notch geometry (3AL1 model with $L_{wg}/L_w = 5\%$)	59
43	Solution 3 - Increase of the hidden gap's length (3AL1 model with $L_{wg}/L_w = 5\%$)	61
44	Solution 3 - Increase of the hidden gap's length (3BL1 model with $L_{wg}/L_w = 5\%$)	62
45	Alternatives for the geometry of the gusset plate's notch	63
46	Bolted/welded gusset plate associated to the SHG connection	65
47	Bolted/welded rib-plate associated to the SHG connection	65
48	Bolted splice gusset plate associated to the SHG connection	66

49	Hysteretic response of the braces with a constraint and elliptical clearance zone in the gusset plate	77
50	Von Mises stress distributions for 1AL1, 1BE, 1AC models at their respective T_{max} . .	78
51	Von Mises stress distributions of the 1AC model (elliptical hinge zone) at the buckling resistance and T_{max}	78
52	Von Mises stress distributions of the 1BE model (linear hinge zone) at the buckling resistance and T_{max}	79

List of Tables

1	Types of CBFs and their corresponding ductility/overstrength-related factors	14
2	Behaviour factors for CBFs according to the EN 8	14
3	Behaviour factors according to SIA 263:2013	15
4	Material properties of most used specifications in Canada	18
5	Material properties of Specimen 12's HSS tube	27
6	Grades of each element of Specimen 12	27
7	Measured geometric properties of the Specimen 12	27
8	Mesh size of the elements	34
9	Response parameters of Specimen 12	36
10	Numerical models matrix	37
11	Grades of each element of the parametric study's models	41
12	Geometrical properties of the different solutions	62
13	Chemical composition of several specifications based on the heat analysis	76
14	Loads, Drifts and Cycles at buckling load and T_{max} for xAC, xBE and xAL1 type . .	79

List of symbols

A_g	Brace's gross area
A_{gv}	Shear area
A_{ne}	Net area
B	Width of the HSS member
b	Evolution rate of the yield surface
C_u	Probable buckling compressive resistance
C'_u	Probable post-buckling compressive resistance
D_w	Weld's size
E	Steel elastic modulus
F_e	Euler buckling stress
F_u	Specified minimum ultimate tensile stress
F_y	Specified minimum yield tensile stress
K	Effective length factor
h_s	Height of the frame (centerline-to-centerline)
LB	Local buckling
L_H	Brace's length including half of the clearance on each side
L_{CC}	Centerline-to-centerline distance between beam-to-column joints
L_b	Brace's length
L_w	Weld's length
L_{wg}	Weld's overlap length
N_{cr}	Critical elastic buckling load
$N_{b,Rd}$	Design buckling resistance of a compression member
n	Parameter that considers the manufacturing process
OB	Overall buckling
R_y	Factor applied to F_y to estimate the probable yield strength
R_o	Overstrength-related force modification factor
R_d	Ductility-related force modification factor
r	Radius of gyration of the HSS cross-section
Q_∞	Maximum change in the yield surface size
q	Behaviour factor
T_u	Probable tensile resistance
t_{HSS}	Thickness of the HSS member
t_g	Gusset plate's thickness
t_{slot}	Slot's width in the HSS tube
W_g	Gusset plate's width
α	Imperfection factor
γ_{M1}	Resistance factor
θ	Angle of inclination of the brace
δ	Axial displacement of the brace
λ	Non-dimensional slenderness
$\bar{\lambda}$	Normalized member slenderness
χ	Reduction factor for the relevant buckling mode

Units

Dimensions	mm
Loads	N or kN
Stresses	N/mm ² (= MPa)

1 Introduction

Concentrically Braced Frames (CBFs) are a popular structural system used in seismic areas due to their inherent high stiffness compared to other Seismic Force Resisting Systems (SFRSs). They are comprised of framing and dissipative elements arranged in a large vertical planar truss. Hollow Structural Sections (HSS) are typically chosen as fuse bracing elements to dissipate energy through inelastic cycles comprising yielding in tension and buckling in compression to avoid premature fracture of the structural members. In accordance with capacity design principles, framing elements such as beams, columns, foundations, and brace connections are designed to ensure that they possess sufficient capacity to withstand the expected forces and resistances exerted by the brace.

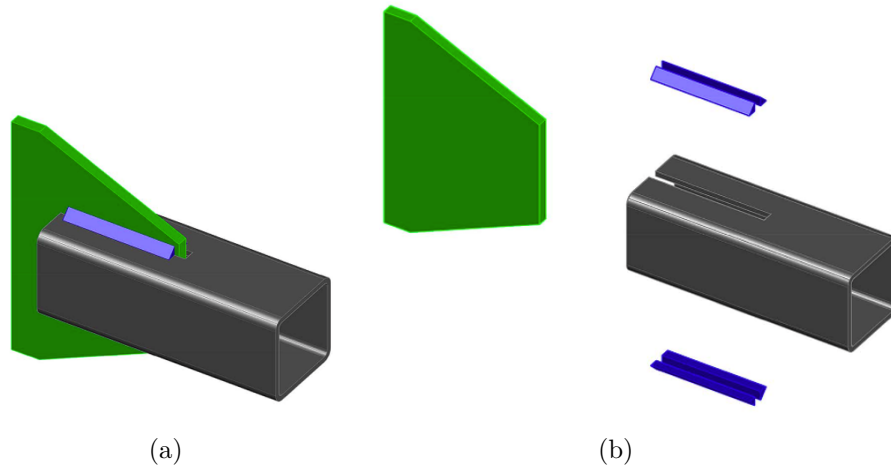


Figure 1: Conventional connection (Figure courtesy of Afifi (2021))

A gusset plate inserted in HSS slots and welded using two fillet weld lines on each side of the slot is often chosen as a connection between braces and beam-to-column joints. Although, the so-called *conventional connection* shown in Figure 1 is widely used, it has several serious drawbacks including a reduced section area due to the HSS slots and unevenly distributed stresses due to shear lag around the connection when subjected to tensile loading conditions. The latter disadvantage often leads engineers and fabricators to either add reinforcing plates on both sides of the HSS member or to practice a return weld around the gusset plate. Return welds are proven to be unsuitable for seismic design due to potential residual stresses caused by a change in temperature while additional welded plates are uneconomic as the reinforcement scheme requires additional design and material. Therefore, the Slotted-Hidden-Gap (SHG) connection as depicted in Figure 2 has been developed to prevent the connection to be reinforced. It consists of a notched gusset plate inserted in the slotted HSS brace members where the welds can start on the gross section of the tube. Once the connection has been entirely manufactured, the space between the end of the notch in the gusset plate and the HSS tube's slot end becomes invisible. The great advantage of the SHG connection detail is to move stress concentrations away from the HSS net area as the weld lines start in the gross section of the brace thereby reducing the risk of fracture at that specific location.

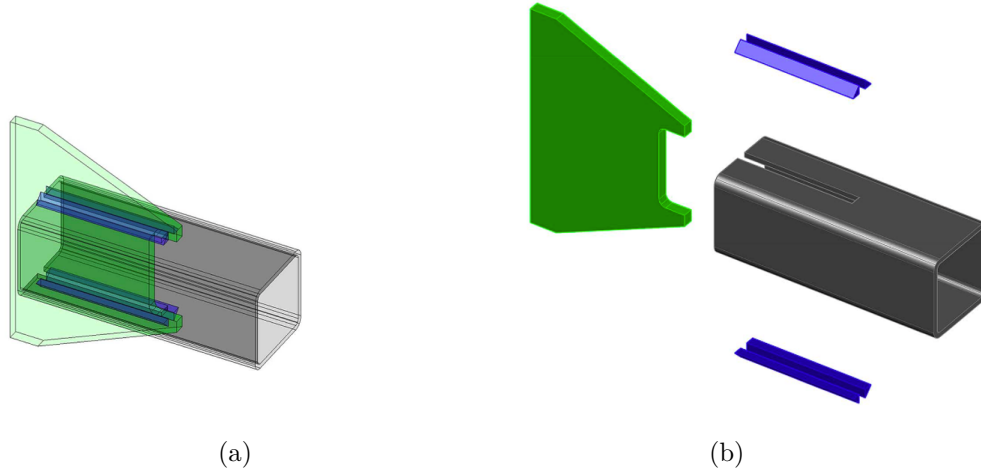


Figure 2: SHG connection (Figure courtesy of Afifi (2021))

Extensive research programs have been conducted on the SHG connection by Martinez-Saucedo (2007), Moreau (2014) and Afifi (2021) using circular and square HSS bracing members to identify the key parameters influencing its behaviour when subjected to a tensile loading. As a result, a design methodology (Afifi et al., 2023) was developed to address the design of this connection due to the absence of specific recommendations in Canadian Steel Design Standard CSA S16-19(CSA, 2019). Despite conducting a reversed cyclic full-scale brace test as a proof of concept in one of these programs (Moreau, 2014), prior research has focused on the SHG connection subjected to a tensile loading since it is often anticipated that the tensile resistance within the brace will be greater than the expected compressive strength. Furthermore, the connection's main challenge stems from the decreased tension resistance, which arises due to factors like the net section of the HSS tube and shear lag problems. Therefore, the response of this connection under cyclic loading, with an emphasis on compression loading cycles, has not been specifically studied, making it the central focus of this thesis.

1.1 Objectives and methodology

The objective of this research project is to assess the SHG connection when subjected to a cyclic loading protocol to study its compressive behaviour. Finite Element Analysis (FEA) is used for this purpose. The second part of the study's objective is to carry out a qualitative examination of the implementation of the SHG HSS brace connection on construction sites. To achieve these objectives, the thesis proceeds through the following steps:

- Calibration study of a Finite Element Model (FEM) under reversed cyclic loading against the results of a full SHG HSS brace tested in the laboratory by Moreau (2014) ;
- Parametric study of the SHG connection elaborated from the design methodology developed by Afifi et al. (2023) through FE analysis ;
- Study of the geometric feasibility of the implementation of the SHG HSS brace connection on construction sites.

2 Literature review

2.1 Concentrically Braced Frames (CBFs)

Concentrically Braced Frames (CBFs) are recognized to be stiffer, more economical and very suitable when Serviceability Design Limit State (SLS) governs the design than Moment Resisting Frames (MRFs) or other Seismic Force Resisting Systems (SFRSs). They are comprised of framing and dissipative elements arranged in a large vertical planar truss. Although CBFs are typically simplified as trusses in design, their actual behavior is more intricate. This complexity arises from the significant resistance and stiffness provided by the connections within the frames (Sen et al., 2016).

Designed for smaller and more frequent earthquakes, the framing elements such as beams, columns, diaphragms, connections must remain elastic while fuse elements, i.e. braces respond inelastically and successively through yielding in tension and buckling in compression when capacity design principles are adopted in order to prevent premature fracture of structural members. By withstanding considerable deformation, this form of energy dissipation of the braces allow the building to resist an earthquake if properly designed without loss of stiffness or strength. After a significant amount of cycles, the favoured failure mode is the brace fracture. CBFs have certain drawbacks, including low redundancy, reduced compressive capacity of the braces, and the potential for low-cycle fatigue failure (B. Shaback & Brown, 2003).

Commonly used in industrial and multi-storey buildings, this system presents a wide range of configurations including single diagonal bracing, V-bracing, inverted V-bracing, X-bracing and split X-bracing as presented in Figure 3. The choice of the configuration relies on structural, architectural and economical considerations. All types of sections can be used for the braces : angles (L- or U-shape), Hollow Structural Sections (HSS) such as Square, Rectangular and Circular Hollow Sections, respectively SHS, RHS, CHS and I-shape cross-sections shown in Figure 4. Rods and pipes could also act as bracing members.

While the elastic response spectra in the Swiss Standard SIA 261 (SIA, 2020) are designed for a return period of 475 years (seismic event with a 10% probability of exceedence over 50 years), earthquakes in Canada are defined as rarer event with a return period of 2475 years (2% probability of exceedence over 50 years) (Adams & Atkinson, 2003).

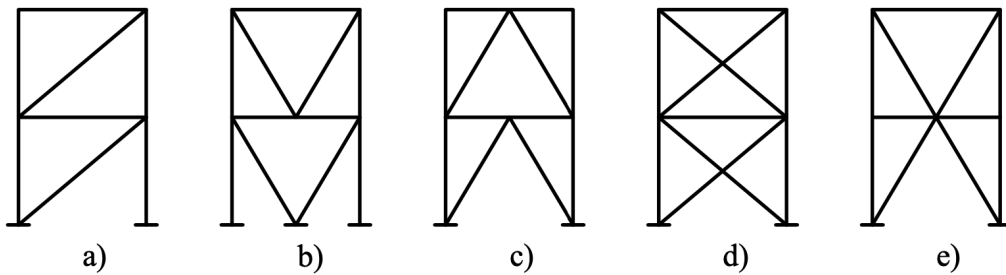


Figure 3: CBFs configurations - a) single diagonal bracing, b) V-bracing, c) inverted V-bracing, d) X-diagonal bracing, e) split X-bracing

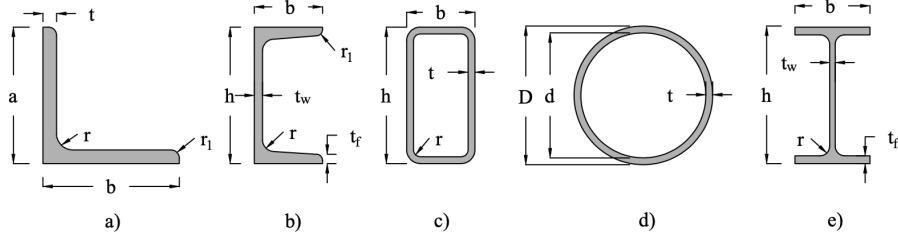


Figure 4: Braces cross-sections - a) L-shape angle, b) U-shape angle, c) RHS d) CHS, e) I-shape cross-section

The Canadian Steel Design Standard CSA S16-19 (CSA, 2019) provide the seismic design requirements for various types of CBFs defined in the National Research Council of Canada (NRCC, 2022). These types include Moderately Ductile (MD), Limited-Ductility (LD) and Conventional Construction (CC), where MD and LD types are only considered when capacity design is adopted. The ability of a structure to dissipate energy can be taken into consideration by the behaviour factor. It is a rough estimate of the seismic forces that the structure could encounter if it responded totally elastically to the seismic forces used in the design. The more dissipative the building is expected to be, the larger is the behaviour factor. In the case of the CSA S16-19 (CSA, 2019), that number is provided by the product of the ductility-related force modification factor that reflects the capacity of a system to dissipate energy through an inelastic behaviour R_d and the overstrength-related force modification factor that accounts for the dependable portion of reserve strength in a structure R_o . Those factors are listed for each CBFs type in Table 1. Achieving suitable strength, stiffness, energy dissipation or ductility, and inelastic deformation capacity must be the aim of earthquake design. Principles of capacity design are applied to prevent early failure and to produce a succession of inelastic behaviours aimed at a particular yield sequence and chosen failure mechanism.

Table 1: Types of CBFs and their corresponding ductility/overstrength-related factors

Type	R_d	R_o	$R_d \cdot R_o$
MD	3.0	1.3	3.9
LD	2.0	1.3	2.6
CC	1.5	1.3	1.95

In Europe, the seismic design provisions Eurocode 8 (CEN, 2004) classify structural systems into three ductility classes : DCL (low), DCM (medium), and DCH (high). The DCL class corresponds to a design concept with low dissipative structural behavior, where the behavior factor, denoted q is below 1.5 or 2. In contrast, the behavior factors for the more ductile classes, i.e. for DCM and DCH are higher. The upper limits of these factors are determined based on the frame type and configuration. Table 2 below presents the values for diagonal and V-bracings in CBFs.

Table 2: Behaviour factors for CBFs according to the EN 8

Structural type	Diagonal bracing	V-bracings	Required cross-sectional class
DCM	4	2	1 or 2
DCH	4	2.5	1 or 2

The SIA 261 (SIA, 2020) also provides the behavior factors based on the structural system and cross-sectional class. It is worth noting that the seismic regulations in the Swiss codes generally align with the Eurocode 8 (CEN, 2004).

Table 3: Behaviour factors according to SIA 263:2013

Structural type	Cross-section classification		
	Class 1	Class 2	Class 3
MRFs	5	4	2
CBFs with X-bracings	4	4	2
CBFs with V-bracings	2.5	2.5	2

2.1.1 Inelastic response of the brace subjected to seismic action

In order to understand how energy dissipation occurs in CBFs, the seismic response of the brace is described. The behaviour of the brace is typically described for a simply supported member axially loaded subjected to one or multiple successive cycles in tension and compression, and is represented in a graph with the axial displacement u in the horizontal axis and the axial load P in the vertical axis. A schematic plot is presented in Figure 5.

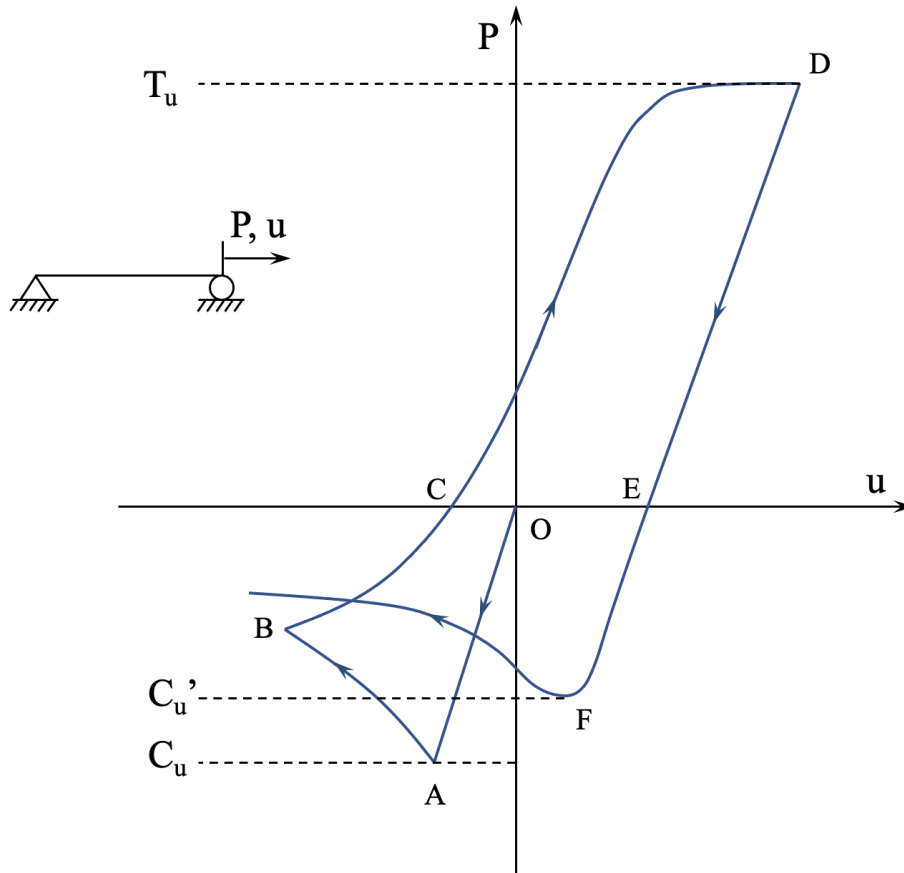


Figure 5: Schematic P-u hysteretic relationship of a brace subjected to cyclic axial loading

Initially, the brace is axially loaded in compression to reach the initial compressive resistance denoted C_u with a linear behaviour where it starts to buckle (O-A). Global buckling results in a formation of a plastic hinge at mid-length and potentially others at the connections depending on the boundary conditions. As a consequence, the axial compressive resistance is reduced to point B. Then, the brace is unloaded to point C where a residual displacement is left due to an out-of-plane deformation. A nonlinear path between B and C is explained by the interaction between compressive and flexure components that contribute to the behaviour. Subsequently, it is loaded in the opposite direction, i.e. in tension, until it reaches its tensile resistance T_u and yields at point D. When the load is reversed to reach point E, a residual deformation due straightening of the brace cannot be recovered. In the following cycle, the compressive resistance C'_u deteriorates after brace buckling and can be explained by the Bauschinger effect, where the lateral deformation increases owing the second order effects (Tremblay, 2002).

According to CSA S16-19 (CSA, 2019) § 27.5.4.2, the probable tensile T_u and compressive resistance C_u and post-buckling resistance C'_u are respectively given by Equations 1, 2 and 5 where components are defined in the Notation Section.

$$T_u = A_g \cdot R_y \cdot F_y \quad (1)$$

$$C_u = \min[A_g \cdot R_y \cdot F_y; 1.2 \cdot A_g \cdot R_y \cdot F_y \cdot (1 + \lambda^{2n})^{-1/n}] \quad (2)$$

$$\lambda = \sqrt{\frac{R_y \cdot F_y}{F_e}} \quad (3)$$

$$F_e = \frac{\pi^2 \cdot E}{(\frac{KL}{r})^2} \quad (4)$$

$$C'_u = \min[0.2 \cdot A_g \cdot R_y \cdot F_y; A_g \cdot R_y \cdot F_y \cdot (1 + \lambda^{2n})^{-1/n}] \quad (5)$$

Equations 6 and 11 are derived from Eurocode 8 (CEN, 2004) on the Design of structures for earthquake resistance and are equivalent to the ones in CSA S16-19 (CSA, 2019).

$$N_{b,Rd} = \frac{\chi \cdot N_{pl,Rd}}{\gamma_{M1}} \quad (6)$$

$$\bar{\lambda} = \sqrt{\frac{A_g \cdot F_y}{N_{cr}}} \quad (7)$$

$$N_{cr} = \frac{\pi^2 \cdot E \cdot I}{(k \cdot L)^2} \quad (8)$$

$$\chi = \frac{1}{\phi + \sqrt{\phi^2 - \bar{\lambda}^2}} \leq 1.0 \quad (9)$$

$$\phi = 0.5 \cdot (1 + \alpha \cdot (\bar{\lambda} - 0.2) + \bar{\lambda}^2) \quad (10)$$

$$N_{b,residual,Rd} = \gamma_{pb} \cdot N_{pl,Rd} \quad (11)$$

$$N_{pl,Rd} = A_g \cdot F_y \quad (12)$$

The parameter α is an imperfection factor that depends on the buckling curves. The latter are established according to the geometry of the cross-sections, the manufacturing process that induces residual stresses (cold-formed or hot-finished) for hollow sections, the thickness of the profile and the steel grade of the member. The γ factor depends on the standards of the specific country, however the Eurocode 8 suggests a value of 0.3.

2.1.2 Effect of global and local slenderness

The global slenderness of a member is determined by a dimensionless ratio KL/r , where K represents the effective length factor, L is the brace's length, and r is the radius of gyration of the section about the relevant axis. On the other hand, the element slenderness of a cross-section is characterized by the dimensionless ratio of the width-to-thickness B/t of the profile.

The seismic performance of steel bracing members is influenced by both global and element slenderness, making it challenging to analyze their effects independently. However, general trends regarding the energy dissipation capacity and the fracture life of braces have been observed in prior laboratory studies (Lee & Bruneau, 2005; B. Shaback & Brown, 2003; Tremblay et al., 2003; Tremblay et al., 2008; Wakabayashi et al., 1977). Those programs have shown that both parameters influence greatly the seismic performance of the steel bracing members. More specifically, the energy dissipation and fracture life increase respectively with a decreasing global and local slenderness. As a result, it was first assumed that braces with low slendernesses and width-to-thickness ratios performed better under seismic action (Lee & Bruneau, 2005). During inelastic hinge rotation, however, stocky bracing, i.e. tubes with low overall slenderness can impose large compressive strains at the plastic hinge. Therefore, local buckling may be initiated early, resulting in fracture due to low-cycle fatigue, especially for RHS bracing members (Fell et al., 2006; Tremblay, 2002).

2.2 Hollow Structural Sections (HSS)

Findings from Popov and Black (1981) showed that square HSS performed better than other rolled shapes thanks to higher radii of gyrations and greater resistances to local buckling. HSS are widely used as structural members for columns, truss elements and bracing members due to their inherent strength, tensile, compressive bending and torsional properties (Fadden & McCormick, 2014). In

addition to their aesthetic appearance, their geometry facilitates the storage in trucks and transport to construction sites and their low strength-to-weight ratio makes them economically attractive (Yaghoubshahi & Imanpour, 2021).

The manufacturing of HSS members start from uncoiling and flattened steel strips that are joined one after another using an end weld. The latter is scrapped off to obtain a flat surface after which the strip heads in the accumulator for forming by passing underneath convex rolls. Each roll has different depths to curve the strips until they form a U-shape. The next step consists of passing the bent strip under concave rolls to push the edges and close the member. The edges are sealed using Electric Resistance Welding (ERW) where the heat zone can rise up to 1500 °C. The excess weld is carved off to obtain an invisible seal. A cold-formed steel member will be cooled using a stream of water to prevent cracking and splitting of the material, whereas the latter step is skipped for hot-rolled HSS tubes (“Atlas Tube”, 2023). Cold-forming allows the steel to recrystallize and leads to grains refining of the material. Although the yield limit is increased thanks to strain hardening, the latter process can imply a shorter ductility range. It can also lead to a higher yield strength in the corners of the tube which can greatly influence the fracture life of the member as shown in past stub-columns tests (Sun & Packer, 2014). Moreover, that manufacturing process leads to the creation of residual stresses in the longitudinal and transverse directions of the members (Koval, 2018), and as expressed in Equations 1 and 2, the change of the yield limit is not taken into account in the CSA S16-19 (CSA, 2019).

2.2.1 Material properties

Typical specifications used for HSS members in Canada are CSA G40.20/G40.21 (CSA, 2009) class C (cold-formed) or class H (either hot-rolled or cold-formed and stress relieved) , ASTM A500 (ASTM, 2003) grade B or C for HSS members and ASTM A1085 (ASTM, 2022) (J.A Packer, 1997; Packer et al., 2010). The material properties of each specification are summarized in Table 4.

Table 4: Material properties of most used specifications in Canada

Specification	Manufacturing process	Grade	F_y [MPa]	F_u [MPa]	Wall thickness reduction
ASTM A500	Cold-formed	B	315	400	-10 %
		C	345	425	
ASTM A1085	Cold-formed	-	min. 345 (= 50 ksi) max. 483 (= 70 ksi)	450	-5 %
CSA G40.20/ G40.21	Cold-formed or stress-relieved	350W	350	450	-5%

Unlike other specifications, ASTM A500 grade B and C exhibit different yield strengths for circular and rectangular HSS, creating potential confusion. The values given in the Table 4 for ASTM A500 are for RHS. Furthermore, grade C of ASTM A500 offers higher yield strengths compared to grade B, making it suitable for a wide range of applications. Hence, the latter specification is less suitable for seismic applications due to very permissive geometric manufacturing tolerances and a lack of requirement regarding the Charpy V-Notch (CVN) toughness specification (J.A Packer, 1997). The AISC 360-10 (AISC, 2010) suggests a reduction of $0.93 \cdot t_{nom,wall}$ whereas the Canadian Institute of

Steel Construction CISC (2010) specifies a design wall thickness equal to $0.90 \cdot t_{nom,wall}$ (“Atlas Tube”, 2023; Packer et al., 2010).

While being also cold-formed and sealed using ERW, the CSA G40.20/G40.21 specification has more stringent geometric restrictions on the mass, area and wall thickness, resulting in a design wall thickness that matches the nominal wall thickness. Additionally, five toughness categories exist to meet the CVN toughness requirement which makes it more suitable for critical welding (Packer et al., 2010).

In the United States, a new ASTM standard, ASTM A1085 (ASTM, 2022), for HSS profiles was recently produced. Except for a maximum yield strength value of 485 MPa, the criteria in this standard are equivalent to those defined in CSA G40.21-350W HSS. It has also stringent geometric restrictions which allows engineers to disregard the reduction of the thickness of the wall.

2.3 Slotted-Hidden-Gap (SHG) connection

In the industry, a commonly employed connection for linking hollow braces to beam-to-column joints is a slotted member with a gusset plate inserted, which is then welded together using four fillet weld lines, as depicted in Figure 6a. The slot in the HSS is usually longer than the length required to insert the gusset plate in order to allow execution tolerances during erection of the structure. Hence, a space between the end of the gusset plate and the end of the slot is left. This distance reveals an apparent net section in the bracing member where fracture is frequently localized near the slot. The latter problem is amplified by shear lag effects, where uneven stress distribution occur at the end of the welds, near the slot due to unconnected parts of the connection. As a result, it is impractical to adhere to the capacity design principle which aims to protect the connections to allow the HSS profile to yield and dissipate seismic energy.

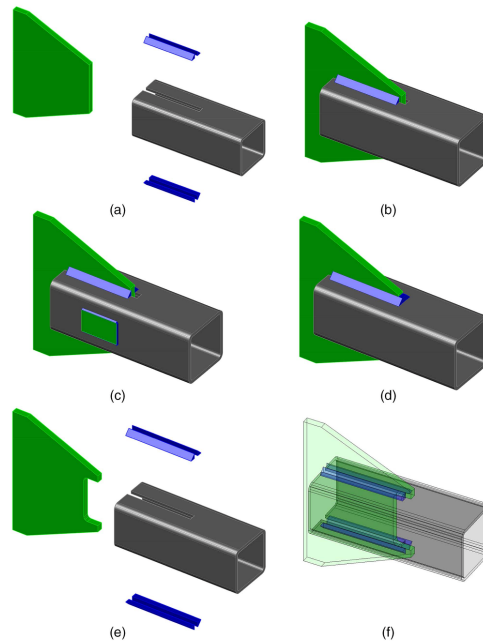


Figure 6: a) b) conventional connection (CC), c) CC with reinforcing plates, d) CC with return welds, e) f) SHG connection (Figure courtesy of Afifi (2021))

Although the shear lag effects can be accounted for the design process by computing the effective net area of the brace using a shear lag factor U in the CSA S16-19 (CSA, 2019) § 12.3.3, the need of reinforcement is necessary to prevent failure at the net section. Currently, the solutions that have been proposed and used are either reinforcement plates welded onto the HSS member on each side, parallel to the gusset plate or return welds as shown respectively in Figure 6c and 6d. According to Haddad et al. (2011), welded cover plates have proven to be effective in redistributing stresses along the member. This is achieved through an increase in the net section area, which helps prevent premature fracture during tension loading cycles. However, additional time to design and cost for the material and manufacturing make it cost-ineffective. Return welds allow for an increase in the ductility before the brace fractures at mid-length. Yet, welding implies a significant temperature gradient during manufacturing leading to the build-up of residual stresses. For this reason, the region surrounding the weld can be subjected to premature fracture and is therefore unsuitable for seismic action. Moreover, it requires strict quality control if the connections are welded on construction sites. Consequently, these reinforcement methods are either economically impractical or unsuitable for the intended purpose.

2.3.1 Background

Mitsui et al. (1985) examined several approaches to address the weld defects and subsequent cracks that can occur at the end of the welds in conventional connections involving circular section tubes. The wrapped-around welds, the reinforcing plates and the extended plate configuration are the solutions suggested. The latter is constructed by cutting a notch in the gusset plate and extending parts of the gusset plate over the tube to fill the gap left by the tube. As a result, the fillet welds begin on the gross area of the tube, shifting the stress concentration away from any weld defects. Based on the results of Mitsui et al. (1985), the Architectural Institute of Japan (AIJ, 2002) established design guidelines for the extended plate arrangement for circular tubes. The slot length in the gusset plate is specified to be twice the thickness of the gusset plate, with a maximum gap length of 6 mm. In order to prevent shear lag effects, the length of the weld must be more than or equal to 1.2 times the outer diameter of the tube. This arrangement demonstrated the ability of an HSS tube to endure overall yielding while avoiding net-section fracture and without the requirement for connection reinforcement.

A research program conducted by Martinez-Saucedo (2007) and Martinez-Saucedo et al. (2008) focused on the SHG connection, formerly called the Modified-Hidden-Gap (MHG) connection for seismic application using ASTM A 500 B/C on Circular Hollow Sections (CHS). FEA and full-scale laboratory tests of one conventional and two SHG connections were carried out under quasi-static tension and cyclic loading. It was concluded that by extending the flaps of the gusset plate, creating a gap between the end of the plate's slot and the end of the slot of the hollow section allows the relocation of the inelastic strains away from the connection favouring fracture at mid-length of the bracing member.

Three years later, large-scale reversed-cyclic tests were carried out on CHS braces by Packer et al. (2010) using the SHG connection. The research program included several manufacturing processes considering cold-formed, heat-treated and hot-finished state on four different braces of same external diameter. ASTM A500 grade C and S355J2H from Europe were chosen. It was demonstrated that the SHG connection performed properly in all four specimens without any fracture occurring at the

welds.

In 2014, Moreau (2014) also studied conventional and SHG connections through numerical simulations and experimental laboratory tests using Square Hollow Sections (SHS) using two HSS sizes (HSS 152 152 9.5 and HSS 203 203 13) under monotonic tension and cyclic loading including a full-brace test. The material used was CSA G40.20-21 350 W Class C for the HSS tubes. The objective was to find the minimum overlap length, i.e. the extended weld length after the end of the HSS slot. As a result of this study, it was observed that localization of strains occurred at the net section of the brace for conventional connections ($L_{wg}/L_w = 0$), where uniform stress distribution appeared away from the connection. In contrast, by increasing the overlap length L_{wg} (Figure 7) up to an ideal value, the inelastic axial deformations dropped at the welds. Once the optimal overlap length is exceeded, the localization of strains increased again due to flexure of the gusset plate's flap. A minimum overlap length of 5% allowed the yield resistance to be reached on the gross area of the SHG HSS brace members subjected to a monotonic tensile loading.

Following the research on SHS, Afifi (2021) probed deeper to identify the geometric parameters and material properties that influence the SHG connection. Extensive Finite Element Analyses (FEA) and experimental tests were conducted using ASTM A1085 square HSS members under monotonic tensile and cyclic loading. The weld overlap length was identified as the most significant variable when designing the SHG connection. Other variables such as the width and thickness of the HSS, the weld size and length and the gap length also influence the performance of the connection. Furthermore, it was shown that the use of smaller size but longer welds allowed to reach higher tensile forces before fracture by means of a more even stress distribution in the brace. The overlap length of 5% was confirmed to allow the brace to reach the maximum yield tensile resistance when subjected to a monotonic tensile loading. A load transfer analysis between the components of the connection has revealed a more uneven transfer mechanism for the conventional connection in comparison to the SHG connection. The SHG connection exhibits a higher load participation of fillet welds, ensuring a more uniform distribution of the forces.

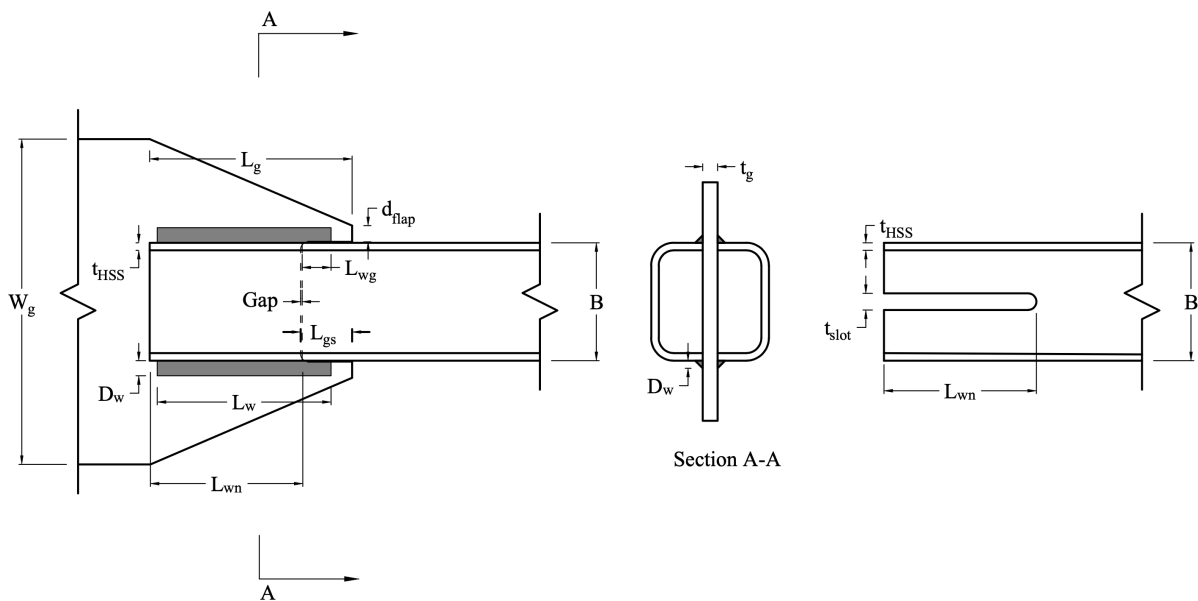


Figure 7: Dimensions of the SHG connection

2.3.2 Design and detailing methodology

Affi et al. (2023) proposed a design methodology to construct the SHG connection in accordance with the CSA S16-19 (CSA, 2019) provision following the results from parametric studies. Herein, the suggested design steps are based chiefly on a tensile behaviour of the connection. Therefore, the compressive behaviour of the gusset plate in particular has not been accounted for this approach. The design methodology starts with the selection of the weld length L_w , and from this property, other dimensions such as the fillet weld size D_w , the gusset plate width and thickness, respectively W_g and t_g and the depth of plate flap d_{flap} are computed. The process is iterative, following a typical design approach, where modifying one variable necessitates updating the others based on the newly calculated value.

The weld length is determined to avoid a block-shear rupture of the HSS member. A simplified version of the equation can be obtained by neglecting the tensile component as the net section area in the HSS can be small. The factored resistance for a potential failure in shear can be equalized to the probable brace resistance in tension as specified by the CSA S16-19 (CSA, 2019) § 13.11. Equation 13 can be rearranged to obtain Equation 14 that provides L_w , where the shear area is equal to $A_{gv} = 4 \cdot L_w \cdot t_{HSS}$. A resistance factor $\phi = 0.90$ is also applied for structural steel as specified in the CSA S16 (CSA, 2019).

$$A_g \cdot R_y \cdot F_y = 0.6 \cdot A_{gv} \cdot R_t \cdot F_u \quad (13)$$

$$L_w = \frac{A_g \cdot R_y \cdot F_y}{\phi \cdot 0.6 \cdot 4 \cdot t_{HSS} \cdot R_t \cdot F_u} \quad (14)$$

Based on the Whitmore section, the width W_g of the gusset plate can be computed according Equation 15. Using the probable tensile resistance of the brace, the gusset plate's thickness is obtained following Equation 16.

$$W_g = 2 \cdot L_w \cdot \tan(30^\circ) + B \quad (15)$$

$$t_g = \frac{A_g \cdot R_y \cdot F_y}{\phi \cdot W_g \cdot F_{y,gusset}} \quad (16)$$

Equation 17 provides the weld size. It should be taken as the maximum value to avoid base-metal fracture, the failure of the weld-to-HSS and weld-to-gusset plate.

$$D_w = \max \left(\frac{A_g \cdot R_y \cdot F_y}{0.67 \cdot \phi_w \cdot 4 \cdot L_w \cdot F_{u,GP}}; \frac{A_g \cdot R_y \cdot F_y}{0.67 \cdot \phi_w \cdot 4 \cdot L_w \cdot F_{u,HSS}}; \frac{A_g \cdot R_y \cdot F_y}{0.67 \cdot \phi_w \cdot 4 \cdot L_w \cdot \frac{\sqrt{2}}{2} \cdot X_u} \right) \quad (17)$$

The minimum depth of the plate flap is designed to avoid rotations while subjected to tension, and is computed according to the Equation 19. It can be modeled by a cantilever of a rectangle parallelepiped where the inertia is computed according to Equation 18. The force P is the difference between the net section fracture and the gross area yielding, respectively T_u and T_y , that is distributed equally to each flap.

$$I = \frac{t_g \cdot d_{flap}^3}{12} \quad (18)$$

$$d_{flap} = \sqrt[3]{\frac{12 \cdot \frac{T_u - T_y}{2} \cdot (L_{gap} + L_{wg})^3}{3 \cdot E \cdot t_g}} \quad (19)$$

The minimum weld overlap length L_{wg} can be determined through two approaches. Firstly, it can be calculated using shear lag properties outlined in the CSA S16-19 (CSA, 2019) according to Equation 20. Alternatively, it can be selected to ensure adequate shear resistance against the difference between the net section fracture and gross area yielding of the HSS member as shown in Equation 22.

$$L_{wg} \geq \frac{A_{ne}}{A_g} \cdot t_{slot} \quad (20)$$

with

$$\frac{A_{ne}}{A_g} \geq 0.7, \frac{\frac{L_{wg}}{t_{slot}}}{\frac{A_{ne}}{A_g}} \geq 1 \quad (21)$$

$$L_{wg} \geq \frac{T_r - T_{prob}}{\phi \cdot 0.67 \cdot (4D_w) \cdot F_u} \quad (22)$$

Referring to Figure 7, the other detailing parameters can be computed according to Equation 23, where the tolerance L_{tol} is typically chosen to be 15 mm.

$$L_{wn} = L_g - L_{tol} - L_{wg}; L_{gs} = L_{wg} + L_{tol} + L_{gap}; t_{slot} = t_g + 3; W_{gs} = B + 3 \quad (23)$$

2.4 Compressive behaviour of gusset plates

Gusset plates connections are used ubiquitously in steel structures as member joints. Designed to transfer the loads from the bracing to framing elements, they must also withstand significant inelastic deformations and accommodate end rotations due to bending of the diagonal member when subjected to a large ground motion while maintaining the axial resistance of the brace. When detailed properly, out-of-plane deformations must be permitted to allow the brace to fulfill its role of fuse element. This system that follows capacity design requirements can be also called "strong gusset - weak brace" approach (Haddad et al., 2011). Recent seismic activity, however, has demonstrated that bracing systems are vulnerable to significant failure when an intense seismic event takes place. Bracing systems failure have been documented during previous earthquakes such as in Northridge in 1994 and Kobe in 1995 (J. B. Shaback, 2001; Yamamoto et al., 1988). During tensile cycles, gusset tearing, gusset net section and weld fractures have been observed as typical failure modes while buckling of the gusset plate may occur in compression when not properly designed (Skalomenos et al., 2018).

Astaneh-Asl et al. (1985) investigated nine full-scale test specimens under severe cyclic loading. One of these findings suggests integrating a free distance between the end of the bracing members in the

gusset plate and the imaginary line of constraint defined by the framing elements of at least twice the plate's thickness. It aims to allow a plastic hinge to form in that area. The latter practice design concept has been incorporated in the American Institute of Steel Construction (AISC 360-10) (AISC, 2010) in addition to other capacity design requirements such as restricting bracing configurations to prevent undesirable inelastic deformation, restricting global slenderness and width-to-thickness ratios of the braces to maintain a ductile behaviour, requiring connections to develop the anticipated brace capacity and to handle the brace's end rotation (Sen et al., 2016). Later, Lehman et al. (2008) and Roeder et al. (2005) developed a balanced design methodology to enhance the seismic behaviour of CBFs. It consists of prioritizing the yield mechanisms in a sequence where the least favourable failure modes may occur last. This is achieved by having expected resistances of the members lower than the capacity of the connection. A linear clearance distance of $2t_g$ can lead to massive and uneconomic gusset plate geometries for a rectangular plate, hence their research programs also included elliptical clearances rule of 3, 6, 7 and $8t_g$, which enable more flexible and compact gusset plates geometries. It has been demonstrated that employing the largest elliptical offset of $8t_g$ offers higher system ductility and deformation capacity without any notable differences in strains observed at the mid-length of the brace. These clearances are shown in Figure 8.

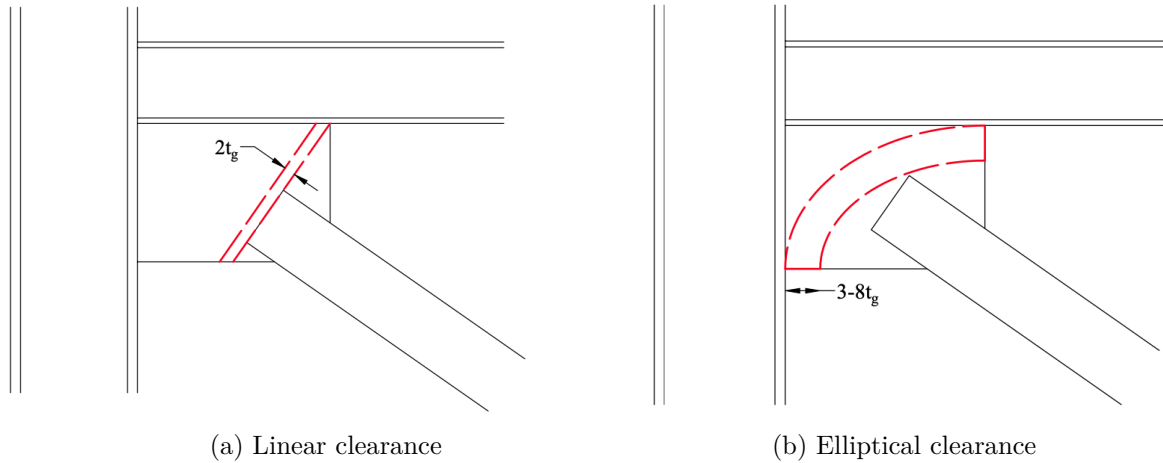


Figure 8: Clearance rules

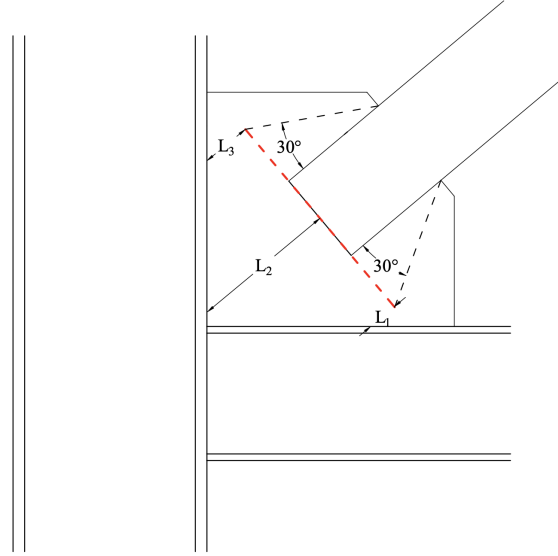


Figure 9: Whitmore's section

Currently, the Canadian Standard CSA S16-19 (CSA, 2019) lacks any explicit design recommendations or requirements despite the fact that many steel structures employ gusset plate connections. The traditional design approach relies on the verification of stresses at the Whitmore's section in compression. The Whitmore's width is defined by the line provided by the intersection between extended lines drawn at 30° from the brace and a perpendicular line at the end of the brace as illustrated in Figure 9. The Whitmore's section is given by the product of the Whitmore's width and the thickness of the gusset plate. The buckling of the plate can be also verified using an adapted version of the Euler buckling load (Equation 24) with strips denoted L_1 , L_2 and L_3 based on the Whitmore section as shown in Figure 9.

$$N_{cr,gs} = \frac{\pi^2 \cdot E \cdot I_{Whitmore}}{(kL)^2} \quad (24)$$

With

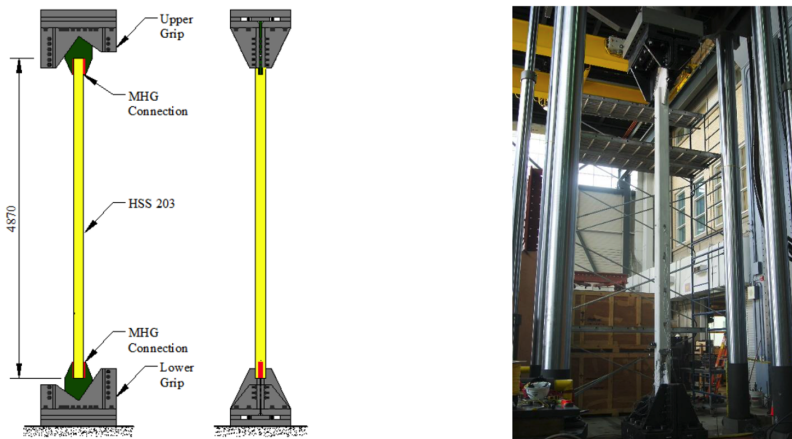
$$L = \max \left(L_2; \frac{L_1 + L_2 + L_3}{3} \right) \quad (25)$$

3 Calibration of FE model against test result

The objective of this section is to establish a Finite Element Model (FEM) that will serve as the basis for conducting a parametric study (see Section 4). The goal will be achieved by calibrating the FE model to the results of the experimental test of the full-brace under cyclic loading conducted by Moreau (2014). The aim is to evaluate the global response by using the force-displacement relationship, i.e. the chosen verification criterion of the behaviour of the FE model and the results of the experimental test in order to assess the accuracy of the FE model. All numerical models are analyzed using the commercial finite element program Abaqus/CAE 2022 (Simulia, 2022). The geometry of the brace and connections are designed first in AutoCAD 2023 (AutoDesk, 2023) and imported into the finite element software before the modelling and the analysis. In order to achieve the most accurate results, the characteristics of the FE model such as the boundary conditions, the geometry, the material properties and the loading were chosen to recreate realistically the conditions of the laboratory experiment.

3.1 Laboratory-tested full-brace

The full-brace specimen (called "Specimen 12" in the research program) tested by Moreau (2014) comprised of a HSS 203 203 13 with an overlap length ratio of L_{wg}/L_w of 15 %. The length of the HSS member is 4870 mm and it simulates a brace to a frame of 3.3 m in height and 4.7 m in width with an inclination of 35° to the horizontal. Two times the thickness of the gusset plate ($2t_g$) of linear clearance was left between the brace's end and the line of constraint of the plate in order to allow rotation of the gusset plate when the brace was flexed under compression loading. The HSS member was connected to the gusset plate using four fillet welds with a length of 310 mm using a SHG connection at each end secured by two grips. Figure 10a illustrates a schematic drawing of the full-brace configuration, showcasing the SHG connections at both ends along with identical upper and lower grip assemblies. In addition, Figure 10b provides a visual representation of the experimental setup in the laboratory. A more detailed description of the test setup and measurement procedure is provided by Moreau (2014).



(a) Schematic drawing of the brace specimen (b) Photograph of the laboratory test

Figure 10: Full scale brace Specimen 12 tested by Moreau (2014) (Figures courtesy of Moreau (2014))

The brace from Specimen 12 was fabricated with a grade CSA G40.20-12 350 W Class C with theoretical and measured properties listed in Table 5. Gusset plates were fabricated from ASTM A572 (ASTM, 2011) steel as shown in Table 6. The length and the size of the welds were chosen accordingly to avoid tensile, block-shear rupture of the brace and to avoid the welds from failing according to the methodology described in Section 2.3.2. All geometric properties are listed in Table 7. The global slenderness and width-to-thickness ratio of the HSS are compliant with the limits provided in the CSA S16 (CSA, 2019) and the values are respectively provided in Equations 26 and 27.

Table 5: Material properties of Specimen 12's HSS tube

Material Properties [MPa]	Theoretical	Measured
E	200'000	214'000
F_y	350	416
F_u	450	472

Table 6: Grades of each element of Specimen 12

Member	Grade
Brace	CSA G40.20-21 350 W Class C
Gusset plates	ASTM A572 Gr. 50

Table 7: Measured geometric properties of the Specimen 12

HSS size	A_g [mm ²]	L_b [mm]	L_{wg} [mm]	L_w [mm]	$\frac{L_{gw}}{L_w}$ [%]	D_w [mm]	t_g [mm]	W_g [mm]
HSS 203 203 13	9260	4870	47	310	15	25	25.4	560

$$\frac{KL}{r} = \frac{0.9 \cdot (4870 + 4 \cdot 25.4)}{76.3} = 57 \leq 100 \quad (26)$$

$$\frac{B}{t_{HSS}} = \frac{203}{13} = 15.6 \leq \frac{330}{\sqrt{F_y}} = \frac{330}{\sqrt{350}} = 17.6 \quad (27)$$

The true stress-strain relationships for the gusset plates, the HSS walls and corners shown in Figure 11 are the result of a conversion from engineering stress-strain to true stress-strain relationship. The engineering stresses and strains are determined by averaging the results of several coupons tests extracted from the HSS walls. Physical tests and FE models were used for this purpose. In order to obtain the material properties for the HSS corners, modification factors provided by Koval (2018) were used from the true stress-strain of the HSS walls by Moreau (2014). The conversion of the calculations are provided in Moreau (2014). Moreover, the behaviour of the material used for the welds is not available, hence, the true stress-strain relationship from the brace member has been used for the weld metal.

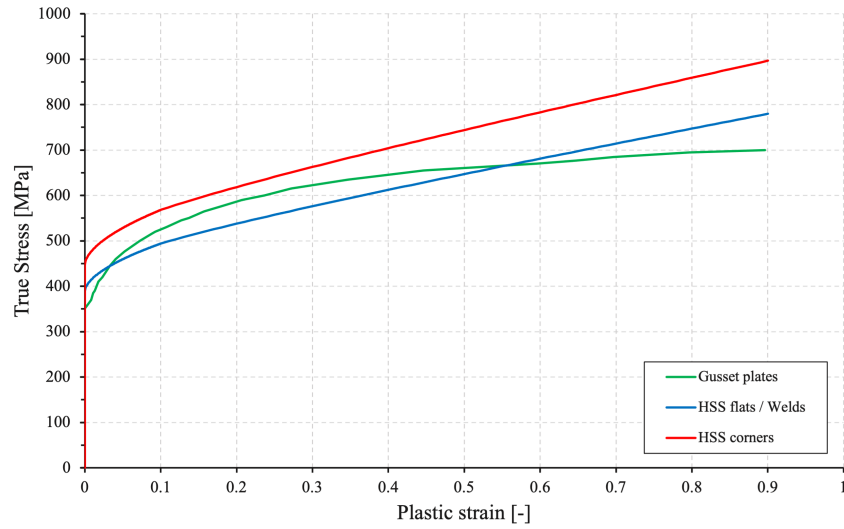


Figure 11: True stress-strain relationships for gusset plates, HSS tube and welds

Prior studies mainly subjected the SHG connections to quasi-static or cyclic loading with lower amplitude displacements. Therefore, an asymmetrical tensile-dominant cyclic loading history was applied to the full brace. After 9.5 cycles, a tensile displacement corresponding to an Interstorey Drift Ratio (IDR) of 3.1 % was applied to subject the SHG connection to a significant tensile demand that may happen during a ground motion that is close to a fault. The second part expresses a far-field history represented by a reversed cyclic loading with symmetrical amplitudes shown in Figure 13. This loading protocol dominated by a tensile response allows the brace and its connections to be subjected to larger demand than previous laboratory tests. The amplitudes have been converted to IDR $\frac{\Delta}{h_s}$ according to Equation 28, assuming a diagonal length from centerline to centerline of the beam-to-columns joints of $L_{cc} = 1.3 \cdot L_H$, where $L_H = L_B + 2 \cdot t_g$. Those variables are shown in Figure 12.

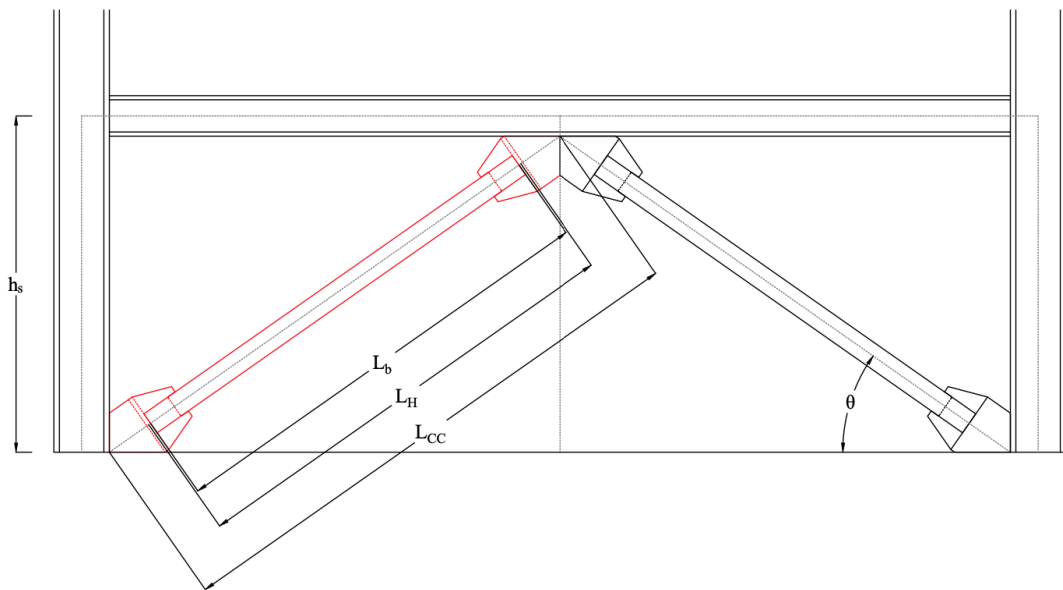


Figure 12: Schematic drawing of the inverted V-bracing frame with SHG connections

$$\frac{\delta}{L_H} = 1.3 \cdot \sin(\theta) \cdot \cos(\theta) \cdot \frac{\Delta}{h_s} \quad (28)$$

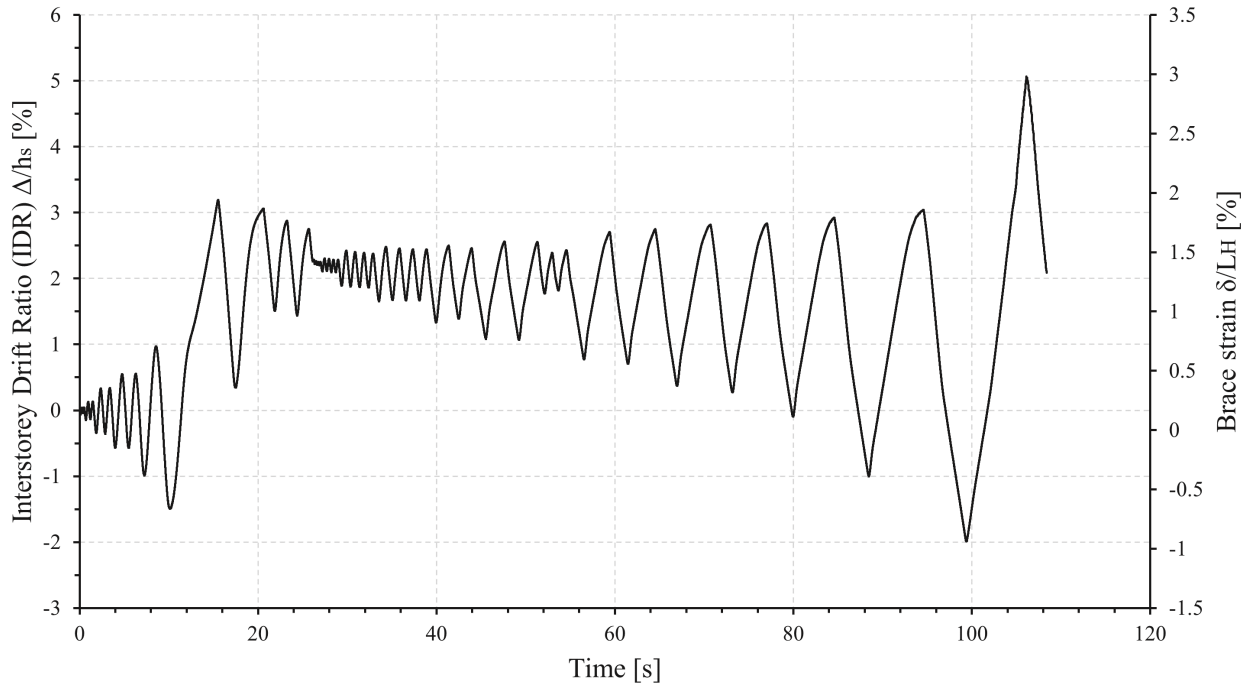


Figure 13: Tensile-dominated loading protocol

3.2 Finite Element Model (FEM)

The FE model is built to represent the laboratory-tested specimen, using the same geometry, material properties and boundary conditions as Specimen 12 tested by Moreau (2014). Figure 14 depicts the visual representation of the numerical model, showcasing the brace, its SHG connections at both ends, and the gusset plates. Partitioning has been drawn according to the grip geometry of the test elaborated in the laboratory and the datum planes (dashed yellow lines) represent the outer edges of the beams and columns flanges. The detailed description and assumptions used to develop the numerical models are presented in Section 3.2.1, following the sequential order of the steps employed in constructing the numerical model in the software.

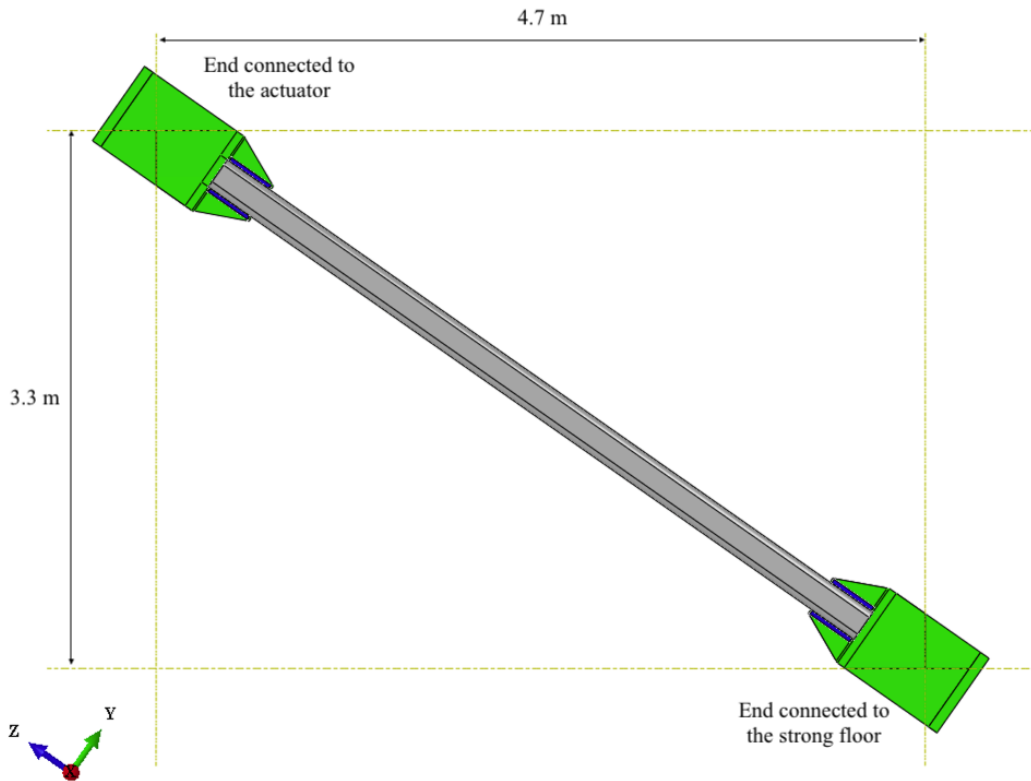


Figure 14: Visual representation of the FE model

3.2.1 Detailed description of the FE model

Geometry In contrast to prior numerical simulations from Afifi (2021) and Moreau (2014), quarter of half models are not utilized as they are not able to capture the effect of geometric imperfections on the force-deformation response. Instead, a full-brace model (Figure 14) has been generated to account for residual stresses and buckling of the brace when subjected to a compressive force. In order to accurately replicate the Specimen 12, AutoCad (AutoDesk, 2023) drawings were utilized to create the geometry of the full-brace, incorporating the measurements obtained from the tested specimen. Since the aim is not to reproduce measurements from a specific physical test, the geometries of the numerical models in the parametric study are directly defined in Abaqus (Simulia, 2022) to ensure simplicity.

Residual stress and geometric imperfections The cold-forming manufacturing process is accounted in the model by inputting an asymmetrical residual stress pattern to model the residual stress caused by the seam weld to close the cross-section. Although Koval (2018) collected and examined residual stress data of cold-formed HSS over the previous 60 years on ASTM A500, ASTM A1085 and CSA G40.20-21 350 W specifications, the considered HSS were seamless. Therefore, a longitudinal residual stress distribution from Suzuki and Lignos (2020) has been incorporated in the model using predefined fields in the initial step assuming one seam weld on one the of the plain HSS walls. Peak values at the seam weld are taken as $1.0 \cdot F_y$ and decrease linearly to $-0.30 \cdot F_y$ in the corners of the brace as depicted in Figure 15. On the other hand, the transverse residual model is taken from Koval (2018) and varies through the thickness between $-0.6 \cdot F_y$ to $+0.6 \cdot F_y$ where the outer surface of the HSS is in tension and the inner surface in compression. However, the temperature gradient caused by the fillet welds between the HSS profile and the gusset plate has not been modeled for simplicity. It is suggested for further research to incorporate that effect in the study.

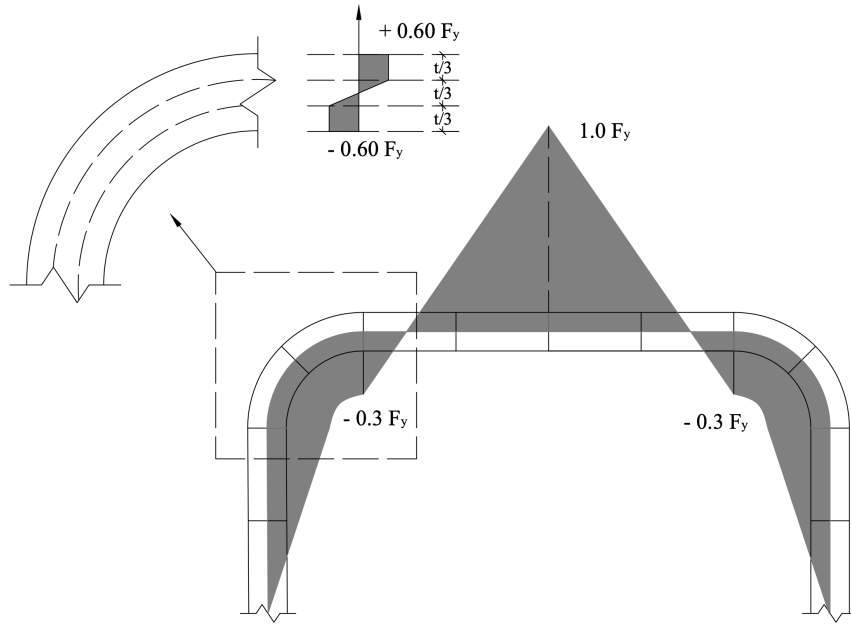


Figure 15: Longitudinal and transverse residual stress distributions of the HSS

As the initial imperfection significantly influence the global behaviour of the brace, it must be accounted in the model. A buckling analysis is performed beforehand where the first eigenmode is considered. The results of this analysis (Figure 16) were integrated by adjusting the nodal coordinates of the HSS through scaling the corresponding buckling mode shape according to tolerances obtained in the manufacturing process of the steel members. The CSA S16-19 (CSA, 2019) § 28.6.4 suggests that the out-of-straightness should not exceed $L_{brace}/1000$. For this model, the factor is equal to 4.86. Therefore, the latter value is used to scale the deformed shaped obtained from the buckling analysis.

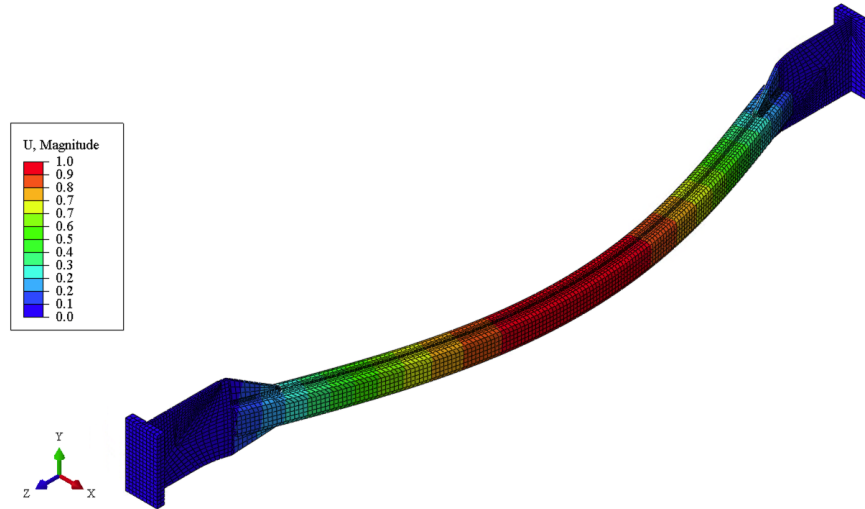


Figure 16: Results from the buckling analysis (first eigenmode)

Boundary conditions and loading The boundary conditions aim to replicate the behaviour of the end conditions of the Specimen 12. Figure 17 illustrates a photograph of the bottom grip used for the tested specimen of the full-brace. Due to the unrestricted rotation capacity of the grips around the brace axis, all rotational Degrees Of Freedom (DoFs) are allowed in the three directions for both ends. On the other hand, all translational DoFs are constrained on the strong floor structure side. The axial force is applied as a unit displacement following the loading protocol (Figure 13) on the end side that simulates the location where the actuator is applied. Figure 18 provides an overview of the boundary conditions and highlights their application on the green surfaces.

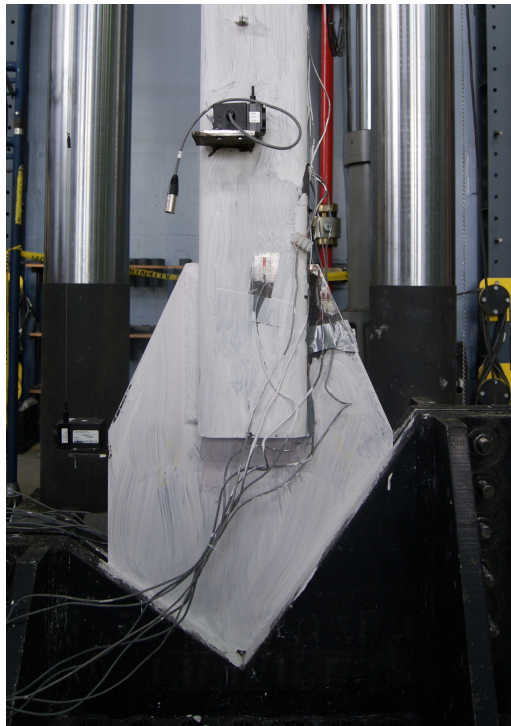


Figure 17: Photograph of the bottom grip of Specimen 12 by Moreau (2014)

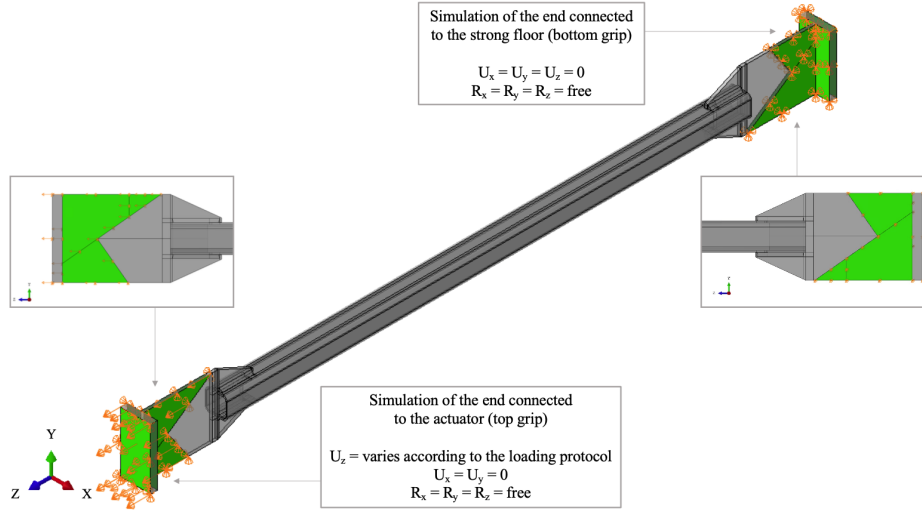


Figure 18: Boundary conditions of the FE model

Material model Although there is an abundance of tensile test data available for structural steels, the insights provided by monotonic loading as shown in Figure 11 are constrained in terms of understanding the material's characteristics. It is important to note that crucial aspects of the material's inelastic response to cyclic loading, such as the Bauschinger effect, cannot be accurately determined without conducting tests using a load reversal protocol. Hence, the material plasticity is modeled with a combined hardening model with half cycle data type with three backstresses based on a refined version of the Voce-Chaboche constitutive model (Chaboche et al., 1979; Voce, 1948) proposed by Hartloper et al. (2021). The model is integrated in the material properties, where the two parameters of interest are Q_∞ which represents the maximum change in the yield surface size and b which describes the rate of the evolution of the yield surface with the equivalent plastic strain. Those factors depend on the chemical composition of the steel grade among other variables. Although the specific CSA G40.20-21 350 W and A572 grades for the HSS and gusset plates, respectively, were not studied directly by the researchers, a comparison was made between their chemical compositions and the ASTM A500 studied by Hartloper et al. (2021). The chemical composition comparison based on a heat analysis is provided in Appendix 7.2 and are based on the ASTM 500 (ASTM, 2003), ASTM A572 (ASTM, 2011), ASTM A1085 (ASTM, 2022) and CSA G40.20-21 (CSA, 2009). It was determined that the CSA G40.20-21 350 W and ASTM A572 grades lack substantial similarity compared to the ASTM A500 specification. Therefore, the parameters Q_∞ and b were not included in the numerical model created for the calibration with the Specimen 12 but will be considered for the parametric study as the specification ASTM A1085 is used for the HSS tubes.

Constraints Tie constraints are utilized to connect two surfaces during a simulation, ensuring that each node of the slave surface moves in the same manner as the corresponding point on the master surface to which it is connected according to the Abaqus Documentation (Simulia, 2012). They have been implemented between each fillet weld and HSS and gusset plates. The weld surfaces have been designated as the master surfaces as is it stiffer than the gusset plate, while the other interface (either the HSS or gusset plate's surface) is considered as the slave surface.

Mesh type and size A solid 20-node brick quadratic mesh element C3D20R is utilized in the FE model thanks to numerous benefits it provides such as a large deformation capacity and higher order shape functions compared to linear elements. The latter benefit allows to estimate with more accuracy curved borders of irregularly shaped geometries. The reduced integration also helps to speed up the computational time without losing too much accuracy. Unlike linear mesh element such as C3D8R type, it is not affected by locking issues (Logan, 2007). It is crucial for the buckling analysis model and the main model to share the same mesh.

The mesh size was established based on the calibration study conducted by Afifi (2021), which involved performing a mesh sensitivity analysis. In order to accurately capture the characteristics of the weld region, a finer mesh is employed. This finer mesh provides several benefits, including enhanced accuracy, improved representation of small-scale features, and increased ability to capture localized effects. The sizes are summarized in Table 8 and Figure 19 provides a visual representation of the mesh applied to the full brace, with a closer look at the connection and gusset plate. Datum planes were employed to partition the components, ensuring a regular mesh that adheres to the geometry of the grips, as well as the slots in the HSS tube and gusset plates.

In addition, a standard solver was employed capable of handling linear, nonlinear, static, and dynamic problems. The standard solver resolves a system of equations implicitly at each increment, whereas an explicit solver is better suited for handling impacts problems and computes the solution incrementally forward in time using smaller time steps, without solving a coupled system of equations at each increment (Simulia, 2012).

Table 8: Mesh size of the elements

Parts	Mesh size (size x number of elements through the thickness)
Gusset plates	20 x 2
HSS	35 x 2
Welds	4 x -

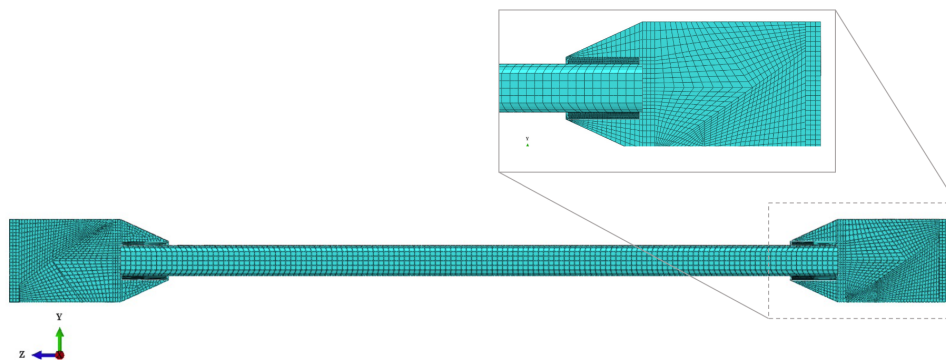


Figure 19: Global and local mesh of the HSS brace and its SHG connections

Fracture model Since the study does not incorporate a fracture model, the equivalent plastic strain (PEEQ) is utilized as a criterion for determining fracture. Specifically, in the critical area where the tested full-brace fractures at mid-length, a PEEQ value equal to unity at this location is indicative of bracing member fracture as reported by Zhao et al. (2009).

3.3 SHG connection subjected to cyclic loading

The results obtained from the Specimen 12 tested in the laboratory by Moreau (2014) and the results from the FE model are plotted in Figure 20. The proposed FE model is validated with the experimental data of the Specimen 12 as it captures fairly accurately the ductility range and the yield limits, considering a global behaviour criterion where the force-displacement relationship is plotted. Both models have IDR varying between -1.8% to 2.9% before fracture. Table 9 summarizes key parameters of the laboratory test response. The experimental test exhibits a slightly stiffer behavior, which could potentially be attributed to a different residual stress pattern compared to the one employed in the numerical model. A maximum difference of 27 % between the post-buckling peaks can be explained by the theoretical as opposed to the measured account of the initial geometric imperfections employed in the FE model. As mentioned in the assumptions, greater accuracy could be achieved if the adapted parameters Q_∞ and b are incorporated in the material model for the CSA G40.20-21 (HSS) and ASTM A572 (gusset plate) specifications.

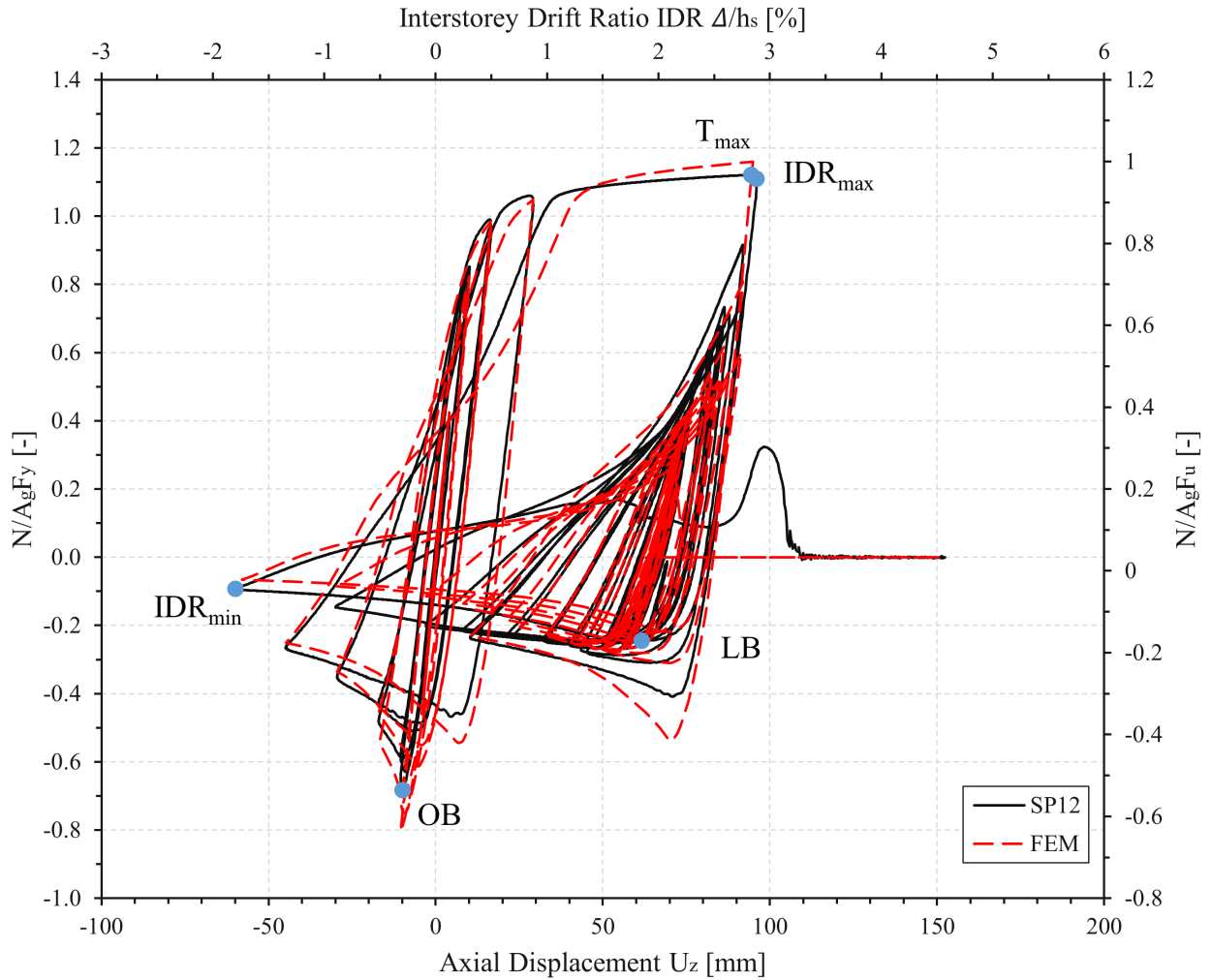


Figure 20: Force-displacement calibration of the FEM against the Specimen 12 with $\frac{KL}{r} = 57$ and $\frac{B}{t} = 15.6$

Table 9: Response parameters of Specimen 12

Response parameters	Time [s]	T [kN]	C [kN]	IDR [%]	U [mm]
Overall buckling (OB)	6.17	-	- 2631	-0.34	- 9.9
T_{max}	19.78	4318	-	3.30	94.5
IDR_{max}	19.88	4273	-	3.35	96.0
Local buckling (LB)	99.86	-	-947	2.15	61.7
IDR_{min}	103.77	-	-360	-2.09	-59.8

A time history provides a clearer view of the evolution of the axial load compared to a force-displacement hysteretic response, as there is no overlapping cycles. Figure 21 illustrates the time history response of Specimen 12 and the numerical model developed in Abaqus. Similarly to Figure 20, both models exhibit a similar overall response. However, it can be observed that between 30.4 and 33.8 seconds, the numerical model deviated from the protocol and skipped respectively 3 and 4 cycles at 1.4% and 1.5% drift. The reason for this deviation remains unclear.

Furthermore, it is notable that up to 21 seconds, the compressive force in the finite element model (FEM) is higher than that of the laboratory-tested specimen, as also shown in Figure 20. The trend reverses after 60 seconds, where the axial tensile force in Specimen 12 exceeds that of the FEM, which is also visible in Figure 20.

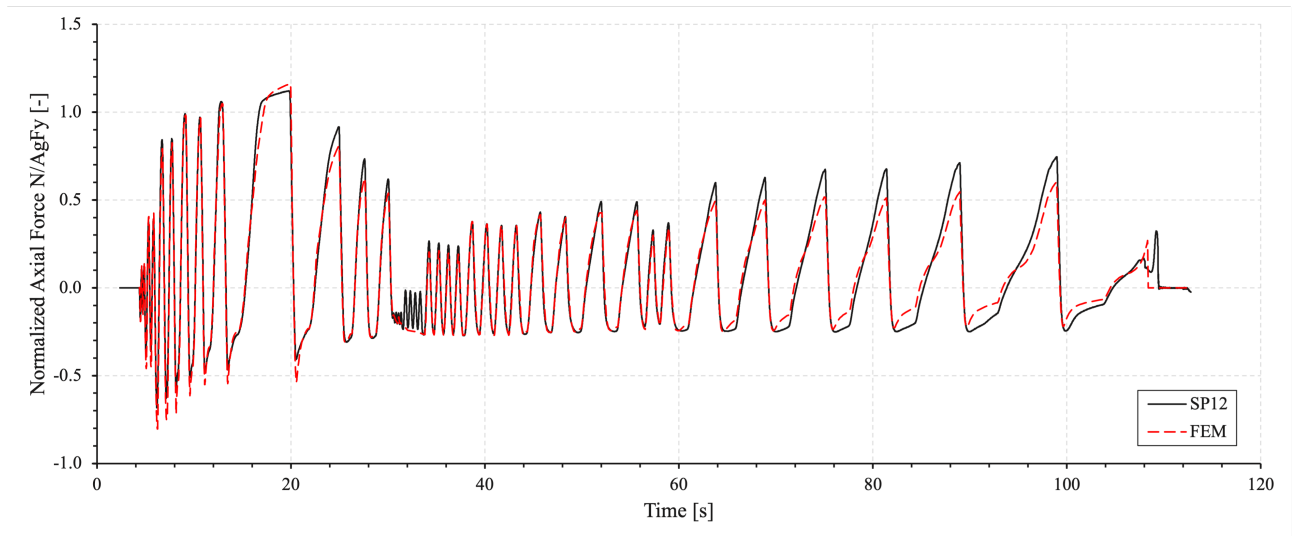


Figure 21: Comparison of the time histories of Specimen 12 and FEM

4 Study of the hinge zone of the gusset plate

In order to ensure that braces could yield in tension and buckle under compression when the building is subjected to a ground motion, it is crucial to detail properly their connection to the main frame to allow the member to fulfil its role of dissipative element. In cases of out-of-plane brace buckling, the gusset plate may experience weak axis bending due to end rotations of the member. The creation of plastic hinges in the plate allows post-buckled brace's end rotation to be accommodated at significant storey drifts. This section aims to assess the behaviour of the gusset plate under cyclic loading and its impact on the performance of the SHG connection. Several parameters are studied and varied, including the HSS size, weld configuration (short or long welds), brace's slenderness, and clearance rule (linear, elliptical or constrained), while maintaining a constant brace inclination to ensure a consistent loading protocol for all numerical models.

4.1 Brace and connection configurations

A total of twenty-one numerical models were generated and analyzed using Abaqus CAE/2022 (Simulia, 2022), with a SHG connection present at both ends of each model. The values of the studied parameters for each model are summarized in Table 10.

Table 10: Numerical models matrix

ID	HSS size	b_{el}/t [-]	L_{brace} [mm]	KL_H/r [-]	Weld Config. D_w, L_w [mm]	Gusset plate t_g, W_g [mm]	Offset
1AL1	HSS 127 127 6.4	15.1	4950	91.3	(A) 15, 200	13, 358	Linear $2t_g$
1AL2			5400	99.6	(B) 10, 250	10, 416	
1BL1			4950	91.3			
1BL2			5400	99.6			
2AL1	HSS 254 254 13	15.5	4950	45.5	(A) 30, 390	25, 705	Linear $2t_g$
2AL2			5400	49.6	(B) 25, 475	18, 797	
2BL1			4950	45.5			
2BL2			5400	49.6			
3AL1	HSS 305 305 16	15.8	4950	38.1	(A) 35, 440	33, 814	Linear $2t_g$
3AL2			5400	41.5	(B) 30, 515	24, 900	
3BL1			4950	38.1			
3BL2			5400	41.5			
1AC	HSS 127 127 6.4	15.1	4950	91.3	(A) 15, 200	13, 358	Constrained
1BC					(B) 10, 250	10, 416	Elliptical $8t_g$
1BE							
2AC	HSS 254 254 13	15.5	4950	45.5	(A) 30, 390	25, 705	Constrained
2BC					(B) 25, 475	18, 797	Elliptical $8t_g$
2BE							
3AC	HSS 305 305 16	15.8	4950	38.1	(A) 35, 440	33, 814	Constrained
3BC					(B) 30, 515	24, 900	Elliptical $8t_g$
3BE							

The model IDs have been chosen in such a way that 1, 2, 3 represent respectively the HSS 127 127 6.4, HSS 254 254 13 and HSS 305 305 16, L_1 and L_2 respectively denote a length of 4950 mm and 5400 mm, while A and B represent a weld configuration A (shorter-length large-size) or B (longer-length smaller-size), and C and E respectively indicates a constrained or elliptical hinge zone. The imaginary test setup is designed to simulate a single brace of an inverted V-bracing frame with a constant inclination of 35° of the brace (Figure 12). The choice is made to use a constant angle in order to apply the same loading protocol to all models although a slight variation in the heights is present (respectively 3400 mm and 3700 mm for a brace's length of 4950 mm and 5400 mm).

The HSS sizes were chosen based on typical brace sizes that can be found in practice (Afifi, 2021). Two different fillet weld configurations are implemented where configuration B is an equivalent longer-length smaller-size welds compared to the weld configuration A to assess the behaviour of the SHG connection. After considering Afifi's findings (Afifi et al., 2021), it was decided to maintain a consistent ratio of L_{wg}/L_w at 15%. The study revealed that a higher overlap length ratio significantly reduces the equivalent plastic strain (PEEQ) in the HSS slot region, but it also introduces higher demand near the gusset plate slot. Hence, an average value within the range studied by Afifi et al. (2021) (from 5% to 30%) has been selected. The selection of the global slenderness is based on the findings from the literature review conducted in Section 2.1.2. It was concluded that a stockier bracing member tends to experience higher concentrations of plastic deformation at plastic hinges when subjected to a compressive loading, leading to local buckling at critical locations. Therefore, it was chosen to adhere to the CSA S16-19 (CSA, 2019) § 27.5.3.2 a) to keep an overall slenderness limit under 100 in order to study the most critical cases. The design of the numerical models is based on the methodology outlined in Section 2.3.2.

In addition to the parameters incorporated in Afifi's design approach (Afifi et al., 2023), the geometry of the clearance in the gusset plate was introduced as an additional parameter in the numerical study. Figure 22 contains a visual representation of three degrees of confinement of the gusset plate : a linear, elliptical and constrained hinge zone. The elliptical offset follows the equations provided by Lehman et al. (2008) and the constrained configuration was determined arbitrarily, with the condition being to push the brace to its maximum extent toward the intersection of the brace and column, limiting the ability of the gusset to displace out-of-plane. Based on the work of Lehman et al. (2008), an elliptical gusset plate clearance model with an $8t_g$ offset distance provides greater system ductility and deformation capacity compared to smaller elliptical clearance, while also effectively delaying or restricting fracture occurrences in the welds or brace. For this reason, an offset of $8t_g$ was considered in this parametric study.

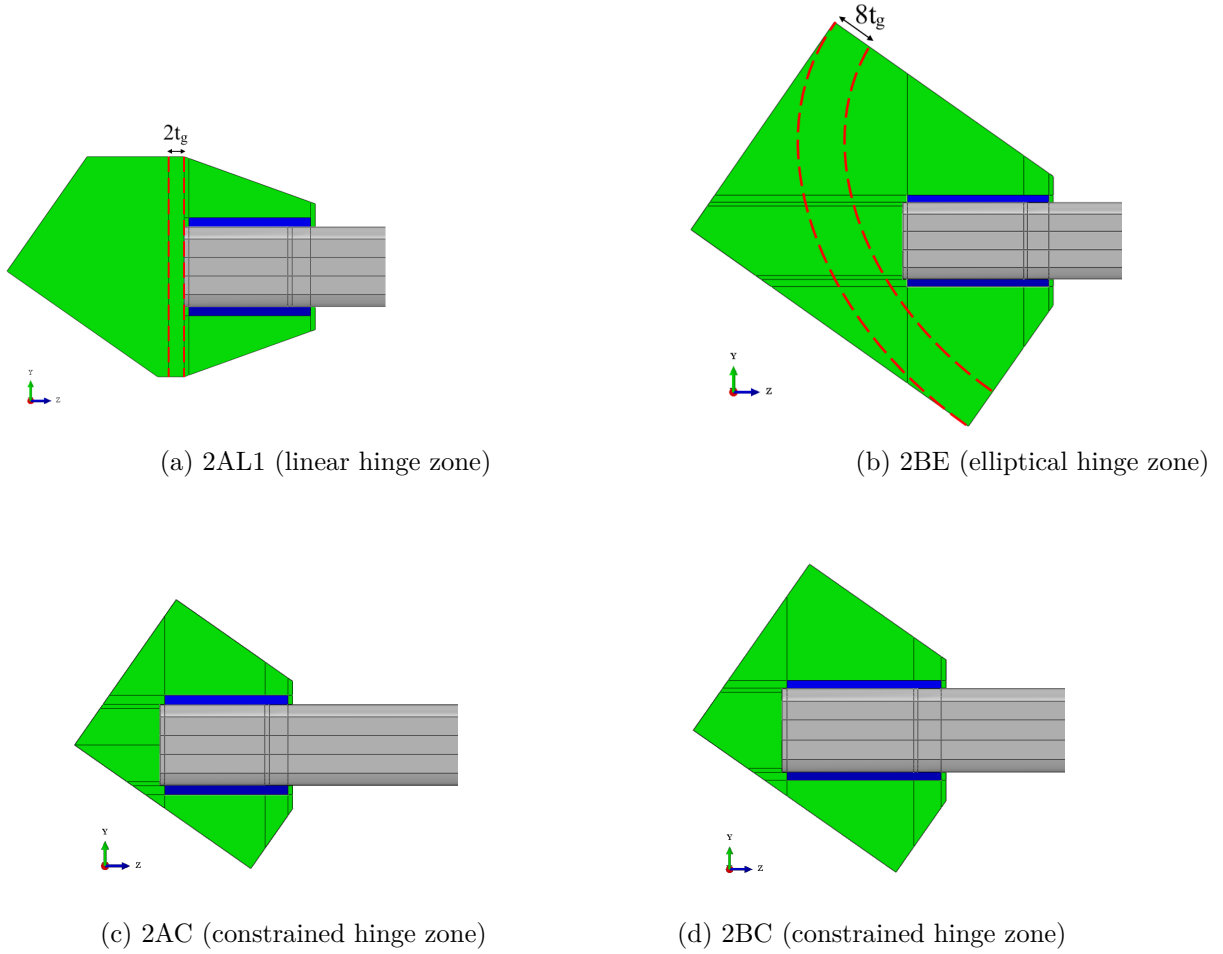


Figure 22: Degrees of confinement of the gusset plate for HSS 254 254 13

Following the design methodology suggested by Afifi et al. (2023), the net section fracture and block shear rupture have been verified for the HSS. Additionally, the block shear rupture has been verified for the gusset plate according to mode 1, mode 2 and mode 3 in tension (Appendix 7.1). In the case of compression, the design of the gusset plate takes into account the Whitmore section. Moreover, an additional verification has been included to ensure that the buckling of the gusset plate occurs after any potential fracture at the mid-length of the brace. The calculations were done following the CSA S16-19 (CSA, 2019) design provisions when applicable (Appendix 7.1).

4.2 Assumptions

The FE models developed for the parametric study incorporate identical boundary conditions, mesh types, and longitudinal and transverse residual stress patterns as the FE model utilized in the comparison presented in Section 3. The mesh size was adjusted according to the dimensions of the gusset plate and the length of the brace. Additionally, an elastic buckling analysis was conducted for each model to determine the shape of the initial geometric imperfections, and the obtained results of the node coordinates were scaled to respect a maximum lateral amplitude of $L_{brace}/1000$ and incorporated in the main analysis.

The main objective being the assessment of the compressive behaviour of the gusset plate while using a SHG connection, a reversed cyclic loading protocol is used in the parametric study instead of a tension-dominated loading protocol in contrast to the calibration conducted in Section 3. The standard protocol comes from Fell et al. (2009) where overall buckling is expected at a 0.2% drift after three times six cycles at low drift, followed by a smaller number of cycles of higher drifts where the maximum considered earthquake occur at a 4% drift. A summary of the number of cycles and drifts are provided in the Figure 23.

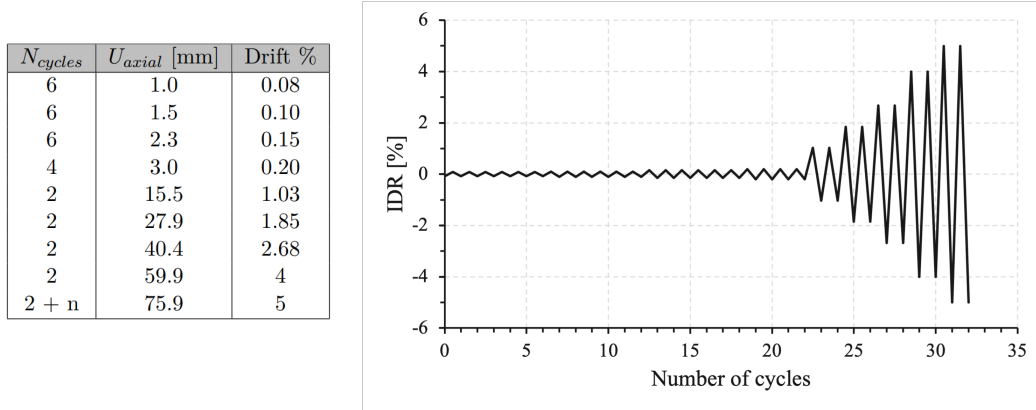


Figure 23: Loading protocol (IDR vs. cycles)

In order to obtain the loading protocol expressed in time along the horizontal axis (the loading protocol introduced in the software) as shown in Figure 24, a sine function is used to convert the number of cycles to time. The brace's strain is computed according to Equation 28. It is assumed that the material properties are rate-independant, thus the velocity applied on the hypothetical actuator holds minimal significance.

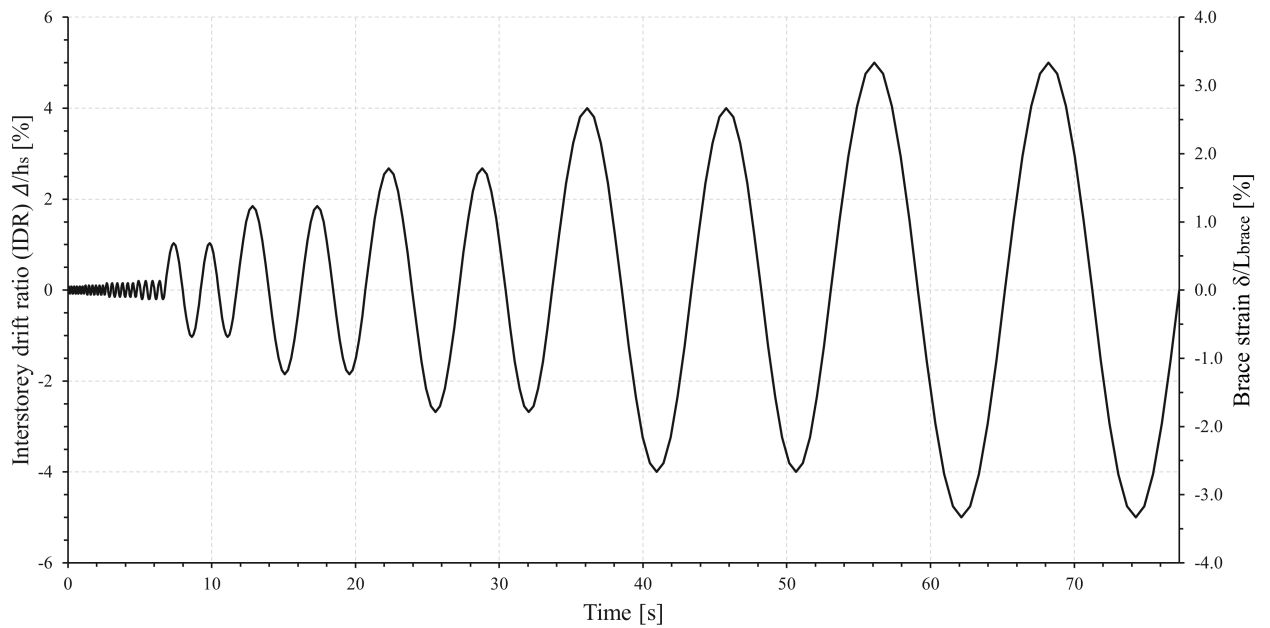


Figure 24: Loading protocol (IDR vs. time)

In the parametric study, the HSS tubes are made of ASTM A1085 steel replacing the CSA G40.20-21 350 W Class C used in the calibration study. As mentioned in the detailed description of the FE model of the comparison in Section 3, Appendix 7.2 compares the chemical composition of the different steel grades. It is determined that the ASTM A1085 and ASTM A500 grades exhibit sufficient similarity. Consequently, the parameters $Q_\infty = 228.02$ MPa and $b = 0.11$ obtained for ASTM A500 by Hartloper et al. (2021) can be applied to ASTM A1085 specification in the material model. However, those parameters are not applicable to ASTM A572 grade.

Table 11: Grades of each element of the parametric study's models

Member	Grade	F_y [MPa]	$R_y F_y$ [MPa]	F_u [MPa]
Brace	ASTM 1085	345	460	448
Gusset plates	ASTM A572	345	380	450

4.3 Results and discussion

Normalized load-displacement hysteretic response of the full braces The normalized load-displacement response of specimens 1AL1 to 3BL2 (Table 10) which exclusively feature a free hinge zone are presented in Figure 25. The hysteretic curves is terminated when the PEEQ reaches a value of 1 at the mid-length of the brace. The braces were categorized by their length and weld configuration (Table 10). The normalization of the axial force and displacement helps to eliminates the effect of having different yield resistances between the different brace's sizes and allows for a more meaningful comparison. All specimens exhibit a similar behaviour with a similar response in tension for the first cycles, a visible reduction of the post-buckling loads and a decrease in the global stiffness.

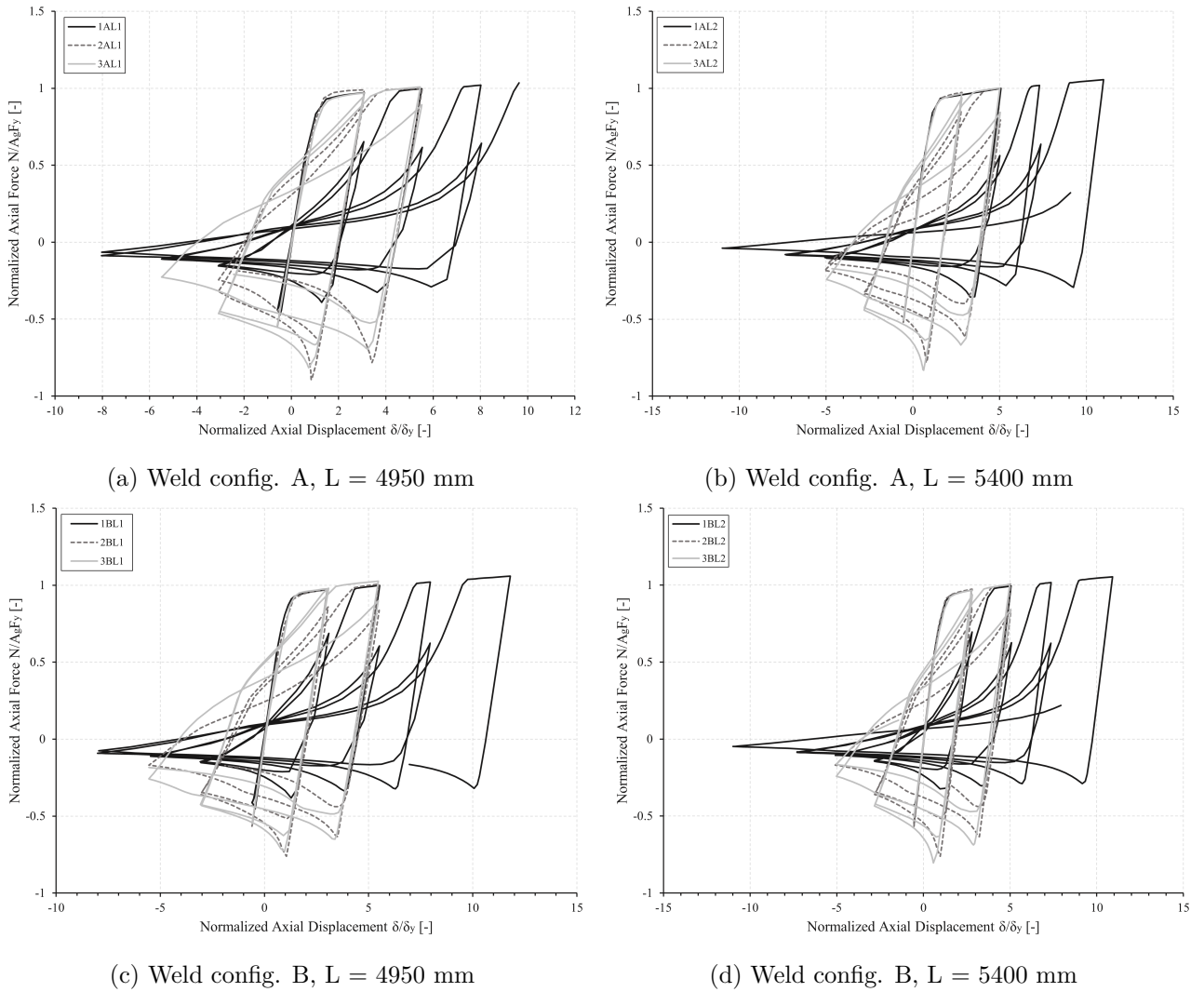


Figure 25: Force-displacement hysteretic response of the braces with a linear clearance zone in the gusset plate

While the width-to-thickness ratios are similar for all HSS sizes (15.1, 15.5, and 15.8, respectively from the smallest to the largest HSS tube), there is a variation in the overall slenderness ratio among these examples. Stockier braces exhibit lower ductility ranges due to their inherent higher stiffness which limits the ability to undergo significant plastic deformation. On the other hand, they can achieve a

higher compressive strength compared to slender braces. In tension, the three HSS sizes demonstrate a similar response in the first loops. However, subsequent loops are wider for stockier braces, indicating a greater capacity to dissipate energy (larger area under the loop) for low displacements. Furthermore, analysing the force-displacement hysteretic curves, it is clear that the buckling load is reached only once, whereas successive post-buckling loads during compression cycles are significantly lower, which is the typical response of a single HSS brace. In contrast, during the tension cycles, the yield limit is reached multiple times. This suggests that the majority of the plastic deformation occurs during the tension cycles.

Figure 25 exclusively illustrates the force-displacement hysteretic behaviour of specimens featuring a linear $2t_g$ hinge zone. It is recognized that the buckled shape of brace is influenced by the ability of the gusset plate to rotate. Hence, the Figure 26 offers a comparison among specimens 1AC, 1BC, 1BE and 1AL1 which exhibits a constrained, elliptical $8t_g$ and linear $2t_g$ hinge zone configuration in the gusset plate. The corresponding hysteretic curves for the HSS 254 254 13 and HSS 305 305 16 can be found in Appendix 7.3.

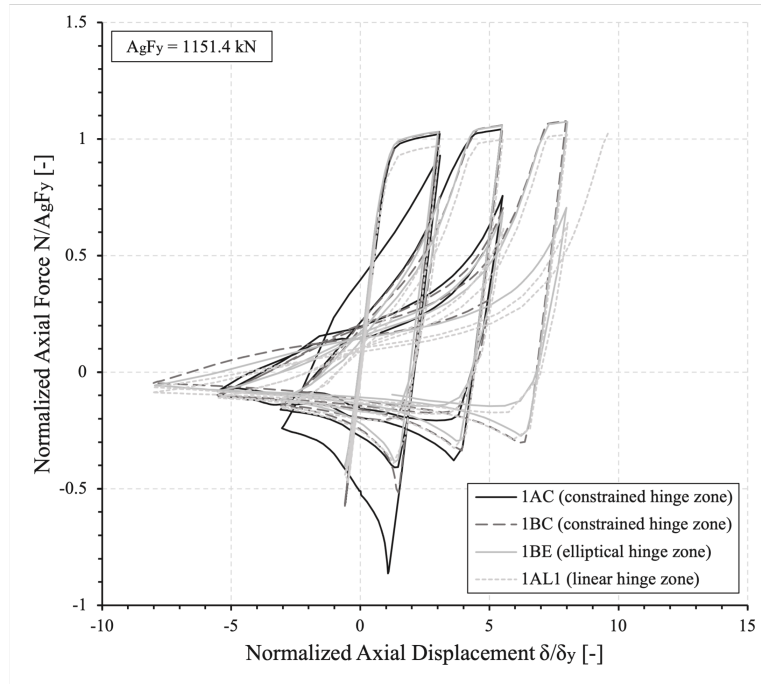


Figure 26: Force-displacement hysteretic curves for HSS 127 127 6.4 with a constrained, elliptical and linear hinge zone

On the tensile loading side, notable differences can be observed among the four numerical models. Specifically, the 1AL1 model with a linear hinge zone exhibits lower axial loads (both in tension and in compression) compared to the other models. For example, its T_{max} is 4.9% lower than that of the 1BC (constrained hinge zone) specimen. Additionally, the 1AL1 model shows a lower stiffness compared to the other models. On the contrary, the 1AC model demonstrates a higher stiffness compared to the 1BC, 1BE and 1AL1 models.

For HSS 254 254 13 and HSS 305 305 16 (Figures 49a, 49b), it can be observed that the 2BC and 3BC models, which also feature a constrained hinge zone, demonstrate a higher stiffness compared to the

other models. These variations can be attributed to a lower axial force transmitted to the brace when a linear offset is integrated in the gusset plate as the 1AL1 shows it. Indeed, the $2t_g$ clearance induces the formation of a plastic hinge, allowing the rotation to occur within the gusset plate rather than at the brace's ends. On the other hand, for the constrained configurations, as rotation is not permitted in the gusset plate, the rotation will tend to occur at the connection, which can resist more due to its higher stiffness compared to the rest of the brace. This aspect is also addressed in the analysis of the stress distributions.

In the compression side, the model 1AC which features a constrained hinge zone combined with a shorter weld, exhibits a significantly higher buckling resistance compared to the 1BC (constrained hinge zone with a longer weld), 1BE (elliptical hinge zone and longer weld) and 1AL1 (linear hinge zone with weld configuration A) models. In order to understand this variability, Figure 27 illustrates the lateral displacement distribution of the 1AC, 1BC and 1AL1 numerical models at the first buckling load. Notably, the buckling resistance increases ($N/A_g F_y = -0.86, -0.52, -0.39$ respectively for 1AC, 1BC and 1AL1) as the out-of-plane displacement at mid-length of the brace decreases ($U_x = -3.8$ mm, -48.5 mm, -99.7 mm respectively for 1AC, 1BC and 1AL1). This observation can be attributed to the rotation of the brace's ends which is influenced by the level of confinement provided by the gusset plate and the length of the weld. Specifically, a larger lateral displacement at mid-length of the brace results in a greater rotation of the brace's ends, thus reducing the force required to achieve that rotation. Despite the hinge zone being constrained in both cases, model 1BC, with its longer weld, enables a more gradual rotation of the brace's ends compared to the more restricted configuration of 1AC thanks to a more uniform stress distribution.

The force-displacement hysteretic response of the HSS 254 254 13 and HSS 305 305 16 (Appendix 7.3) exhibit a similar behavior, showing less variability in buckling resistances across the constrained, elliptical, and linear configurations. It is also important to note that among all numerical models, only the 1AC model which is the slenderest brace with a constrained gusset plate configuration exceeds the probable buckling compressive resistance C_u equal to 647 kN by 35%.

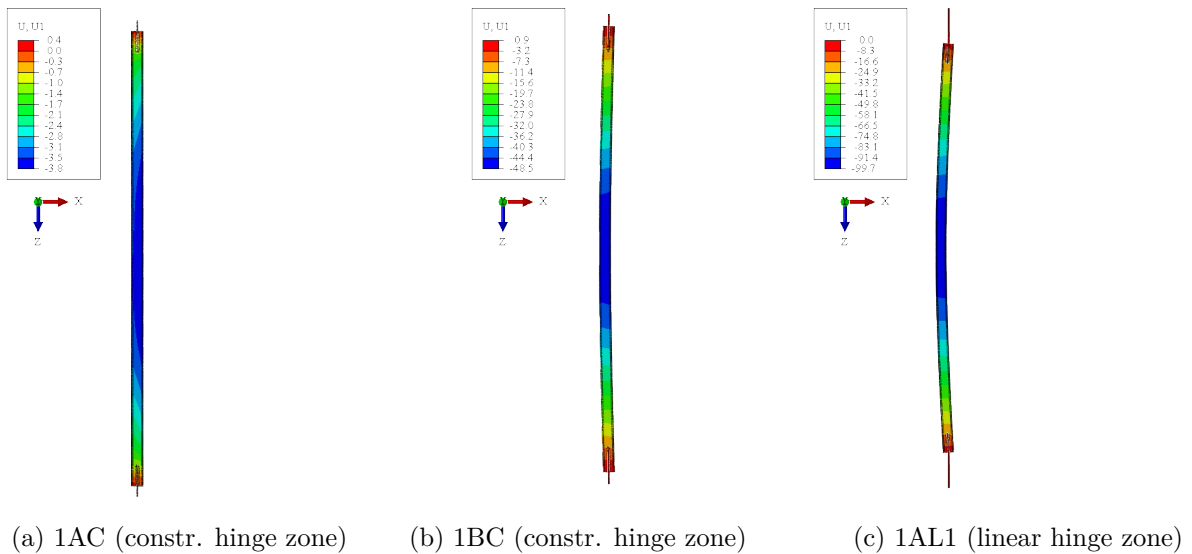


Figure 27: Lateral displacement distribution U_x for HSS 127 127 6.4 with different gusset plate configurations

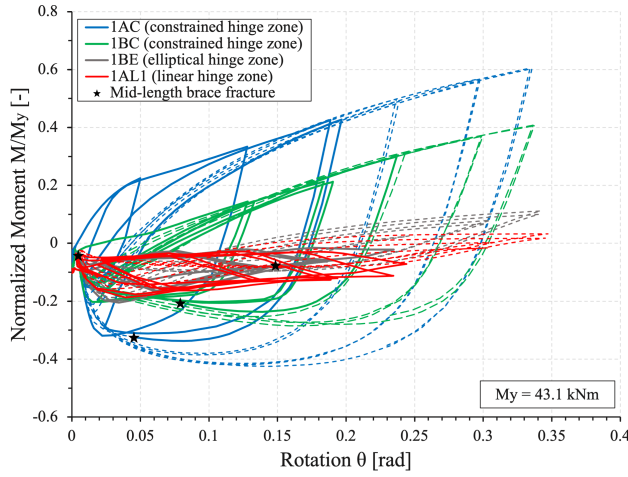
Moment vs. Rotation The purpose of constraining the gusset plate is to eliminate the presence of the hinge zone within the plate, thus directing the moment experienced during compression loading towards the HSS tube's end. Figure 28 illustrates the variation of the normalized moment (with the yield moment resistance computed with F_y) within the HSS measured at the end of the slot (critical zone), as a function of the rotation of the brace's ends. In order to obtain a comprehensive understanding of the behaviour, it was determined that plotting all the response points, including those beyond the potential fracture point defined by a PEEQ value equal to unity in the middle of the brace, would be beneficial (expressed by the dashed lines).

The rotation of the brace's ends has been defined according to a geometrical approach based on a simplified geometry of a buckled brace following Equation 29 where U_x is the lateral displacement at mid-length of the brace. Although it is acknowledged that this equation oversimplifies the actual rotation of the brace's ends, the conclusions drawn from the equation are thought to be conservative.

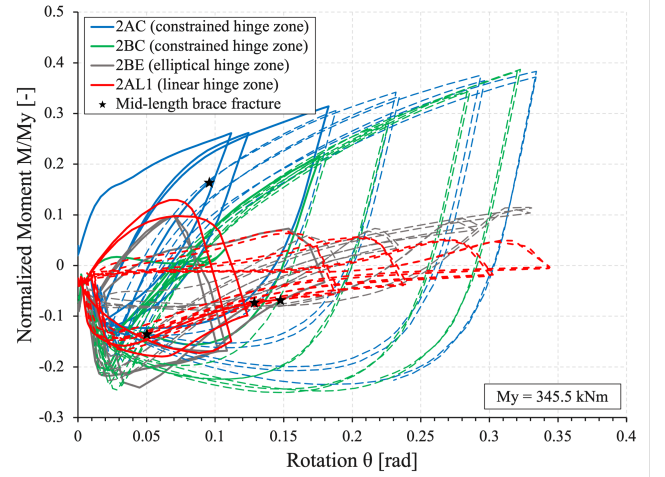
$$\theta = \arcsin\left(\frac{2 \cdot U_x}{L_{brace}}\right) \quad (29)$$

A non-symmetrical response was observed in all specimens under both tensile and compressive cycles. This behaviour can be attributed to the variation in axial load, which decreases during compression leading to a moment recovery and increases during tension resulting in a moment deterioration. Across all three scenarios, a notable trend emerges : the greatest moment occurs when the gusset is constrained with the weld configuration A, while the smallest moment arises when the gusset is allowed to rotate freely thanks to the elliptical offset. Additionally, as the tube sizes increase, the behaviour of the the two constrained gusset configurations, despite having different weld setups, tends to converge particularly for small rotations. Indeed, a short-length larger-size weld will lead to a increased gusset plate's thickness according to Equations 14 to 17. This increased thickness results in a larger moment of inertia compared to a thinner gusset, consequently leading to larger moments for the weld configuration A. Importantly, in all cases, the moment-to-elastic moment resistance ratio never reaches unity. This observation suggests that even for a short-length larger-size weld, the HSS brace does not experience plastic deformation due to compression loading at that particular location.

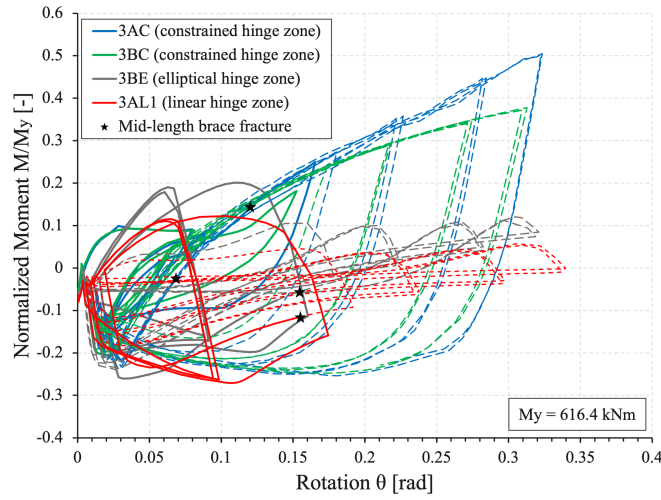
Furthermore, it is worth noting that the moment-rotation responses of the specimens type xAC and xBC (constrained hinge zone with respectively a weld configuration A and B) exhibit a consistent almond-shaped pattern in their responses, while the response's shape of the configurations with an elliptical and linear offset evolves as the size of the HSS increases. Figure 28c illustrates cycles of significant moment for small rotations with these wave-shaped cycle amplitudes decreasing as the rotation increases. This phenomenon can be attributed to the development of a plastic hinge within the gusset plate, enabling the moment to be transmitted beyond the brace. As a result, the HSS tube at the connection is relieved of excessive demand and experiences reduced stresses.



(a) HSS 127 127 6.4



(b) HSS 254 254 13



(c) HSS 305 305 16

Figure 28: Moment Vs. Rotation at the SHG connection near the HSS brace's slot

Equivalent Plastic Strain (PEEQ) vs. Drift The equivalent plastic strain (PEEQ) is a scalar parameter that ranges from zero to one and serves as an indicator of the material's inelastic deformation accumulation. If the PEEQ is greater than zero, it signifies that the material has yielded according to the Abaqus Documentation (Simulia, 2012). The results of the moment-rotation graphs at the brace's ends revealed that the combination of a short weld and a constrained hinge zone results in the highest moments. As a consequence, Figure 30 displays the PEEQ distribution along the brace of the three models exhibiting the highest moments (1AC, 2AC and 3AC) when reaching the buckling resistance (OB) and at T_{max} . This figure highlights two critical locations at the SHG connection : one near the end of the HSS slot at the front of the weld and the other at the extreme fiber of the HSS (at the corner) as in the 1AC model (Figure 30b). As observed in the previous analyses, the xAC type models are the most critical, therefore, the following analysis is conducted on all other configurations at the location depicted in Figure 29. The relationship between the PEEQ and drifts at the extreme fiber of specimen 1AC is also studied.

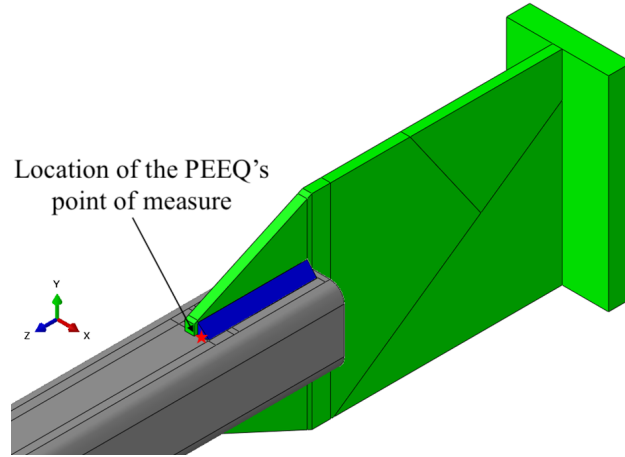
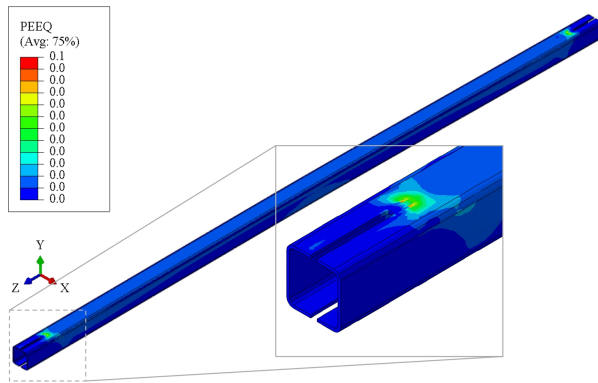
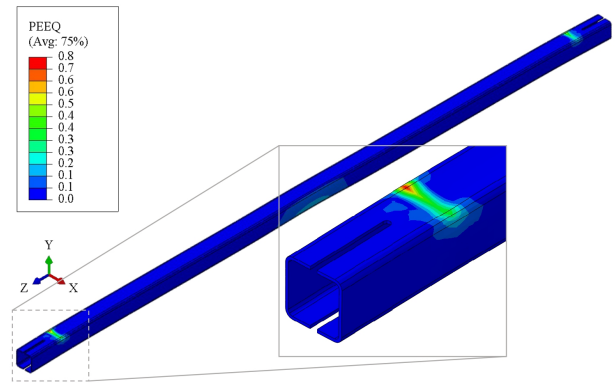
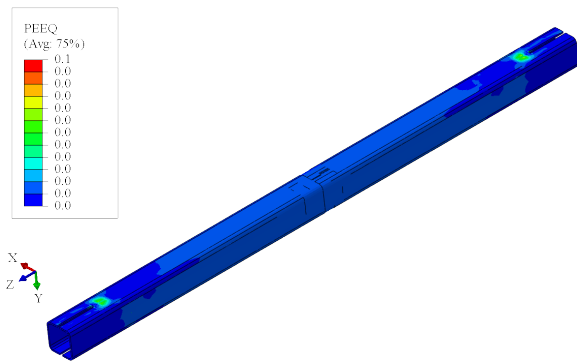


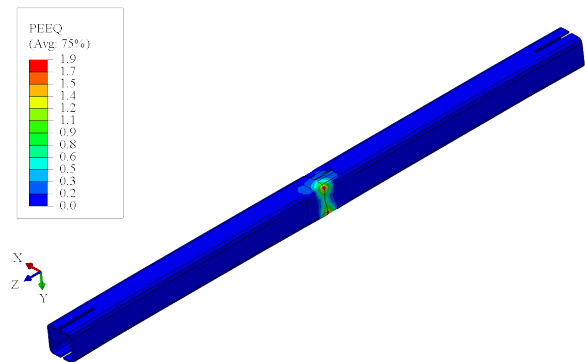
Figure 29: Critical location on the HSS at the connection



(a) 1AC at OB

(b) 1AC at T_{max} 

(c) 2AC at OB

(d) 2AC at T_{max}

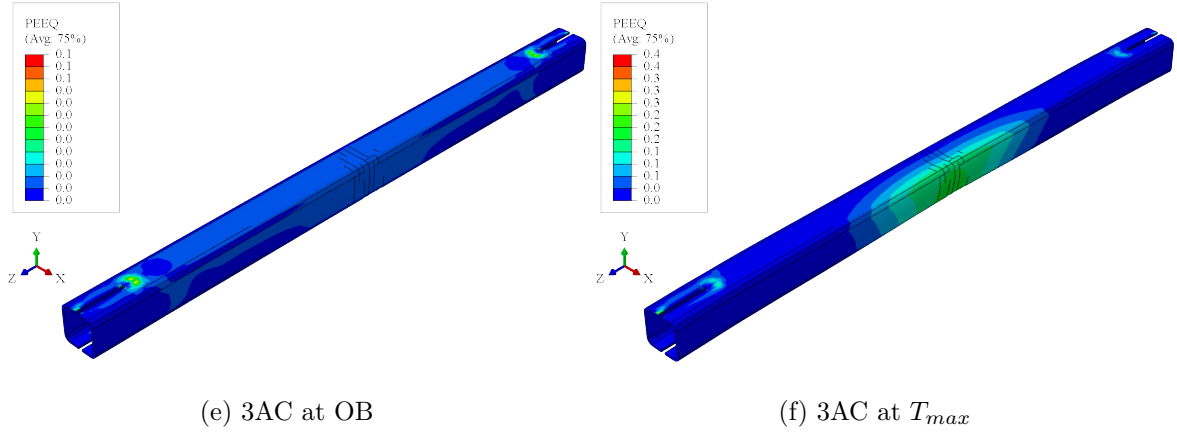


Figure 30: PEEQ distributions of 1AC, 2AC and 3AC models (constrained hinge zone with weld configuration A, respectively for HSS 127 127 6.4, HSS 254 254 13 and HSS 305 305 16) at the buckling resistance and T_{max}

Figure 31 depicts the relationship between the PEEQ values measured on the HSS tube at the end of the welds as referred on Figure 29 as a function of the drift. Each graph represents a specific tube size with different weld configurations and brace's lengths with a linear clearance in the gusset plate. The fracture occurring at the mid-length of the brace (identified by a PEEQ value equal to one) is denoted by a star icon, resulting from low-cycle fatigue. All three HSS sizes exhibit a similar response. Notably, as the tube size increases, the curves become less scattered, suggesting that the weld configurations have a lesser impact on larger tubes. One possible explanation for this phenomenon could be that the compactness of the connection relative to the slenderness of the brace is less significant for a stockier brace. Figures 31a and 31b show that the length of the brace primarily influences the drift at which the brace experience fracture (with a PEEQ value equal to unity). A longer brace with a higher overall slenderness displays a wider range of ductility as illustrated in Figure 25. Similarly, as the tube becomes stockier, the differences at the fracture become less pronounced between the several connections configurations. Moreover, a stockier brace leads to lower drifts when reaching fracture at mid-length of the brace. As an example, specimens 1BL2, 2BL2 and 3BL2 experience fracture at 4.08 %, 2.21 % and 2.19 % respectively for HSS 127 127 6.4, HSS 254 254 13 and HSS 305 305 16.

To delve into further detail, the weld configuration B (longer-length smaller-sized weld) combined with a short brace exhibits higher PEEQ values compared to the other models. On the contrary, the weld configuration A (shorter-length larger-size weld) paired with a longer brace results in lower PEEQ values. This behaviour can be explained by an increased ductility thanks to a longer brace i.e a higher overall slenderness which leads to a higher capacity to undergo plastic deformation. The plastic deformation values, even at drift levels approaching 5%, are relatively small compared to the fracture threshold defined at the mid-length of the brace. For example, the 3BL1 model exhibits the highest PEEQ when the brace fractures, which is 0.11, significantly below the threshold of 1. This is likely because the majority of deformation occurs at the mid-length of the brace, where the PEEQ values are higher for the same drift levels. This leads to the conclusion that the fracture at the connection location is unlikely to happen prior to the fracture at the mid-length of the brace, which is the intended and dominant failure mode according to capacity design requirements.

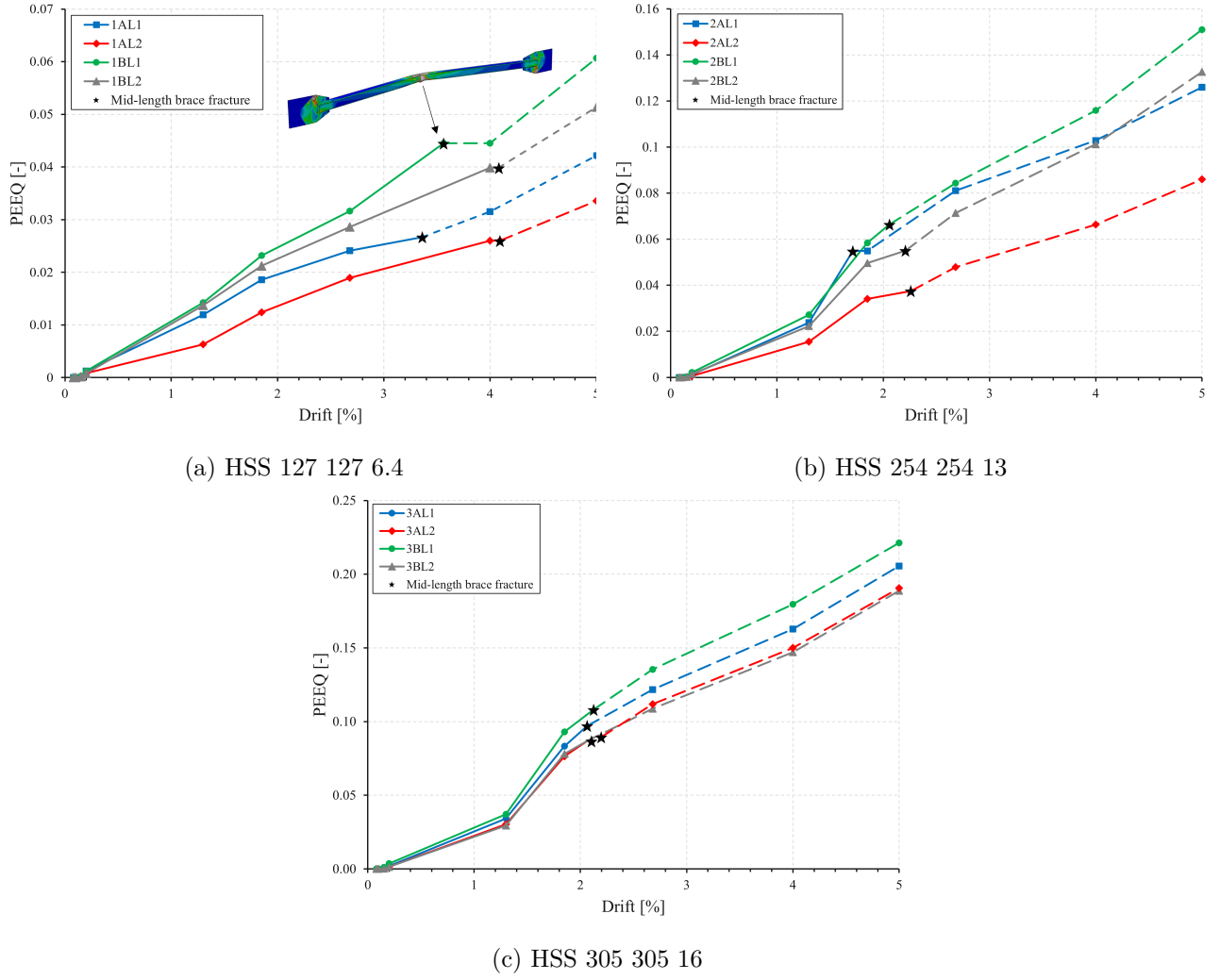


Figure 31: PEEQ vs. Drift measured on the HSS at the end of the welds with a linear clearance in the gusset plate

Figure 32 presents the relationship between the equivalent plastic strain, measured on the HSS at the end of the welds as shown on Figure 29 and the drift for the three tube sizes. The graphs include both constrained and elliptical clearance in the gusset plate, considering both weld configurations. Similarly to Figure 31a, a star icon indicates fracture at the mid-length of the brace. In order to assess the influence on the PEEQ of the different degrees of confinement of the gusset plates, the graphs were extended to include configurations with a linear offset in the hinge zone as illustrated in Figure 31. Due to the consistent brace length of 4950 mm among the specimens with constrained and elliptical hinge zone, the decision was made to exclusively incorporate the xxL1 type numerical models.

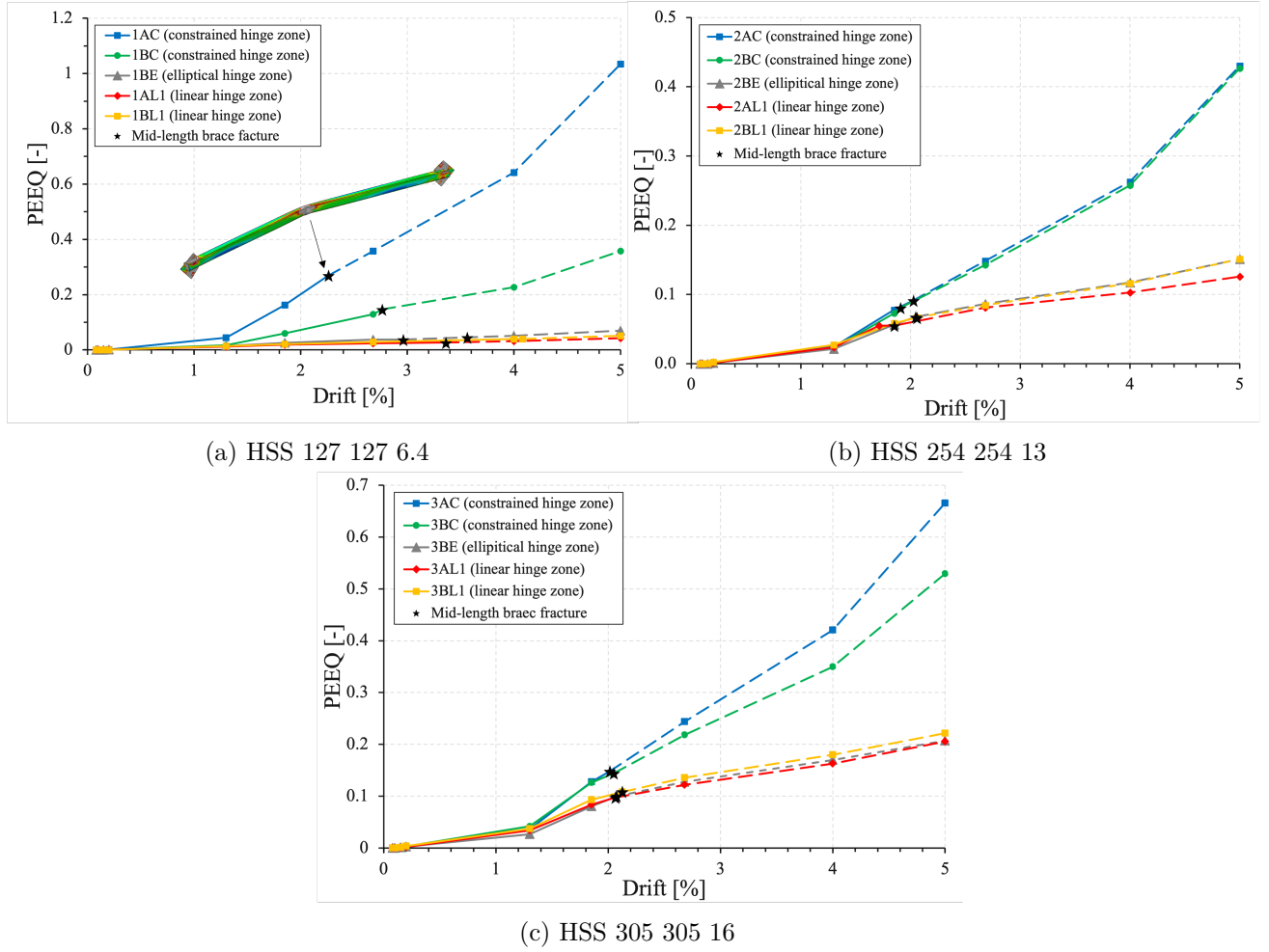


Figure 32: PEEQ vs. Drift measured on the HSS at the end of the welds with a constrained and elliptical offset in the gusset plate

As anticipated, the connection configuration with an elliptical clearance exhibits lower PEEQ values compared to a constrained configuration, with a maximum value reached at fracture of the brace's mid-length equal to 0.1 for specimen 3BE among all studied models of Figure 32. By incorporating either an elliptical or linear offset, a hinge zone is created, facilitating the rotation of the plate and consequently reducing the plastic deformation in the HSS at the front of the welds. On the other hand, a constrained configuration with a compact weld (type xAC) consistently results in the highest PEEQ values among the same HSS size. However, even though it reaches higher values, it is evident that fracture at mid-length of the brace due to low-cycle fatigue is the primary failure and occurs before the PEEQ equal to unity at the connection location (Figure 29) is reached, as demonstrated in Figure 32a.

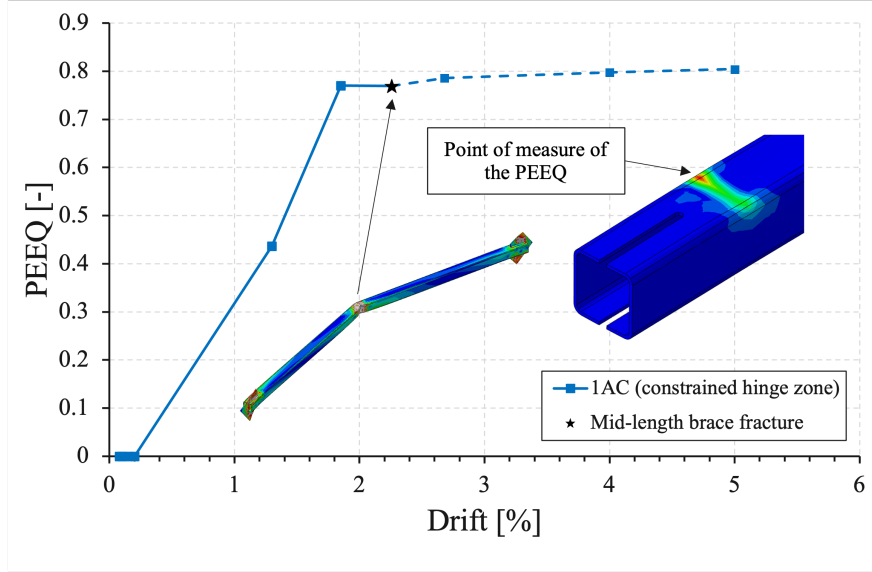


Figure 33: PEEQ vs. Drift measured on the HSS corner at the end of the welds for 1AC model (constrained hinge zone)

Under compressive loading, both the connection and the brace's undergo rotation, resulting in the highest stress values concentrated in the extreme fibers of the section, away from its neutral axis. This behavior is particularly evident in the configuration featuring a restricted hinge zone with a weld configuration A (1AC model), where there is a notable concentration of PEEQ representing the accumulation of plastic deformation at the corners of the HSS, as illustrated in Figure 30b. As mentioned in the analysis of the force-displacement hysteretic response, the majority of the plastic deformation occurs during the tension cycles, resulting in a PEEQ concentration at the HSS corners at T_{max} . The relationship between the PEEQ and drifts measured at this specific location is presented in Figure 33. Notably, fracture at mid-length of the brace occurs at a drift of 2.26% corresponding to a PEEQ value of 0.77. Despite the model 1AC being the most critical among all the specimens in terms of PEEQ, fracture at mid-length of the brace occurs prior to reaching the fracture at the extreme fiber of the cross-section at the connection (before the PEEQ reaches unity).

Stress distributions Stress distribution analyses provide valuable insights. The analyses of the PEEQ-drift and moment-rotation relationships revealed that SHG connection configurations combining a constrained hinge zone with a weld configuration A (type xAC) experience the highest moment demands on the HSS at the connection and exhibit the highest PEEQ values in critical zones compared to the other models. Therefore, it is interesting to study the Von Mises stress distribution of these xAC type models and compare them to those with lower moments and PEEQ values.

Figure 34 illustrates the distribution of the Von Mises stresses for models 1AC (constrained hinge zone), 1BE (elliptical hinge zone), and 1AL1 (linear hinge zone) for the entire brace, as well as an amplified view of the brace's end when their respective buckling resistance is reached. The stress distribution scale is chosen such that the upper limit is given by $R_y F_y = 460$ MPa. Any stresses beyond this limit are shown in gray, indicating that the material has yielded. The equivalent graphs for the HSS 254 254 13 and HSS 305 305 16 braces are showcased in Figures 35 and 36.

In general, a similar behavior is observed among the three HSS tube's sizes. A distribution with higher stresses, particularly with stress concentrations at certain locations on the brace, is observed for a confined hinge zone configuration (type xAC), while a more uniform stress distribution with lower values is observed for a connection configuration with an elliptical offset (type xBE). Upon analyzing the 1AC, 2AC, and 3AC models, it becomes apparent that a stress concentration occurs at the front of the weld near the end of the HSS tube's slot. At the same level, the color scheme indicates material yielding at the HSS corners. This occurs due to the combination of a short weld and a constrained hinge zone (type xAC), which forces the rotation to take place in the HSS brace at the slot instead of occurring in a dedicated gusset plate's hinge zone, resulting in higher stresses at that location. On the contrary, a longer weld and an elliptical offset in the gusset plate configuration (type xBE) allows a more gradual rotation of the brace's ends and the connection, thus leading to better distribution along the HSS and significantly lower stresses compared to the $R_y F_y$ value, as depicted in Figures 34b, 35b and 36b. Nevertheless, it is important to note that a concentration of high stresses still persists at the front of the welds, which can be attributed to a discontinuity between the welds and HSS tube's material properties and geometries.

In the case of a hinge zone that allows a free rotation (linear hinge zone) of the gusset plate (type xAL1), the stress distribution along the braces closely follows the compression-induced deformation of the brace, with higher stresses concentrated on the compressed extreme fiber at mid-length of the brace (Figures 34a, 35a, 36a). For stockier braces (2AL1 and 3AL1), the stresses also concentrate at the brace's ends at the start of the welds close to the hinge zone (Figures 35a and 36a). This is likely due to the increased stiffness of the brace's ends compared to the gusset plate, hence attracting the stresses at that location.

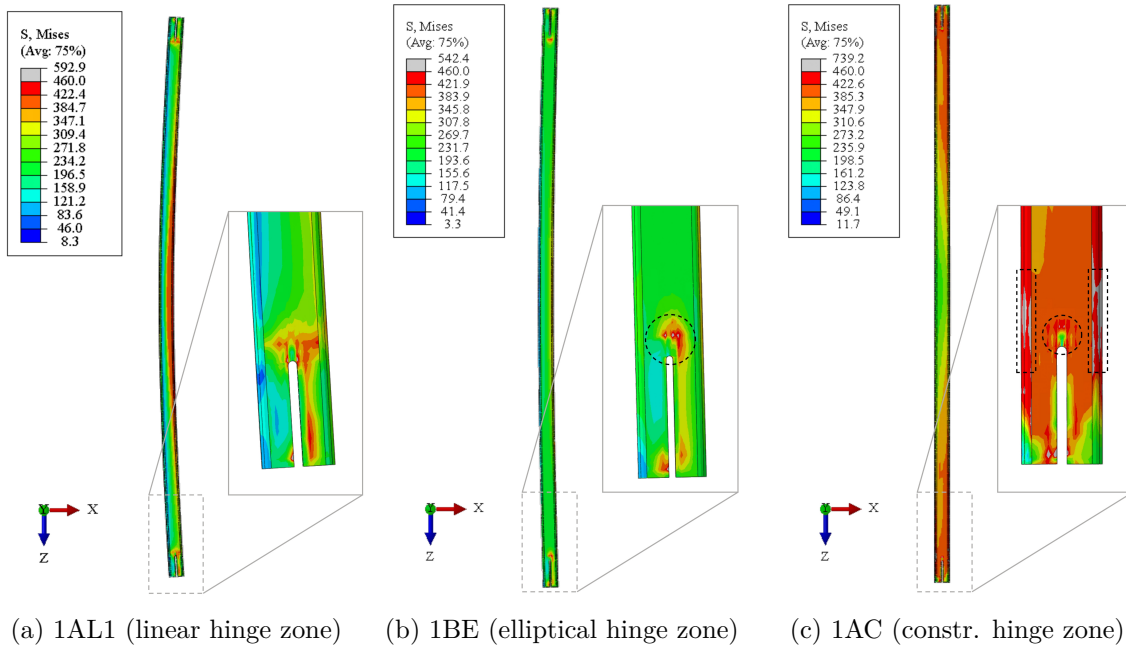


Figure 34: Von Mises stress distributions for 1AL1, 1BE, 1AC models at their respective buckling resistance

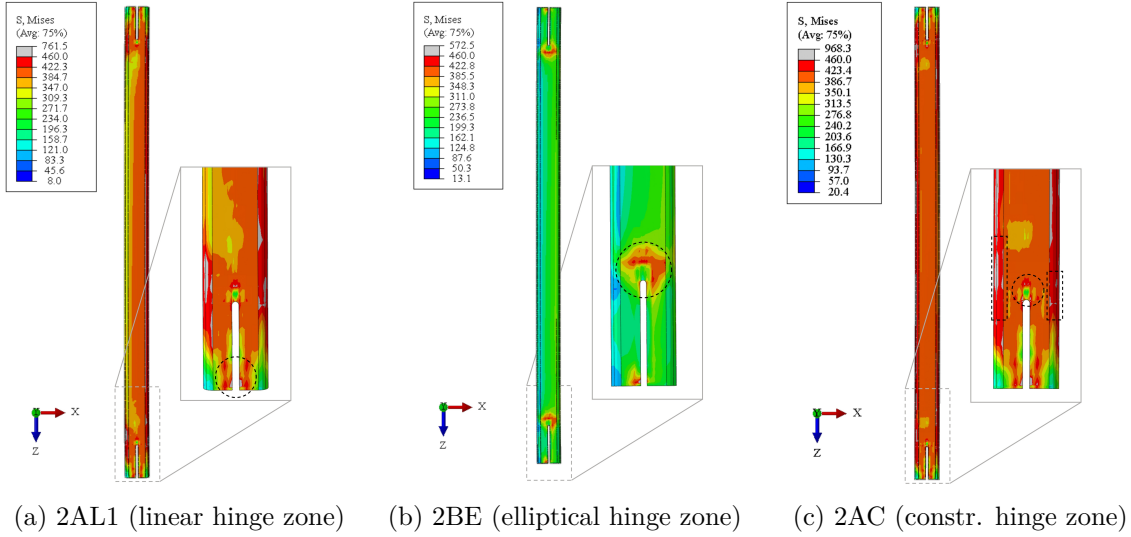


Figure 35: Von Mises stress distributions for 2AL1, 2BE, 2AC models at their respective buckling resistance

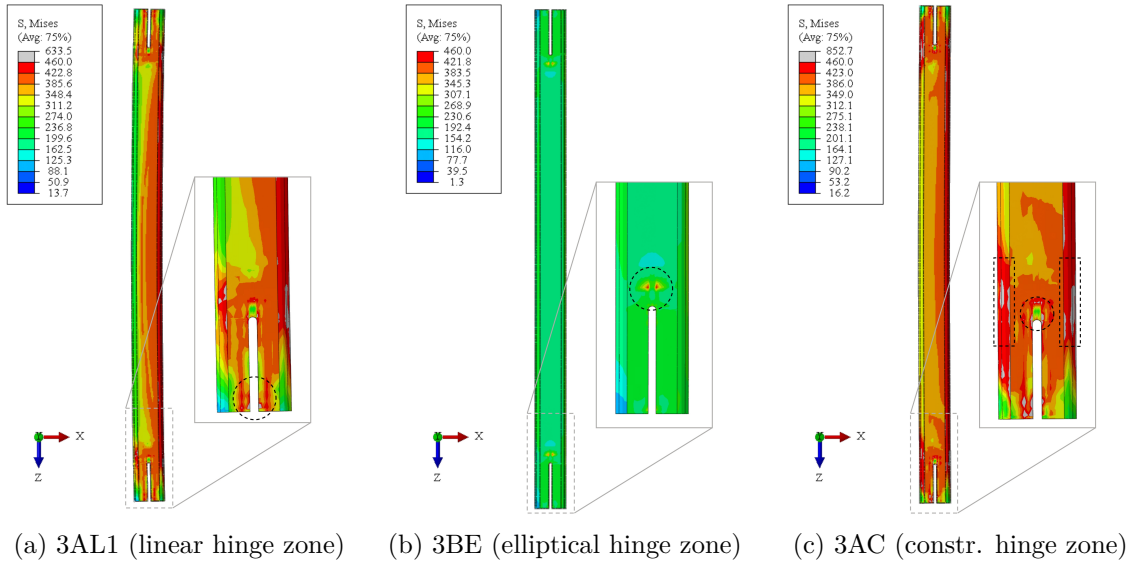


Figure 36: Von Mises stress distributions for 3AL1, 3BE, 3AC models at their respective buckling resistance

Figure 37 depicts the hysteretic curve for the 1AL1 specimen, along with the stress distribution at critical points such as the buckling load and T_{max} . The upper limit of the stress distribution interval is 460 MPa, corresponding to the $R_y F_y$ value of the HSS. The equivalent figures for the 1AC and 1BE models as well as Table 14 that summarizes the loads, drifts and cycles at which the buckling resistance and T_{max} occur can be found in Appendix 7.4. The stress distribution at T_{max} provides an additional support for the previous reasoning regarding the stress distribution at the buckling resistance. A linear clearance allows for a hinge zone to develop within the gusset plate, preventing the concentration of moments in the HSS at the connection. As a result, the brace can flex along its entire length. After multiple compression cycles, another plastic hinge will develop at the mid-length of the brace, which explains the yielding observed in the stress distribution at T_{max} in Figure 37.

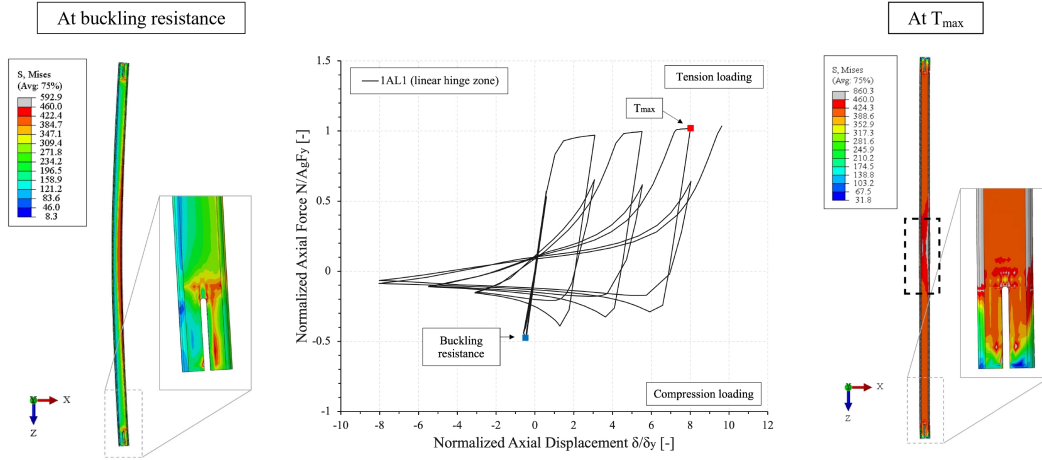


Figure 37: Von Mises stress distributions of the 1AL1 model (constrained hinge zone) at the buckling resistance and T_{max}

Figure 38 displays the Von Mises stress distribution for the three gusset plate configurations for the largest tube size (HSS 305 305 16) at the point of reaching their respective buckling load. Notably, Figures 38a and 38b presents a constrained hinge zone respectively for a weld configuration A and B. The shorter-length larger-size weld (weld configuration A) demonstrates a pronounced stress concentration on the gusset plate near the start of the HSS tube's slot, whereas a longer-length smaller-sized weld (weld configuration B) reveals a more uniform stress distribution at the tube's ends. As anticipated, higher stresses are localized within the elliptical hinge zone in the gusset plate for the specimen 3BE, relieving the stresses at brace's ends.

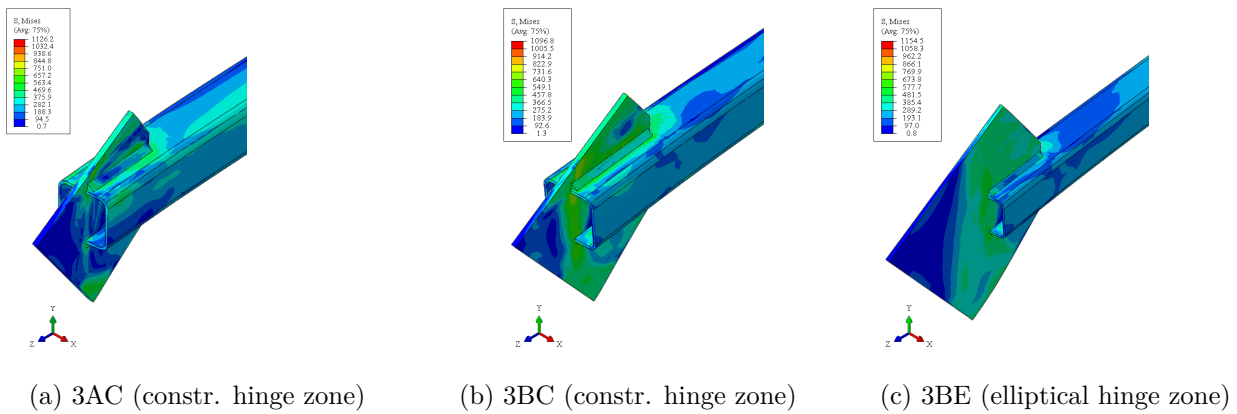


Figure 38: Von Mises stress distribution for constrained and elliptical configuration for HSS 305 305 16 at the buckling load

4.4 Summary

In summary, the results of the hysteretic load-displacement graphs demonstrate that slender braces (HSS 127 127 6.4) exhibit higher ductility ranges but a lower compressive strength compared to stockier braces (HSS 254 254 13 and HSS 365 365 16). The response curves indicate that the yield resistance is reached multiple times suggesting that the plastic strain accumulate during tension cycles. Among all specimens, the constrained hinge zone combined with a short weld configuration (type xAC) exhibits the highest buckling resistance for HSS 127 127 6.4, HSS 254 254 13 and HSS 305 305 16 compared to elliptical or linear configurations, with the buckling resistance of the 1AC model exceeding the probable buckling compressive resistance C_u by 35%. Furthermore, regarding the degree of confinement of the gusset plate, a linear hinge zone leads to lower axial forces and stiffness compared to an elliptical and confined hinge zones. This suggests that achieving a more uniform buckled deformation along the brace requires a lower axial force when using a free hinge zone.

The moment-rotation measured on the HSS at the connection show a non-symmetrical response between tension and compression cycles. The constrained configuration with a short weld (xAC type) exhibits the highest moments among the same HSS size for different degrees of confinement. Additionally, as the tube size increases, the behavior of the two constrained gusset configurations (type xAC and xBC), despite having different weld setups, tends to converge, particularly for small rotations. This suggests that the impact of weld configurations on larger tubes is relatively minimal. Specimens with permitted hinge zones (linear and elliptical clearance) exhibit a different behavior (in a wave-shape instead of almond-shape) compared to constrained configurations with lower moments, suggesting that a constrained hinge zone in the gusset plate forces the moment to occur in the HSS instead of the gusset plate. Moreover, Von Mises stress distributions reveal that an elliptical hinge zone combined with a longer weld induces reduced stresses and a more uniform distribution along the brace's length compared to other configurations, even at critical loads such as the buckling resistance or T_{max} .

Most importantly, the relationships between the equivalent plastic strains and drifts have highlighted critical connection locations where plastic deformation concentrates, either near the end of HSS tube's slot at the front of the weld or at the corner of the HSS at its extreme fiber. The PEEQ-drift analysis is conducted at these locations and it resulted failure at the mid-length of the brace takes place before fracture occurs at the connection which follows the capacity design principles. The combinations that result in the lowest PEEQ values are the linear and elliptical hinge zone configurations, making them preferable for practical use. However, constrained configurations can also be utilized, as they are also capacity design protected, even though they may result in higher levels of plastic strains.

5 Feasibility study of the SHG connection construction

Relying on the findings of previous research and this report, which have demonstrated the successful performance of the SHG connection subjected to a monotonic tensile and reversed cyclic loading conditions, the aim is to identify an effective way to incorporate this connection into steel structures. This involves a comprehensive understanding of the construction and implementation processes of the SHG connection, whether directly on construction sites or in fabrication plants, with a focus on optimizing material quantity, construction time, design, and cost.

Fillet welds employed in the SHG connection offer distinct advantages, providing both structural rigidity and visual appeal. However, it is important to note that welding requires qualified technicians to ensure proper execution and quality controls, resulting in higher potential cost implications. Furthermore, due to the environmental sensitivity and associated risks such as high temperatures and emanating fumes, it is advisable to minimize welding activities on construction sites. Hence, Afifi et al. (2022) studied four bolted connections scenarios through numerical simulations involving 2-plates, 4-angles, splice plate and T-stub connections associated to the SHG connections as depicted in Figure 39. The SHG connection would be constructed in factory, transported and bolted on construction site. Those connections are found in common practice in the USA and Canada. Despite the distinct load transfer mechanisms employed by the various paddle-gusset plate connections, the overall performance of the SHG connection remained remarkably consistent. The different configurations had minimal impact on its effectiveness. However, one notable exception was the 4-angle configuration, which demonstrated a significant reduction in in-plane gusset rotation. This improvement can be attributed to the wider gusset plate at the connection. Although the construction technique involves the simplicity of fabrication in factory of the HSS SHG connection and on-site bolting, it requires additional costs, design, materials and quality controls.

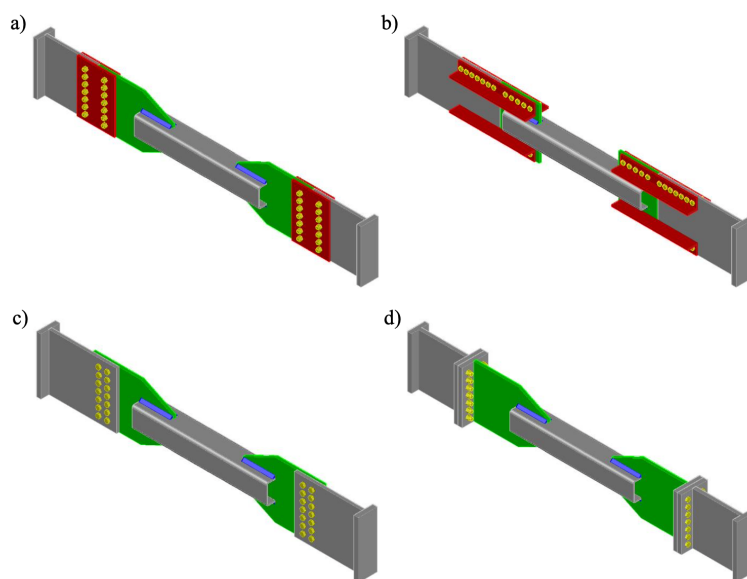


Figure 39: Paddle-to-gusset plates connections : a) 2-plates b) 4-angles c) Splice plate d) T-stub (Figure courtesy of Afifi (2021))

Achieving the optimal equilibrium between prefabrication in a controlled factory environment and the transportation of components to the construction site, while also considering the feasibility of direct on-site construction, emerges as an important consideration. This section aims to investigate conceptually the geometric feasibility of various constructability scenarios for HSS SHG connections to beam-to-column joints of CBFs. These scenarios encompass an examination of standalone SHG connections as well as their combination with additional bolted and/or welded connections.

5.1 Constructability of the SHG connection on-site

The implementation of the conventional connection on construction sites assumes that the gusset plates are pre-welded to the frame, and the HSS tube is intentionally over-slotted to facilitate its insertion between the gusset plates. Once accurately aligned along the diagonal axis of the frame's bay, the brace is securely joined to the gusset plate through the application of fillet welds. When it comes to the SHG connection, the conventional approach of overslotting the HSS tube becomes impractical as the fillet welds between the gusset plate flaps and the HSS tube start on the gross area of the bracing member beyond the HSS tube's slot. Therefore, alternative approaches need to be considered to try to insert the bracing member between the gusset plates by back-and-forth movements. One could explore the idea of overslotting the gusset plate instead, taking the opposite perspective.

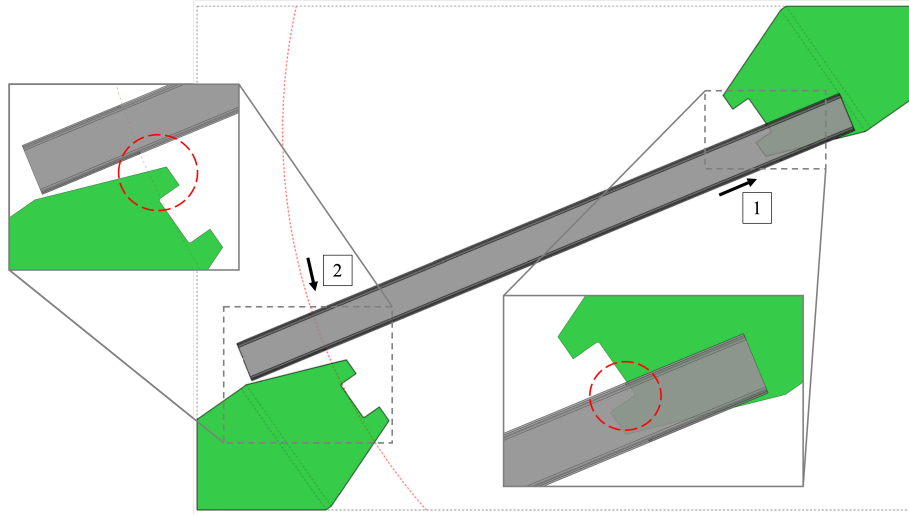


Figure 40: Implementation of the 3BL1 model ($L_{wg}/L_w = 15\%$)

To illustrate the implementation of the SHG connection on a construction site, the geometry of the 3BL1 model from the parametric study is utilized, and the values of its geometry are provided in Table 10. This model is chosen because it includes a longer weld, resulting in a wider gusset plate's geometry and longer slots in both the HSS and the plate. Figure 40 depicts the initial two steps required for its installation. Firstly, assuming that the gusset plates are already welded to the steel frame, represented by the gray dashed lines outlining the column and beam flanges, the brace would be positioned within the frame plane. The step 1 indicates that one of the gusset plate's flap would be inserted between the two slots of one of the brace's end and that it would be pushed as far as possible in the direction of the top gusset plate to facilitate step 2. The concept of implementation of the SHG connection involves back-and-forth movements of the brace between the gusset plates. Therefore, in step 2, the

other end of the brace is rotated to fit between the flaps of the lower gusset plate. The dashed red line represents the radius between the center of rotation at the HSS tube's upper end and the HSS slot's lower end. However, in the case of the 3LB1 numerical model with a 15% overlap length ratio, it is observed that the final step may be impractical due to insufficient length of the HSS tube's slot at the lower end or the flaps of the gusset plate being too long to accommodate the HSS onto the gusset plate. Consequently, in the case of this specific 3BL1 model configuration, it is not feasible to implement the SHG connection on-site due to inherent geometric limitations. However, in Section 5.2, several conceptual ideas are presented to address these geometric challenges and facilitate the on-site construction of the SHG connection without requiring additional welded or bolted connections. The following figures are drawn to scale.

5.2 Conceptual solution ideas

5.2.1 Solution 1 - Reduction of the overlap length ratio

As shown in Figure 40, the issue can stem from multiple sources: either an excessively long gusset plate's flap length, an insufficient length of the HSS tube's slot, or a combination of both. In such cases, the first solution involves reducing the flap length by decreasing the overlap length ratio. A shorter weld configuration is also chosen and an example is demonstrated in Figure 41, which showcases the geometry of the 3AL1 specimen from the parametric study presented in Section 4 with an overlap length ratio of 5%. Other dimensions of the connection were updated according to the design methodology proposed by Afifi et al. (2023) while keeping the same weld size and length. Afifi et al. (2021) conducted a parametric study exploring various conclusive overlap length ratios, ranging from 5% to 30%. Therefore, considering the results, the minimum overlap length ratio of 5% is selected. Similarly to the construction depicted in Figure 40, one of the flap of the upper gusset plate is inserted between the two slots of the HSS tube's end (step 1), an attempt is made to rotate the other end in order to fit it between the two flaps of the opposite gusset plate and accommodate the brace (step 2). Although the overlap length is reduced, it still does not allow the tube to fit between the flaps of the lower gusset plate (step 2).

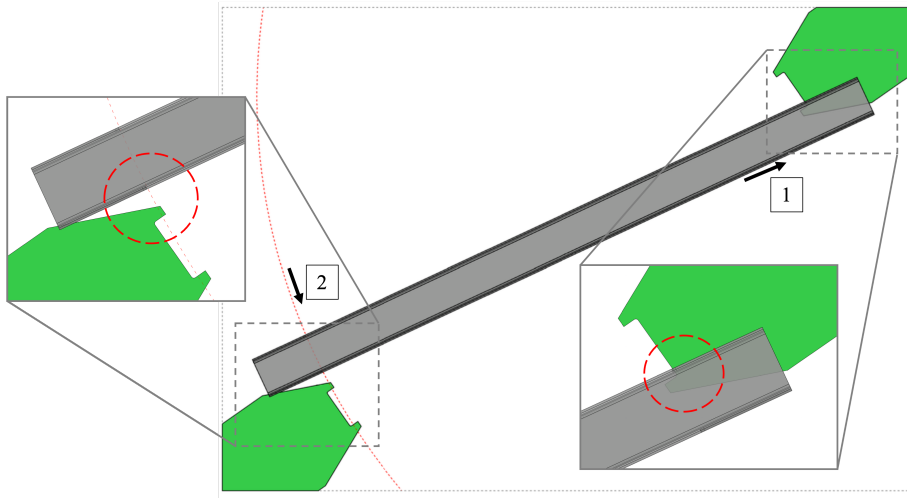


Figure 41: Implementation of the 3AL1 model ($L_{wg}/L_w = 5\%$)

5.2.2 Solution 2 - Modification of the gusset plate's notch geometry

As seen in the previous solution, it would be beneficial to have more room at step 1 of Figure 41, specifically in the notch of the gusset plate, to push the upper brace's end a bit further and allow the opposite end of the HSS tube to pass and fit between the two flaps of the bottom gusset plate. Therefore, the second solution involves the extension of the gusset plate's notch in a triangular shape (Figure 45). Figure 42 illustrates the three necessary steps for assembling the SHG connection on-site. This solution still features the 3AL1 model with an overlap length ratio of 5%. Step 1 remains the same as previously presented, where one flap of the upper gusset plate is inserted between the slots on one HSS tube's top end. The modified notch in the gusset plate allows the tube to be pushed slightly further as shown in step 1 of Figure 42. In the same figure, the red dashed line represents the arc, which has a radius equal to the distance between the center of rotation at the HSS tube's top end and the HSS slot's bottom end. Step 2 of Figure 42 involves placing the bottom end of the tube between the two flaps of the bottom gusset plate. Then, the tube is pushed as far as possible against the bottom gusset plate at step 3 to rotate the top end and to position it between the flaps of the top gusset plate (step 4). Unfortunately, in this case, it is observed that the upper HSS tube's slots are insufficiently long to allow the flap of the gusset plate to pass through.

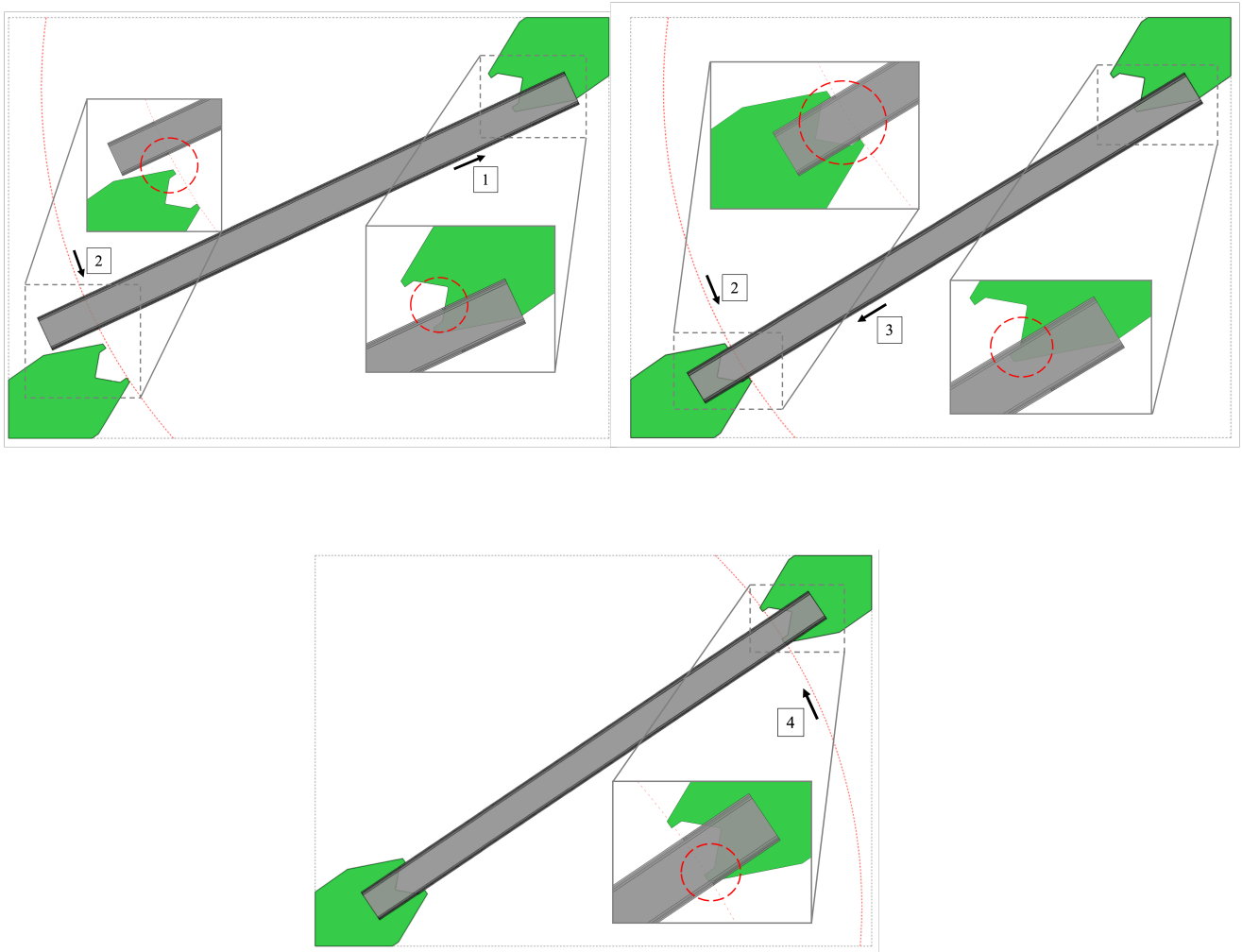


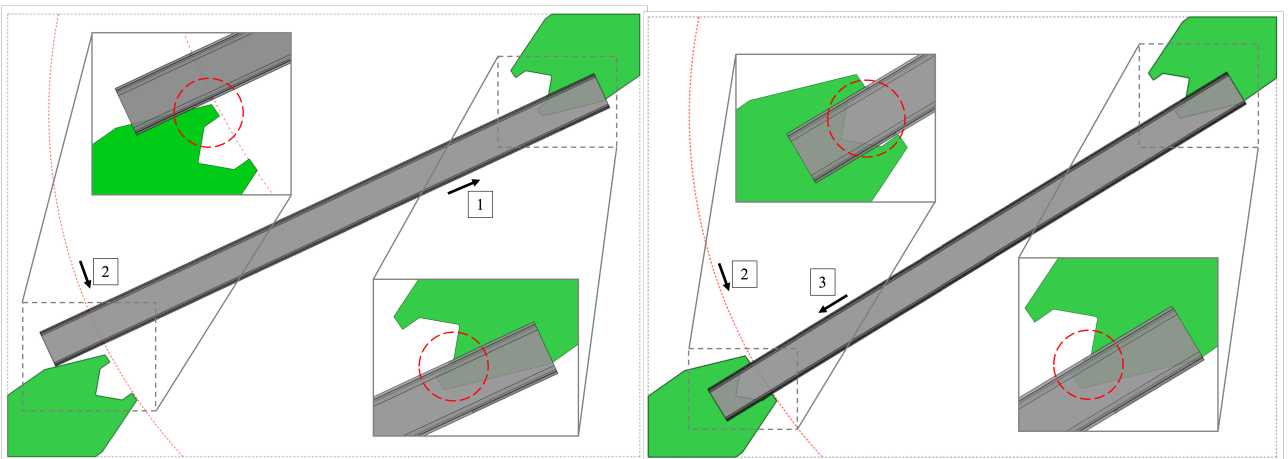
Figure 42: Solution 2 - Modification of the geometry of the gusset plate's notch geometry (3AL1 model with $L_{wg}/L_w = 5\%$)

5.2.3 Solution 3 - Increase of the hidden gap's length

Weld configuration A The previous solution demonstrated that it is possible to add two additional assembly steps compared to the initial SHG connection shown in Figure 41. However, since it is not sufficient, the following solution involves combining a low overlap length ratio, the modified geometry of the gusset plate's notch with a longer hidden gap without changing the weld length. The principle consists of simply increasing the parameter L_{gs} of the gusset plate's notch (Figure 7). The other dimensions of the SHG connection follows the calculations provided by the design methodology described in Section 2.3.2.

The assembly steps for the 3AL1 model, with an overlap length ratio of $L_{wg}/L_w = 5\%$ presented with a combinations of the two previous and actual solution, are illustrated in Figure 43. The initial three steps of the assembly process remain the same as explained previously. In this current solution, there is sufficient space during step 4 for the upper HSS end to rotate and fit between the flaps of the upper gusset plate, as indicated by the red dashed line. The latter step demonstrates the rotation of the HSS tube's upper end, followed by the precise alignment of the brace along the diagonal axis of the frame (step 5). The exact position of the brace is given by the SHG connection's geometry which is derived from the design calculations. The final step 6 involves welding fillet welds on both sides of the brace, connecting the HSS walls and the gusset plate.

Despite the very limited room for maneuver, this solution is promising from a geometric standpoint. The minimal space for rotation indicates that on-site implementation might pose challenges, demanding meticulous precision and careful assembly. Considering the success of the SHG connection involving a weld configuration A, it raises the question of whether a longer weld configuration (weld configuration B) could also be feasible. To provide a comprehensive comparison, Table 12 presents the geometric properties of the two proposed solutions, for a SHG connection involving a weld configuration A (3AL1) and B (3BL1), alongside with the initial values of the models examined in the parametric study.



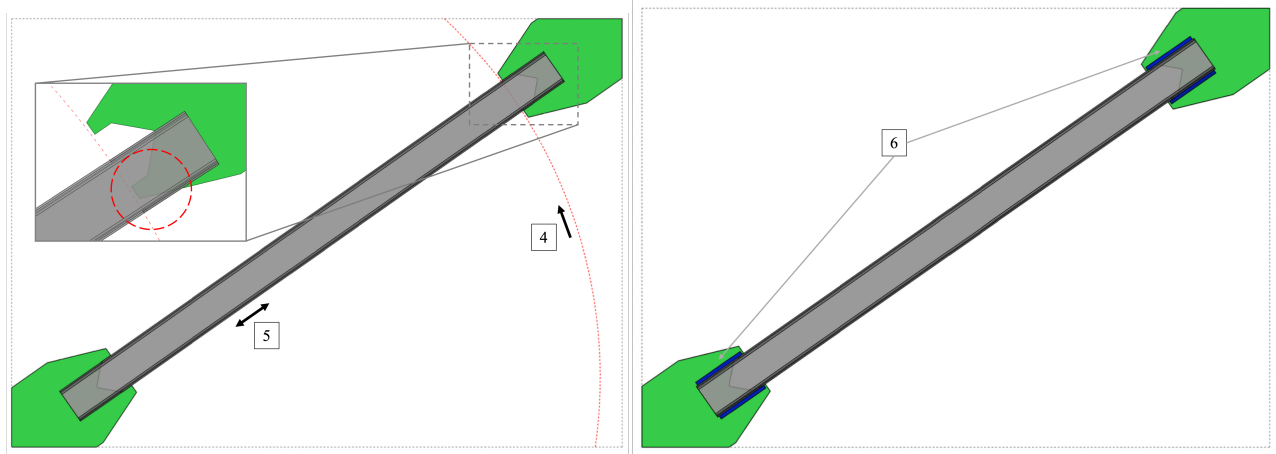
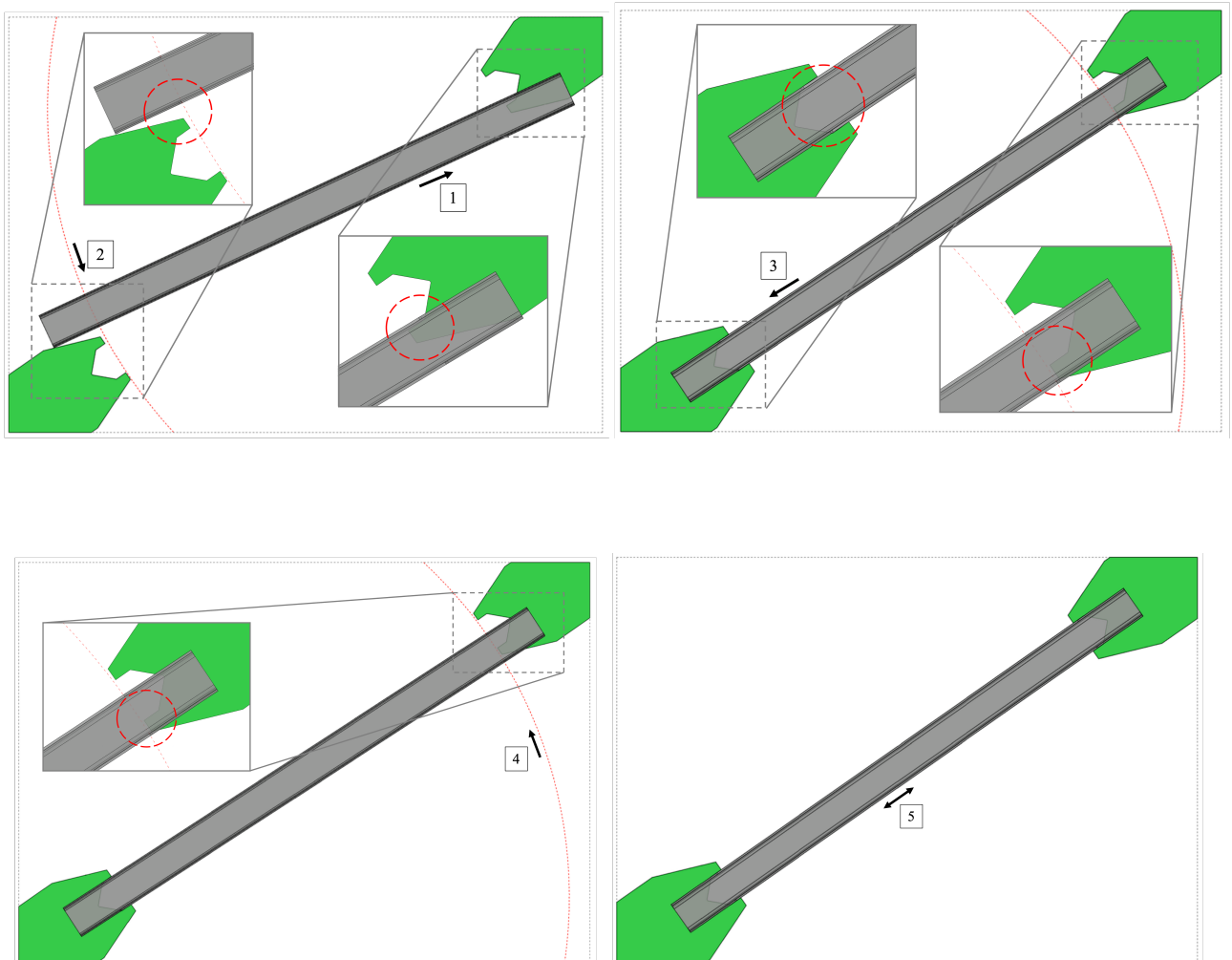


Figure 43: Solution 3 - Increase of the hidden gap's length (3AL1 model with $L_{wg}/L_w = 5\%$)

Weld configuration B Figure 44 illustrates the same steps as the solution featuring weld configuration A. By observing these steps, it can be deduced that a connection incorporating an extended weld configuration (weld configuration B) could also be feasibly implemented on the construction site, with similarly limited margins for maneuvering as for the 3AL1 model (Figure 41).



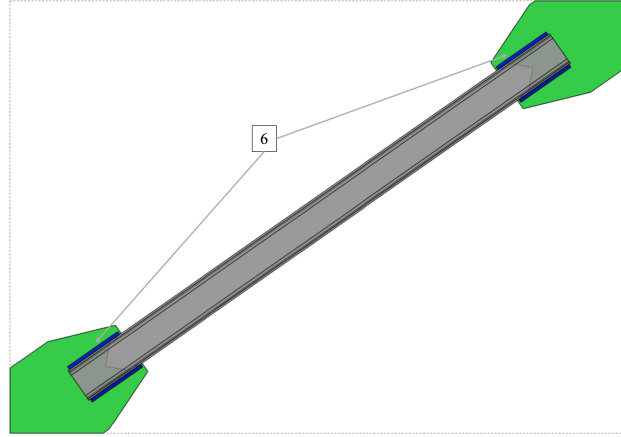


Figure 44: Solution 3 - Increase of the hidden gap's length (3BL1 model with $L_{wg}/L_w = 5\%$)

Table 12: Geometrical properties of the different solutions

Geometrical properties [mm]	3AL1	Solution 3 Weld conf. A	3BL1	Solution 3 Weld conf. B
L_{gs}	67	97	64	111
L_{gap}	30	60	30	70
d_{flap}	44	70	49	84
L_{wn}	389	433	452	504
L_{wg}/L_w	15 %	5 %	15 %	5 %

Note on the geometry of the gusset plate's notch The proposed solution, which involves modifying the geometry of the gusset plate's notch, theoretically has no influence on the calculations of the design methodology proposed by Afifi et al. (2023). The gusset plate is verified based on four criteria, including criteria for the block shear, considering the three showcased modes in Appendix 7.1, as well as buckling. The critical net and shear sections respectively are verified at the widest part of the gusset, denoted as W_g , and along the welds. Therefore, a triangular notch allows these verifications to remain unaffected. Additionally, the gusset plate buckling is evaluated based on the strips depicted in Figure 9, which depend solely on the length L_g , representing the depth of the brace penetration into the gusset plate, and the degree of confinement of the hinge zone.

Future research should focus on determining the optimal shape of the gusset plate's notch and the D_{gs} value in order to construct the SHG connection on site. While a triangular shape, as illustrated in Figure 45b, would enable a deeper brace penetration towards the beam-to-column joint during erection, it may introduce stress concentrations and initiate crack formations at the top corner of the triangle. Consequently, exploring a truncated triangular notch shape, as depicted in Figure 45c, could potentially improve the structural performance.

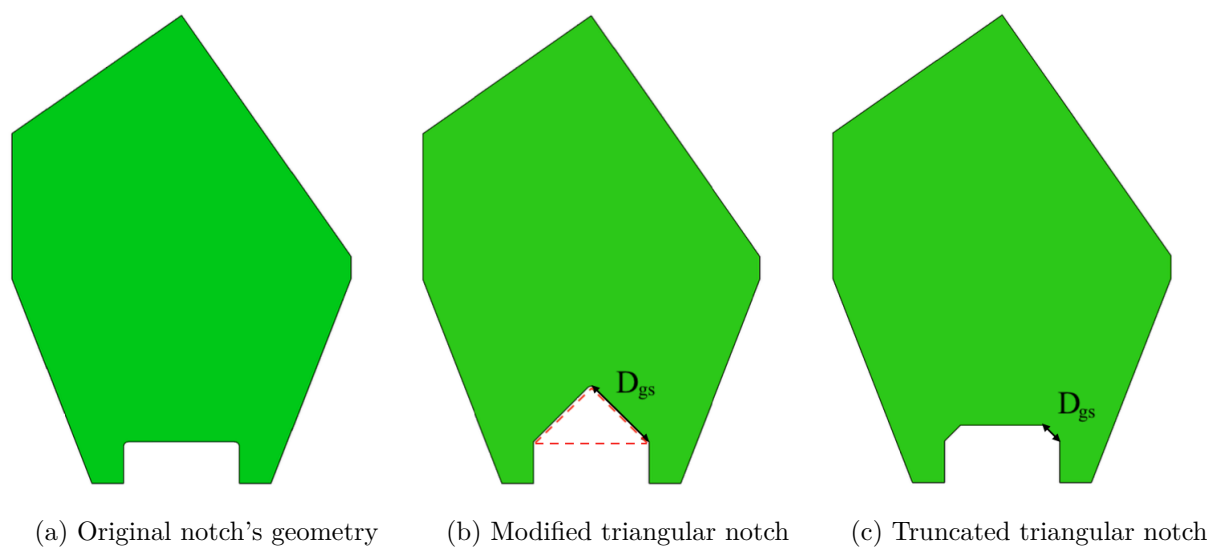


Figure 45: Alternatives for the geometry of the gusset plate’s notch

5.3 Alternative connections to build on-site

This section presents alternative connection methods for linking SHG connections to framing elements when direct installation of the SHG is not possible. Considering the limitations or constraints that may arise during the construction process, it is important to explore and evaluate alternative methods to achieve the desired connection.

A bolted connection is widely considered as the most preferred and simplest option due to its inherent assembly tolerance, as well as its ease of implementation and cost-effectiveness on-site. However, quality assurance plays a crucial role in bolted connections, as it is necessary to carefully control the axial load or preload of bolts to ensure the safety and reliability of structures. In the context of the gusset plate already being welded to the brace in the factory and the member and its SHG connection being transported as is to the construction site, several solutions are presented. The following alternative solutions are depicted through conceptual drawings, where the gusset plates of the connections feature a linear clearance to form the hinge zone.

Figure 46a and 46b present a connection with bolted angles on each side of the gusset to the flanges of the column and/or beam. Bolting to flanges of the column and the beam provides greater execution tolerance and allows for easy replacement of components if necessary. However, depending on the type of the floor covering, bolted angles may hinder its installation, and welding can be used as an alternative. In the case of double bolting (bolting on the flanges of the column and the beam), the hinge zone offset of the gusset plate should be taken into account if it is considered in the design, and efforts should be made to find the optimal arrangement of the angles to accomodate rotation of the gusset plate.

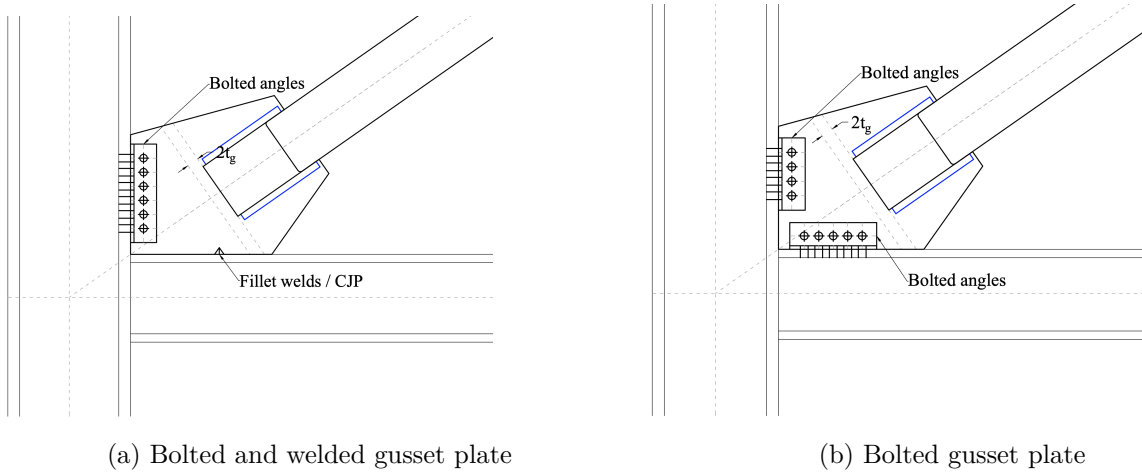


Figure 46: Bolted/welded gusset plate associated to the SHG connection

Another interesting solution would involve rotating the brace by 90° and connecting the gusset to the paddle plate using either welds or bolted angles. This approach offers advantages in terms of brace's buckling since, it allows the brace to flex within the frame's plane. In the two alternative scenarios depicted in Figures 47a and 47b, the only limitation is that the width of the gusset plate should not be excessively wide to ensure proper alignment of the connection within the wall plane. Special attention should be paid to the design of the plates, particularly regarding buckling and eccentricities.

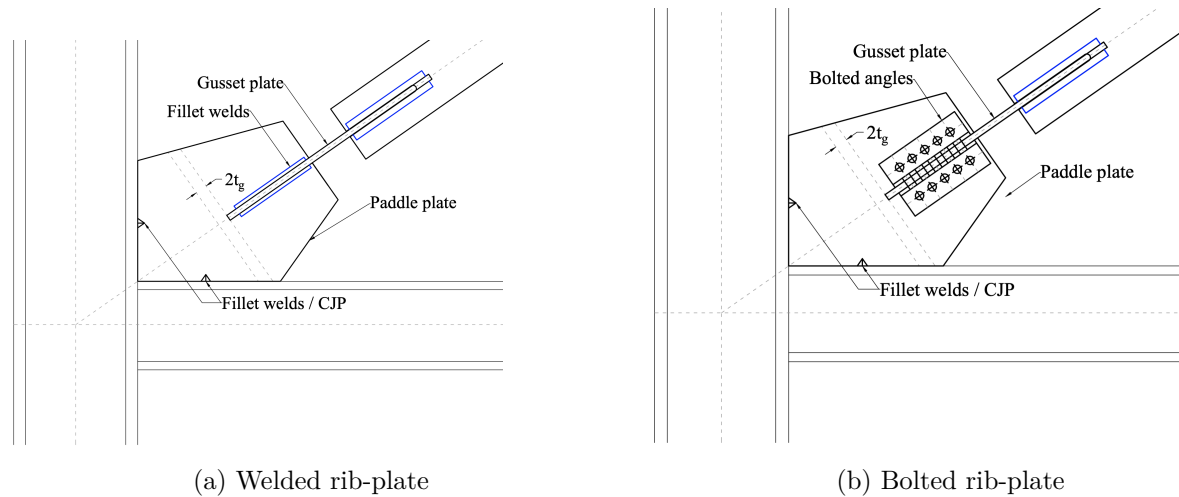


Figure 47: Bolted/welded rib-plate associated to the SHG connection

The final suggested solution as showcased in Figure 48 involves trimming a portion of the upper flange of the beam and directly connecting the gusset plate to the web of the horizontal member using bolts. The vertical edge of the gusset plate can be either welded or bolted, depending on the configuration of the connection between the beam and the column. This solution appears to be practical as it only involves creating holes in the gusset plate and adding additional bolts, without the need for any additional materials such as angles or plates

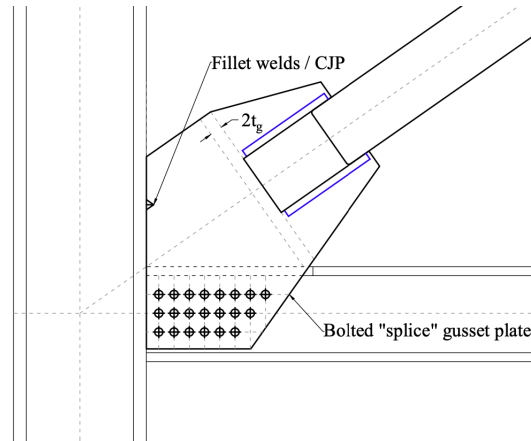


Figure 48: Bolted splice gusset plate associated to the SHG connection

5.4 Summary

In summary, the SHG connection can be assembled on the construction site by considering a combination of an enlarged notch in the gusset plate, a reduced overlap length ratio and an increased hidden gap between the HSS and the gusset plate. It works for a long-weld short-size (weld configuration B) and short-length large-size (weld configuration A) welds. However, the execution tolerances are tight, and for its construction, it will require precision and careful implementation. It is suggested for future research to find the optimal geometry and overlap length ratio to meet the construction tolerances, as well as to numerically study these models to understand their behavior under seismic loading. It is also important to investigate if the enlarged notch significantly influences the compressive response of the gusset plate. If it is concluded that this method cannot be successful, other solutions combining bolted and welded connections are proposed.

6 Conclusion and recommendations

In this report, the inelastic response of HSS SHG brace connections under a reversed cyclic loading protocol through numerical simulations using Abaqus/CAE finite element software is investigated. To establish a numerical base model, a calibration study is conducted by comparing the results of a laboratory-tested full-brace with a finite element model (FEM). Subsequently, a parametric study is performed, involving twenty-one models based on the design methodology proposed by Affi et al. (2023), where parameters such as HSS tube's sizes, brace's slendernesses, weld configurations, and gusset plate clearance rules were varied.

The findings of the parametric study revealed that stockier braces exhibited lower ductility ranges but a higher buckling load compared to slender braces. Among different degrees of confinement of the hinge zone in the gusset plates for the same HSS tube's size, the load-displacement hysteretic response indicated that a constrained configuration with a shorter weld exhibited a higher compressive strength. Moreover, this configuration also resulted in higher moments at the HSS tube's ends at the connection. Interestingly, the impact of the weld configurations on larger tubes was found to be minimal. The Von Mises stresses distribution analysis demonstrated that an elliptical hinge zone with a longer weld induced reduced stresses along the brace.

Through the analysis, critical connection locations with concentrated plastic deformations were identified near the HSS's slot at the front of the welds and at the HSS corners. Importantly, failure was observed to occur at the mid-length of the brace before fracture at the SHG connection, aligning with capacity design principles. The linear and elliptical hinge zone configurations exhibited lower plastic strains at critical locations and are recommended for practical applications. However, it is worth noting that constrained gusset plate configurations are also viable, indicating that fracture at the SHG connection is unlikely to happen prior to fracture at the mid-length of the brace, making it capacity design protected, although it may result in higher levels of plastic strains.

The conceptual study on the on-site implementation of the HSS SHG connection has shown that it can be constructed outside the fabrication plants by combining solutions that include a longer hidden gap between the gusset plate and the HSS, a minimal overlap length ratio, along with a modified geometry of the gusset plate's notch. However, it is important to note that the execution tolerance margins for the presented construction technique are quite narrow, prompting the exploration of alternative construction methods. One possibility is to complement the SHG connection with an additional bolted or welded connection, which can provide greater flexibility and ease of implementation while maintaining structural integrity.

In the future, there is ample room for improvement and further development of the SHG connection. Based on the findings of this study, several recommendations are suggested to enhance the understanding and performance of the SHG connection. These recommendations include :

- The overlap length ratio L_{wg}/L_w plays a crucial role in determining the behavior of the SHG connection. Therefore, it is important to consider values other than 15% to fully explore the potential variations and their impact on the SHG connection's performance under cyclic loading.
- In order to accurately capture the material's inelastic response, it is recommended to conduct

material testing on ASTM A572 using a reversed cyclic loading protocol. This approach will provide more realistic and reliable data compared to relying solely on test results obtained from a monotonic loading protocol.

- It is essential to enhance the accuracy of the material model used for the weld metal and incorporate a more precise representation of the residual stress induced at the connection due to welding by conducting detailed investigations and gathering more comprehensive data to calibrate the weld metal material model.
- Rather than solely relying on the conventional "death-feature" approach, conducting material testing is recommended to develop a more robust fracture model specifically for HSS tubes that can accurately predicts the location of fracture within the tube and at which load it occurs.
- In order to comprehensively capture the behavior of the structure, it is essential to account for the three-dimensional effects by considering the framing elements. While the focus may often be on individual components such as HSS tubes and their connections, neglecting the influence of framing elements can lead to an incomplete understanding of the overall structural response.
- A comprehensive feasibility study should be carried out to precisely determine the optimal geometry of the gusset plate's notch for a successful on-site implementation of the HSS SHG connection. Additionally, conducting numerical studies will provide valuable insights into the behavior of the connection, specifically assessing whether the modified notch significantly influences its response. This rigorous analysis will ensure that the proposed modifications meet the necessary structural requirements without compromising the overall performance and safety of the connection.

References

- Adams, J., & Atkinson, G. (2003). Development of seismic hazard maps for the proposed 2005 edition of the national building code of canada. *Canadian Journal of Civil Engineering*, 30(2), 255–271.
- Afi, M. (2021). *Design and detailing methodology of the "slotted-hidden-gap" connection for square hss brace members* (Doctoral dissertation). McGill University.
- Afi, M., Moreau, R., Tremblay, R., & Rogers, C. A. (2021). Evaluation of the slotted-hidden-gap (shg) connection for square hss brace members. *Journal of Constructional Steel Research*, 179, 106548.
- Afi, M., Tremblay, R., & Rogers, C. A. (2022). Numerical & experimental investigation of slotted-hidden-gap connection for square hss brace members. *Journal of Constructional Steel Research*, 192, 107234.
- Afi, M., Tremblay, R., & Rogers, C. A. (2023). Design and detailing recommendations of slotted-hidden-gap connection for square hss brace members. *Journal of Structural Engineering*, 149(2), 04022249.
- AIJ. (2002). Recommendations for the design and fabrication of tubular truss structures in steel.
- AISC. (2010). *ANSI/AISC 360-10 Specification for Structural Steel Buildings* (American National Standard). American Institute of Steel Construction.
- Astaneh-Asl, A., Goel, S. C., & Hanson, R. D. (1985). Cyclic out-of-plane buckling of double-angle bracing. *Journal of structural Engineering*, 111(5), 1135–1153.
- ASTM. (2003). *Standard Specification for Cold-Formed Welded and Seamless Carbon Steel Structural Tubing in Round and Shapes. A500* (Standard specification). American Society for Testing and Materials.
- ASTM. (2011). *Standard Specification for High-Strength Low-Allow Columbium-Vanadium Structural Steel. A572/A572M* (Standard specification). American Society for Testing and Materials.
- ASTM. (2022). *Standard Specification for Cold-Formed Welded Carbon Steel Hollow Structural Sections (HSS). A1085/A1085M* (Standard specification). American Society for Testing and Materials.
- Atlas tube. (2023).
- AutoDesk. (2023). Autocad 2023.
- CEN. (2004). *Eurocode 8 : Design of structures for earthquakes resistance - Part 1 : General rules, seismic actions and rules for buildings* (Construction standards). European Committee for Standardization.
- Chaboche, J., Van, K. D., & Cordier, G. (1979). Modelization of the strain memory effect on the cyclic hardening of 316 stainless steel.
- CISC. (2010). Handbook of steel construction, 10th edition.
- CSA. (2009). *General requirements for rolled or welded structural quality steel/structural quality steel G40.20/G40.21* (General requirements). Canadian Standards Association.
- CSA. (2019). *S16-19 Design of Steel Structures* (Standard). Canadian Standards Association.
- Fadden, M., & McCormick, J. (2014). Finite element model of the cyclic bending behavior of hollow structural sections. *Journal of Constructional Steel Research*, 94, 64–75.

- Fell, B. V., Kanvinde, A., Deierlein, G., Myers, A., & Fu, X. (2006). Buckling and fracture of concentric braces under inelastic cyclic loading. *Structural Steel Education Council, Steel Tips*, 94.
- Fell, B. V., Kanvinde, A. M., Deierlein, G. G., & Myers, A. T. (2009). Experimental investigation of inelastic cyclic buckling and fracture of steel braces. *Journal of structural engineering*, 135(1), 19–32.
- Haddad, M., Brown, T., & Shrive, N. (2011). Experimental cyclic loading of concentric hss braces. *Canadian Journal of Civil Engineering*, 38(1), 110–123.
- Hartloper, A. R., de Castro e Sousa, A., & Lignos, D. G. (2021). Constitutive modeling of structural steels: Nonlinear isotropic/kinematic hardening material model and its calibration. *Journal of Structural Engineering*, 147(4), 04021031.
- J.A Packer, J. H. (1997). *Hollow structural section - connections and trusses*. Canadian Institute of Steel Construction.
- Koval, I. (2018). *Accounting for cold working and residual stress effects on the axial strength of hss bracing members* (Doctoral dissertation). Ecole Polytechnique de Montréal.
- Lee, K., & Bruneau, M. (2005). Energy dissipation of compression members in concentrically braced frames: Review of experimental data. *Journal of structural engineering*, 131(4), 552–559.
- Lehman, D. E., Roeder, C. w., Herman, D., Johnson, S., & Kotulka, B. (2008). Improved seismic performance of gusset plate connections. *Journal of Structural Engineering*, 134(6), 890–901.
- Logan, D. L. (2007). *A first course in the finite element method, 4th edition* (4th ed.). Chris Carson.
- Martinez-Saucedo, G. (2007). *Slotted end connections to hollow sections* (Doctoral dissertation). University of Toronto.
- Martinez-Saucedo, G., Packer, J. A., & Christopoulos, C. (2008). Gusset plate connections to circular hollow section braces under inelastic cyclic loading. *Journal of structural engineering*, 134(7), 1252–1258.
- Mitsui, Kurobane, & Endoh. (1985). Experimental study on ultimate strength and deformation capacity of welded tube-to-through gusset plate joint. *Journal of Structural Engineering JSCE*, 31B, 145–156.
- Moreau, R. (2014). *Evaluation of the modified-hidden-gap connection for square hss brace members* (Doctoral dissertation). McGill University.
- NRCC. (2022). *Quebec construction code, chapter 1 – building, and national building code of canada 2015 (amended)* (4th ed.). National Research Council of Canada.
- Packer, J., Chiew, S., Tremblay, R., & Martinez-Saucedo, G. (2010). Effect of material properties on hollow section performance. *Proceedings of the Institution of Civil Engineers-Structures and Buildings*, 163(6), 375–390.
- Popov, E. P., & Black, R. G. (1981). Steel struts under severe cyclic loadings. *Journal of the Structural Division*, 107(9), 1857–1884.
- Roeder, C., Lehman, D., Christopolus, A., Gunnarson, I., Johnson, S., & Yoo, J. (2005). Seismic design of braced frame gusset plate connections. *WIT Transactions on The Built Environment*, 81.
- Sen, A. D., Sloat, D., Ballard, R., Johnson, M. M., Roeder, C. W., Lehman, D. E., & Berman, J. W. (2016). Experimental evaluation of the seismic vulnerability of braces and connections in older concentrically braced frames. *Journal of Structural Engineering*, 142(9), 04016052.

- Shaback, B., & Brown, T. (2003). Behaviour of square hollow structural steel braces with end connections under reversed cyclic axial loading. *Canadian Journal of Civil Engineering*, 30(4), 745–753.
- Shaback, J. B. (2001). *Behaviour of square hss braces with end connections under reversed cyclic axial loading* (Doctoral dissertation). University of Calgary.
- SIA. (2020). *SIA 261:2020 Actions sur les structures porteuses* (Normes de construction). Société des Ingénieurs et Architectes.
- Simulia. (2012). Abaqus/cae 6.12, getting started with abaqus.
- Simulia. (2022). Abaqus/cae 2022.
- Skalomenos, K. A., Nakashima, M., & Kurata, M. (2018). Seismic capacity quantification of gusset-plate connections to fracture for ductility-based design. *Journal of Structural Engineering*, 144(10), 04018195.
- Sun, M., & Packer, J. A. (2014). Direct-formed and continuous-formed rectangular hollow sections—comparison of static properties. *Journal of Constructional Steel Research*, 92, 67–78.
- Suzuki, Y., & Lignos, D. G. (2020). Fiber-based hysteretic model for simulating strength and stiffness deterioration of steel hollow structural section columns under cyclic loading. *Earthquake Engineering & Structural Dynamics*, 49(15), 1702–1720.
- Tremblay, R., Archambault, M.-H., & Filiatrault, A. (2003). Seismic response of concentrically braced steel frames made with rectangular hollow bracing members. *Journal of Structural Engineering*, 129(12), 1626–1636.
- Tremblay, R., Haddad, M., Martinez, G., Richard, J., & Moffatt, K. (2008). Inelastic cyclic testing of large size steel bracing members. *The 14th WCEE, Beijing, China*.
- Tremblay, R. (2002). Inelastic seismic response of steel bracing members. *Journal of Constructional Steel Research*, 58(5-8), 665–701.
- Voce, E. (1948). The relationship between stress and strain for homogeneous deformation. *Journal of the Institute of Metals*, 74, 537–562.
- Wakabayashi, M., Nakamura, T., & Yoshida, N. (1977). Experimental studies on the elastic-plastic behavior of braced frames under repeated horizontal loading. part 1 experiments of braces with an h-shaped cross section in a frame. *Bulletin of the disaster prevention research institute*, 27(3), 121–154.
- Yaghoubshahi, M., & Imanpour, A. (2021). An overview of hss brace fracture in steel concentrically braced frames. *Journal of Constructional Steel Research*, 185, 106845.
- Yamamoto, K., Akiyama, N., & Okumura, T. (1988). Buckling strengths of gusseted truss joints. *Journal of Structural Engineering*, 114(3), 575–590.
- Zhao, R., Huang, R., Khoo, H. A., & Cheng, J. R. (2009). Parametric finite element study on slotted rectangular and square hss tension connections. *Journal of constructional steel research*, 65(3), 611–621.

7 Appendix

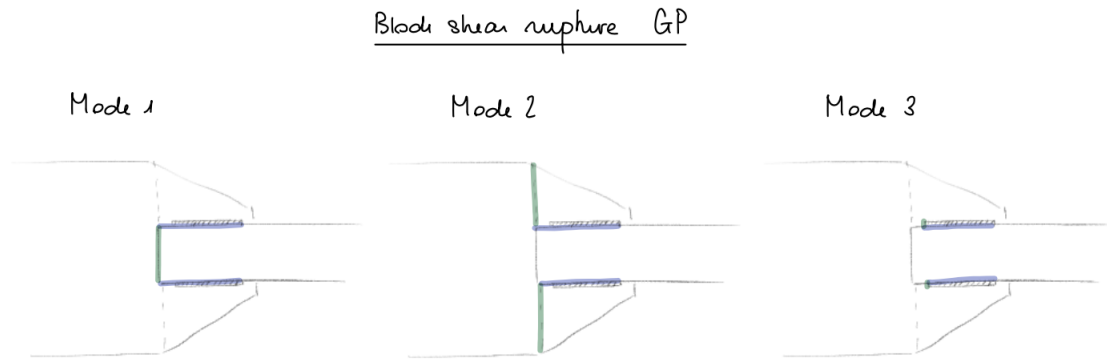
7.1 Design sheets for the parametric study

Parametric study - Weld Configuration A						
Properties		Units	Value			Remarks/References
HSS	Size	inches	HSS 12 5/8	HSS 10 1/2	HSS 5 1/4	
	Width	mm	HSS 305 16	HSS 254 13	HSS 127 6.4	
	Thickness	B	305	254	127	
	Gross area	t	16	13	6.4	
	Radius of gyration	A_g	17700	11800	2960	
Geometry and slenderness	Storey's height (c-c)	r	117	97.9	48.8	
	Storey's width (c-c)	H	3691	3691	3691	
	Brace's angle	W	5271	5271	5271	
	Effective factor	α	35	35	35	
	Brace's length	K	0.9	0.9	0.9	
	Brace's length	L_b	4950	4950	4950	
	Slenderness	L_H	5016	5000	4976	
	Verification	KL_H/r	38.1	45.5	91.3	
	Slenderness	$KL_H/r < 100$	OK	OK	OK	
	Verification	$KL_H/r < 100$	OK	OK	OK	
	Effective width	b_{el}	241	202	101.4	
	Width-to-thickness	b_{el}/t	15.1	15.5	15.8	
HSS material properties	Grade	$b_{el}/t < 17.8$	OK	OK	OK	CSA S16-19 § 27.5.3.2
	Min. yield strength	-	ASTM 1085	ASTM 1086	ASTM 1087	
	Min. tensile strength	F_y	345	345	345	
	Probable yield strength	F_u	448	448	448	
	Probable tensile strength	$R_y F_y$	460	460	460	
	Probable tensile strength	$R_t F_u$	540	540	540	
	Euler buckling stress	T_u	8142	5428	1361.6	
	Dimensionless slenderness	F_e	1325.9	934.3	234.4	
	Factor accounting for manufacturing	λ	0.59	0.70	1.40	
	Probable compressive strength	n	1.34	1.34	1.34	
	Prob. post-buckling resistance	C_U	8142	5103	646	
	Net section fracture	C_U'	1628	1086	272	
GP material properties	Poisson's ratio	T_r	5947.2	3964.8	994.56	CSA S16-19 § 27.1.7 CSA S16-19 § 27.5.4.2
	Elastic modulus	ν	0.3	0.3	0.3	
	Grade	E	200000	200000	200000	
	Min. yield strength	-	ASTM A572	ASTM A572	ASTM A572	
	Min. tensile strength	F_y	Gr. 50	Gr. 50	Gr. 50	
	Probable yield strength	F_u	345	345	345	
	Probable tensile strength	$R_y F_y$	450	450	450	
	Poisson's ratio	T_u	379.5	379.5	379.5	
Resistance factors	Elastic modulus	ν	0.3	0.3	0.3	CSA S16-19 § 27.1.7 CSA S16-19 § 27.5.4.2
	Gross area	E	200000	200000	200000	
		A_g	26862	17625	4654	
Weld geometry	Min. weld length	ϕ	0.9	0.9	0.9	Choice
	Design weld length	ϕ_w	0.67	0.67	0.67	
	Weld size - HSS	ϕ_n	0.75	0.75	0.75	
	Weld size - GP	$L_{w,min}$	437	358	183	
	Weld size - Fracture	L_w	440	390	200	
	Min. weld size	$D_{w,HSS}$	24	18	9	
	Design weld size	$D_{w,GP}$	23	18	9	
		$D_{w,fracture}$	30	23	11	
GP geometry	Width	$D_{w,min}$	30	23	11	Choice
	Thickness	D_w	35	30	15	
GP geometry	Width	W_g	814	705	358	Based on the Whitmore section
	Thickness	t_g	33	25	13	

Shear lag properties		X_{bar}	mm	114	95	48	
		X_{bar}'	mm	98	83	41	
		U	-	1	1	1	
		A_{ne}	mm ²	16548	11072	2755.2	
		A_{ne}/A_g	-	0.93	0.94	0.93	
Overlap length and ratio		L_{wg}	mm	66	59	30	Choice
		L_{wg}/L_w	-	0.15	0.15	0.15	
Detailing geometry	Length of GP insertion	L_g	mm	470	420	230	Choice
	Tolerance of start/end of the welds	L_{tol}	mm	15	15	15	
	Length of the slot in the HSS	L_{wn}	mm	389	346	185	
	Slot's length in GP	L_{gs}	mm	111	100	65	Choice
	Slot's width in GP	W_{gs}	mm	308	257	130	
	Tolerance btw GP and HSS slot	L_{tol}	mm	3	3	3	
	Slot's width in HSS	t_{slot}	mm	36	28	16	
	Straight portion of the hidden gap	$L_{gap,s}$	mm	12	12	12	
	Curved portion of the hidden gap	R	mm	18	14	8	
	Length of the gap	L_{gap}	mm	30	26	20	
	Flap's length	d_{gap}	mm	82	70	32	
Block shear rupture in the HSS	Net section	A_{net}	mm ²	16548	11072	2755.2	CSA S16-19 § 13.11
	Shear area	A_{gv}	mm ²	23744	17264	4531.2	
	Factored resistance	T_r	kN	9796.7	6800.5	1734.2	
	Verification	$T_u < T_r$	-	OK	OK	OK	
Block shear rupture in the GP - Mode 1	Net section	A_{net}	mm ²	10065	6350	1651	CSA S16-19 § 13.11
	Shear area	A_{gv}	mm ²	32010	21750	6370	
	Factored resistance	T_r	kN	9122.7	6033.7	1696.6	
	Verification	$T_u < T_r$	-	OK	OK	OK	
Block shear rupture in the GP - Mode 2	Net section	A_{net}	mm ²	16797	11275	3003	CSA S16-19 § 13.11
	Shear area	A_{gv}	mm ²	23694	16000	4290	
	Factored resistance	T_r	kN	9907.3	6667.3	1780.9	
	Verification	$T_u < T_r$	-	OK	OK	OK	
Block shear rupture in the GP - Mode 3	Net section	A_{net}	mm ²	2310	1500	390	CSA S16-19 § 13.11
	Shear area	A_{gv}	mm ²	9796416	5425280	650227.2	
	Factored resistance	T_r	kN	23694	16000	4290	
	Verification	$T_u < T_r$	-	OK	OK	OK	
Buckling of the gusset plate	Buckling length of the gusset	L	mm	682.13	557.47	290.35	Measured on Abaqus
	Effective factor	K	-	0.9	0.9	0.9	
	Inertia at the Whitmore section	$I_{Whitmore}$	mm ⁴	2437726.5	917968.75	65543.83333	
	Buckling resistance	$N_{cr,gusset}$	kN	12767	7198	1895	
	Verification	$T_u < N_{cr,gusset}$	-	OK	OK	OK	

Parametric study - Weld Configuration B						
Properties		Units	Value			Remarks/References
HSS	Size	inches	HSS 12 5/8	HSS 10 1/2	HSS 5 1/4	
		mm	HSS 305 16	HSS 254 13	HSS 127 6.4	
	Width	B	305	254	127	
	Thickness	t	16	13	6.4	
	Gross area	A _g	17700	11800	2960	
Geometry and slenderness	Radius of gyration	r	117	97.9	48.8	
	Storey's height (c-c)	H	3691	3691	3691	
	Storey's width (c-c)	W	5271	5271	5271	
	Brace's angle	α	35	35	35	
	Effective factor	K	0.9	0.9	0.9	
	Brace's length	L _b	4950	4950	4950	
	Brace's length	L _H	5010	4994	4972	
	Slenderness	KL _y /r	38.1	45.5	91.3	
	Verification	KL _y /r < 100	OK	OK	OK	CSA S16-19 § 27.5.3.2
	Slenderness	KL _H /r	38.5	45.9	91.7	
	Verification	KL _H /r < 100	OK	OK	OK	CSA S16-19 § 27.5.3.2
	Effective width	b _{el}	241	202	101.4	
	Width-to-thickness	b _{el} /t	15.1	15.5	15.8	
	Verification	b _{el} /t < 17.8	OK	OK	OK	CSA S16-19 § 27.5.3.2
HSS material properties	Grade	-	ASTM 1085	ASTM 1086	ASTM 1087	
	Min. yield strength	F _y	345	345	345	
	Min. tensile strength	F _u	448	448	448	
	Probable yield stress	R _y F _y	460	460	460	CSA S16-19 § 27.1.7
	Probable tensile stress	R _t F _u	540	540	540	
	Probable tensile strength	T _u	8142	5428	1361.6	CSA S16-19 § 27.5.4.2
	Euler buckling stress	F _e	1329.0	936.5	234.8	
	Dimensionless slenderness	λ	0.59	0.70	1.40	
	Factor accounting for manufacturing	n	1.34	1.34	1.34	
	Probable compressive strength	C _U	8142	5106	647	CSA S16-19 § 27.5.4.2
	Prob. post-buckling resistance	C _{U'}	1628	1086	272	CSA S16-19 § 27.5.4.2
	Net section fracture	T _r	5947.2	3964.8	994.56	
	Poisson's ratio	ν	0.3	0.3	0.3	
	Elastic modulus	E	200000	200000	200000	
GP material properties	Grade	-	ASTM A572 Gr. 50	ASTM A572 Gr. 50	ASTM A572 Gr. 50	
	Min. yield strength	F _y	345	345	345	
	Min. tensile strength	F _u	450	450	450	
	Probable yield strength	R _y F _y	379.5	379.5	379.5	CSA S16-19 § 27.1.7
	Probable tensile strength	T _u	10247	6654	1737	CSA S16-19 § 27.5.4.2
	Poisson's ratio	ν	0.3	0.3	0.3	
	Elastic modulus	E	200000	200000	200000	
	Gross area	A _g	27000	17534	4576	
Resistance factors		ϕ	0.9	0.9	0.9	
		ϕ_w	0.67	0.67	0.67	
		ϕ_u	0.75	0.75	0.75	
Weld geometry	Min. weld length	L _{w min}	437	358	183	
	Design weld length	L _w	515	470	250	Choice
	Weld size - HSS	D _{w,HSS}	20	15	7	
	Weld size - GP	D _{w,GP}	20	15	7	
	Weld size - Fracture	D _{w,fracture}	26	19	9	
	Min. weld size	D _{w min}	26	19	9	
	Design weld size	D _w	30	25	12	Choice
GP geometry	Width	W _g	900	797	416	Based on the Whitmore section
	Thickness	t _g	30	22	11	

Shear lag properties		X_{bar}	mm	114	95	48	
		X_{bar}'	mm	98	83	41	
		U	-	1	1	1	
		A_{ne}	mm ²	16548	11072	2755.2	
		A_{ne}/A_g	-	0.93	0.94	0.93	
Overlap length and ratio		L_{wg}	mm	66	59	30	Choice
		L_{wg}/L_w	-	0.15	0.15	0.15	
Detailing geometry	Length of GP insertion	L_g	mm	470	420	230	Choice
	Tolerance of start/end of the welds	L_{tol}	mm	15	15	15	
	Length of the slot in the HSS	L_{wn}	mm	389	346	185	
	Slot's length in GP	L_{gs}	mm	111	100	65	Choice
	Slot's width in GP	W_{gs}	mm	308	257	130	
	Tolerance btw GP and HSS slot	L_{tol}	mm	3	3	3	
	Slot's width in HSS	t_{slot}	mm	36	28	16	
	Straight portion of the hidden gap	$L_{gap,s}$	mm	12	12	12	
	Curved portion of the hidden gap	R	mm	18	14	8	
	Length of the gap	L_{gap}	mm	30	26	20	
	Flap's length	d_{gap}	mm	82	70	32	
Block shear rupture in the HSS	Net section	A_{net}	mm ²	16548	11072	2755.2	CSA S16-19 § 13.11
	Shear area	A_{gv}	mm ²	23744	17264	4531.2	
	Factored resistance	T_r	kN	9796.7	6800.5	1734.2	
	Verification	$T_u < T_r$	-	OK	OK	OK	
Block shear rupture in the GP - Mode 1	Net section	A_{net}	mm ²	10065	6350	1651	CSA S16-19 § 13.11
	Shear area	A_{gv}	mm ²	32010	21750	6370	
	Factored resistance	T_r	kN	9122.7	6033.7	1696.6	
	Verification	$T_u < T_r$	-	OK	OK	OK	
Block shear rupture in the GP - Mode 2	Net section	A_{net}	mm ²	16797	11275	3003	CSA S16-19 § 13.11
	Shear area	A_{gv}	mm ²	23694	16000	4290	
	Factored resistance	T_r	kN	9907.3	6667.3	1780.9	
	Verification	$T_u < T_r$	-	OK	OK	OK	
Block shear rupture in the GP - Mode 3	Net section	A_{net}	mm ²	2310	1500	390	CSA S16-19 § 13.11
	Shear area	A_{gv}	mm ²	9796416	5425280	650227.2	
	Factored resistance	T_r	kN	23694	16000	4290	
	Verification	$T_u < T_r$	-	OK	OK	OK	
Buckling of the gusset plate	Buckling length of the gusset	L	mm	682.13	557.47	290.35	Measured on Abaqus
	Effective factor	K	-	0.9	0.9	0.9	
	Inertia at the Whitmore section	$I_{Whitmore}$	mm ⁴	2437726.5	917968.75	65543.83333	
	Buckling resistance	$N_{cr,gusset}$	kN	12767	7198	1895	
	Verification	$T_u < N_{cr,gusset}$	-	OK	OK	OK	

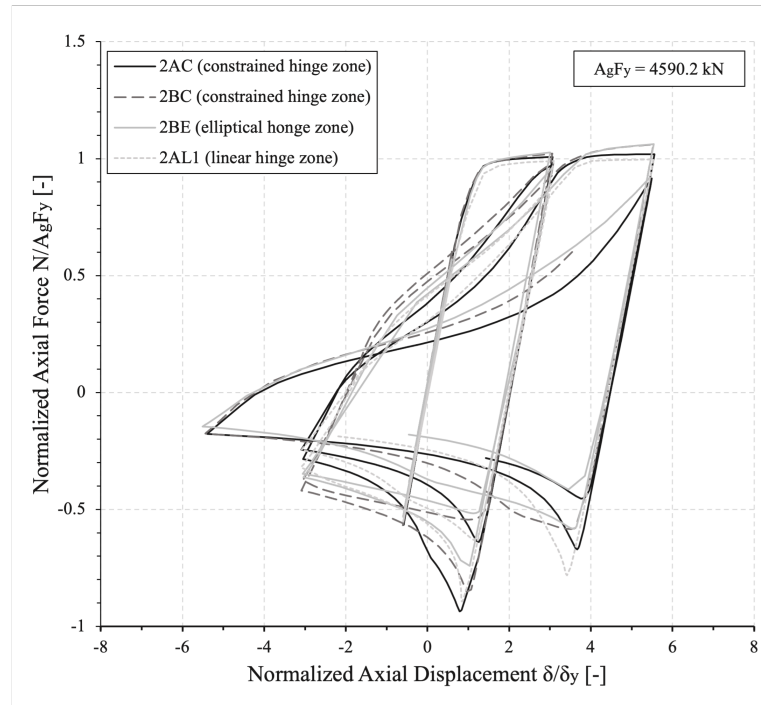


7.2 Chemical composition of the steel grades

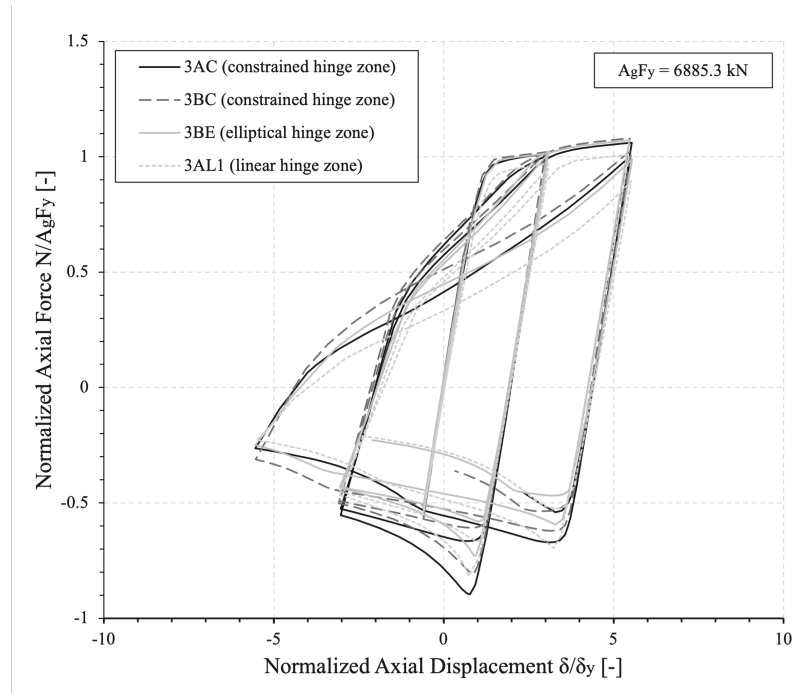
Table 13: Chemical composition of several specifications based on the heat analysis

Chemical composition	ASTM A500 Gr. B	ASTM A1085	CSA G40.20-21 350 W Class C	ASTM A572 Gr. 50
Carbon (max.)	0.26	0.26	0.23	0.23
Manganese (max.)	1.35	1.35	0.5 - 1.50	1.35
Phosphorous (max.)	0.035	0.035	0.040	0.030
Sulfur (max.)	0.035	0.035	0.050	0.030
Silicon (max.)	-	0.04	0.4	0.15 - 0.4
Aluminum (min.)	-	0.015	-	-
Copper (min.)	0.2	-	-	-

7.3 Hysteretic curves with a constrained and elliptical hinge zone



(a) HSS 254 254 13



(b) HSS 305 305 16

Figure 49: Hysteretic response of the braces with a constraint and elliptical clearance zone in the gusset plate

7.4 Von Mises stress distributions

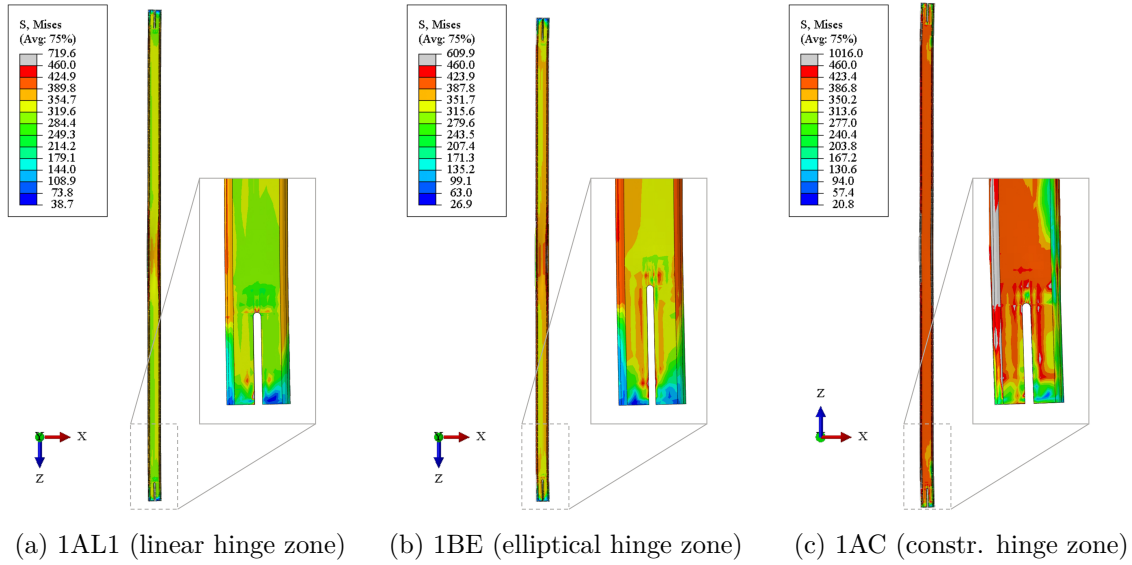


Figure 50: Von Mises stress distributions for 1AL1, 1BE, 1AC models at their respective T_{max}

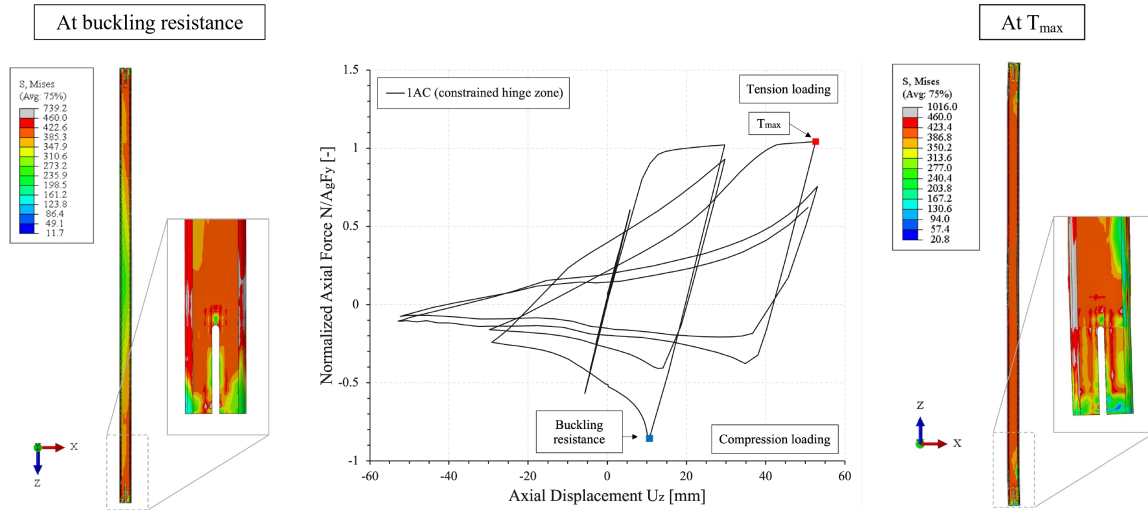


Figure 51: Von Mises stress distributions of the 1AC model (elliptical hinge zone) at the buckling resistance and T_{max}

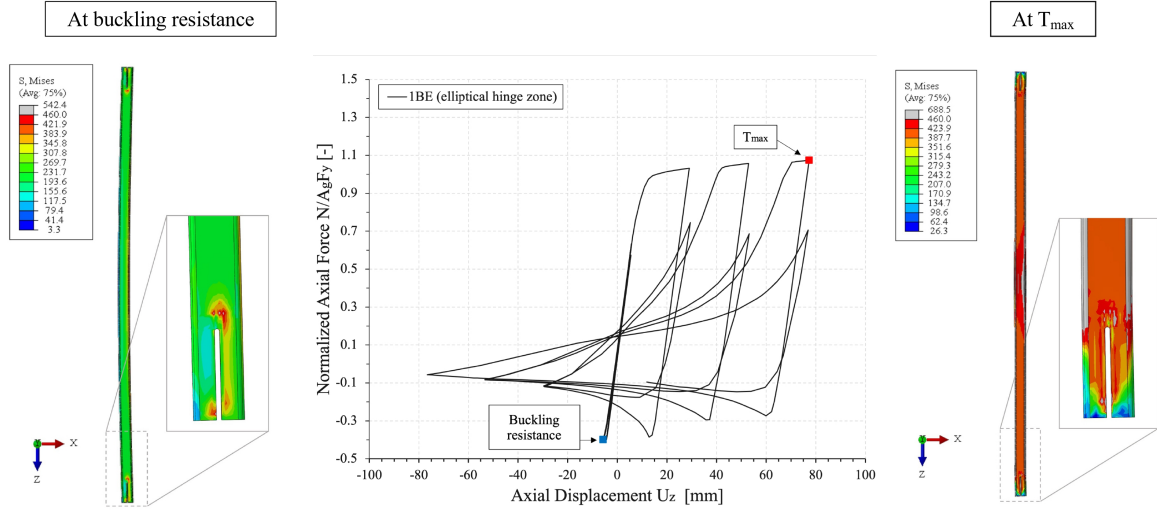


Figure 52: Von Mises stress distributions of the 1BE model (linear hinge zone) at the buckling resistance and T_{max}

Models	At buckling resistance			At T_{max}			At fracture in mid-length of the brace		
	Load [kN]	Drift [%]	Cycle	Load [kN]	Drift [%]	Cycle	Load [kN]	Drift [%]	Cycle
1AC	-986.1	0.93	22	1199.4	1.59	24	589.2	2.26	26
1BE	-459.2	0.31	19	1237	2.33	26	102.1	2.96	27
1AL1	-449.8	0.93	22	1174.2	2.33	26	1192	3.39	28
2AC	-4287.3	0.94	23	4679.6	1.59	24	-1286	2.02	25
2BE	-3402	0.93	23	4876.2	1.59	24	-826	2.04	25
2AL1	-4097	0.94	23	4567.92	1.57	24	-854.4	1.71	24
3AC	-6171.1	0.95	23	7306.2	1.60	24	-3117.9	2.01	25
3BE	-5009.8	0.94	23	7373.5	1.60	24	-1415.1	2.07	25
3AL1	-5622.6	0.95	23	6943.7	1.61	24	-1441.9	2.06	25

Table 14: Loads, Drifts and Cycles at buckling load and T_{max} for xAC, xBE and xAL1 type